AN ABSTRACT OF THE THESIS OF

In-Sik Kang for the degree of Doctor of Philosophy in Atmospheric Sciences presented on March 27, 1984

Title: Quasi-Stationary Atmospheric Responses to Large-Scale Forcing

Abstract approved: Redacted for Privacy

A time-dependent, spectral, barotropic model and a similar two-layer primitive equation model are developed to investigate the planetary-scale wave responses to various types of large-scale forcing: vorticity and heat sources, and sea surface temperature (SST) anomalies. Both models are linearized about the zonal mean states of January climatology.

The characteristics of forced Rossby waves are extensively studied based on both the barotropic model experiments and the theory of Rossby wave propagation on the sphere (Hoskins and Karoly, 1981). In particular, both model and theoretical results show that the responses are dominated by ultra-long wave components (zonal wavenumber m = 1, 2, and 3), and that the large responses occur for vorticity sources located at the subtropics and at the high latitudes near 45°N. The model experiments for the wavenumber-dependent sources located at various latitudes show that the ultra-long waves behave like a north-south seesaw between the high and middle latitudes (m = 1) or between the high latitudes and

subtropics (m = 2). The north-south seesaw of zonal wavenumber 1 component is in good agreement with that observed by Gambo and Kudo (1983). The responses of long waves (m > 3) are, however, localized in the source regions with relatively small amplitudes.

The characteristics of baroclinic responses to prescribed heat sources located at various latitudes are also examined. Over the source latitudes baroclinic responses are dominant; however, the remote responses have a barotropic structure. The north-south seesaws appearing in the barotropic model are also observed in the baroclinic model.

A series of baroclinic model experiments, in which surface heat fluxes and internal heating are computed in terms of the model variables, are also conducted to investigate the linear effect of sea-surface temperature (SST) anomalies on the atmospheric circulation. The experiments for prescribed SST anomalies, taken equal to twice those of Rasmusson and Carpenter (1982), simulate many aspects of the associated observed atmospheric anomalies, and suggest, therefore, that a large part of the atmosphere's responses occur via linear dynamics. It is also suggested that the rather weak responses in the North Pacific are due to the lack of a zonally varying basic state. In the case where the SST anomalies are located in the middle latitudes, the responses are about five times smaller than for the tropical SST anomalies. This result is also fairly consistent with the GCM experimental results by Chervin et al. (1976).

Subsequent experiments, using climatological January SSTs in the tropics, suggest that the tropical Pacific SST can be an important factor in maintaining the climatological standing waves, at least over the western half of the Northern Hemisphere.

Quasi-Stationary Atmospheric Responses to Large-Scale Forcing

by

In-Sik Kang

A THESIS

submitted to

Oregon State University

in partial fulfillment of

the requirements for the

degree of

Doctor of Philosophy

Completed March 27, 1984

Commencement June 1984

APPROVED:

Redacted for Privacy

Associate Professor of Atmospheric Sciences in charge of major

Redacted for Privacy

Chairman of the Department of Atmospheric Sciences

Redacted for Privacy

Dean of Graduate School

Date thesis is presented March 27, 1984

Typed by Naomi W. Zielinski for In-Sik Kang

To my wife Jeung-Hee

ACKNOWLEDGEMENTS

It is with pleasure and deep gratitude that I wish to thank my major professor Dr. Young-June Han for his guidance and support throughout the course of my Ph.D. program. Gratitude is also due to Professor W. Lawrence Gates. His kind advice and encouragement made the present work pleasant. I would also like to thank Professor Michael E. Schlesinger for his careful reading to improve the manuscript; Professor Steven K. Esbensen for fruitful discussions; and Professor Fred L. Ramsey for his interest and valuable comments. I wish to express my sincere thanks to Mr. William McKie for his very productive suggestions on computer programming; and Naomi W. Zielinski for typing the thesis. Finally, I would like to express my gratitude to my wife Jeung-Hee and my parents for their encouragement and support throughout the course of this work. This research was supported by the National Science Foundation under grant ATM 8205992.

TABLE OF CONTENTS

LIST OF FIGURES

Quasi-Stationary Atmospheric Responses to Large-Scale Forcing

1. Introduction

Tropospheric planetary waves at middle and high latitudes are of great interest to meteorologists because of their significant influence on regional climate and its short term fluctuations. Observations reveal that on a long term average these waves are stationary relative to the earth's surface, but their interannual fluctuations often result in profound impacts on certain regional climates (Namias, 1978). For this reason, the study of the dynamics of these planetary waves is an important subject in climate research.

There is little doubt that the irregularities of the earth's land and ocean masses are the major factors that influence the observed planetary waves. The studies by Charney and Eliassen (1949), Kasahara et al. (1973) and more recently Grose and Hoskins (1979) show that the waves are primarily the results of topographical forcing. Smagorinsky (1953) and Sankar-Rao and Saltzman (1969), on the other hand, emphasized the importance of longitudinal differential heating due to land-sea contrast. The latter study in particular showed that the topography alone produces the planetary waves, but with a significant phase displacement which can be corrected only when the differential heating is included. Recently, Simmons (1982) suggested an interesting possibility that the climatological forcing in the tropics can also be

partially responsible for the climatological standing waves in the middle and high latitudes.

Planetary-scale standing waves are found to fluctuate from year to year. For instance, during the winter of 1976-77, the United States experienced numerous outbreaks of cold arctic air with accompanying heavy snows and blizzards in the Northeast and persistent droughts in the West, while Alaska was abnormally warm (Namias, 1978). A similar weather pattern also occured during a previous record-breaking cold winter in 1963. In addition to such phenomenological documentations of the wave fluctuations, many recent studies have found that there exist significant correlations between the fluctuations at widely separated points (e.g., Wallace and Gutzler, 1981; Gumbo and Kudo, 1983). These teleconnection patterns are generally characterized by equivalent barotropic structure and are mostly dominated by the scale of planetary waves. Also the centers of these patterns tend to be located preferentially at several particular latitudes.

Among the geograpically localized patterns found in the above studies, an interesting example is the one that Wallace and Gutzler referred to as the Pacific/North American (PNA) pattern. The abnormal planetary wave fluctuations during the 1976-77 winter were a typical case of the PNA pattern. The precise causes for such planetary wave fluctuations are not known, but seem to be somehow related to tropical forcing. Since the pioneering work of Bjerknes (1969), it has been speculated that tropical SST anomalies are a major factor influencing such fluctuations. Recently, Horel and Wallace (1981) have found that wintertime circulation anomalies in the Pacific/North American sector

are closely related to the equatorial Pacific SST anomalies and resemble the typical normal modes of standing Rossby waves apparently emanating from the tropical Pacific. In linear model studies, such Rossby waves have been assumed to be a consequence of anomalous tropical forcing in association with the tropical SST fluctuation (Hoskins and Karoly, 1981, hereafter HK; Simmons, 1982). However, other mechanisms such as resonance of Rossby waves (Tung and Lindzen, 1979) or local barotropic instability (Simmons et al., 1983) have also been suggested to be possible causes of planetary wave fluctuations.

Recent numerical experiments using general circulation models (GCMs) with prescribed SST anomalies reproduce the observed anomaly patterns of Horel and Wallace (Blackmon et al., 1983; Shukla and Wallace, 1983). However, mainly due to the inherent complexity of the models, the dynamics which presumably led to such anomaly patterns are still difficult to understand. Therefore, it is desirable to use simpler models to understand the dynamics of planetary waves. For this reason we have developed relatively simple linear spectral models to study the effect of SSTs on the atmospheric circulation.

Several simplified linear models have already been developed for similar purposes. HK and Simmons (1982) prescribed heating fields in their models, and interpreted the model results based on the linear Rossby wave dynamics. Webster (1981) let his model generate the internal heating, and showed that cumulus heating is an important wave forcing mechanism. In Webster's model, constant surface heat fluxes were simply prescribed. However, Hendon and Hartmann (1982) pointed out that the surface sensible heat flux is an important factor influencing

the atmospheric response. Therefore, as an extension of the previous models, we have included both mechanisms of surface heat fluxes and cumulus heating in the present baroclinic model.

To help better understand the planetary wave dynamics, a linear barotropic model is also developed, and the dynamics of Rossby wave propagation on the sphere is examined in detail for each wavenumber component. In particular, by prescribing wavenumber-dependent sources at various latitudes, some characteristics of the teleconnection patterns are clearly delineated. These include the particular wavenumbers and the latitudes preferred for the most significant remote responses associated with the north-south seesaws. The characteristics observed in the barotropic model are also examined using the baroclinic model.

Although the major objective of the present study is to better understand the linear dynamics of the tropically forced planetary waves, it is insightful to apply the models to some other closely related problems. Therefore, the baroclinic model is used with a middle latitude SST anomaly to resolve some of controversial scientific issues on the relative importance of such anomalies. The resulting relatively weak amplitudes of both the local and remote responses simulated by the present model are explained from a linear dynamical point of view. Another model application made in this study is intended to examine the role of the longitudinal asymmetry of the climatological tropical Pacific SST on the atmospheric standing waves. The experimental results strongly indicate that certain regional patterns of the middle latitude standing waves can be significantly influenced by the tropical SST distribution.

This dissertation is organized as follows. In Chapter 2 we review the observational and numerical model studies and also present the theoretical backgrounds which are relevant to the present study. The linear barotropic and baroclinic models developed for the present work are described in Chapter 3. The barotropic experimental results, along with a discussion of the relevant dynamics which control the local and remote responses, are presented in Chapter 4. In Chapter 5 the baroclinic responses to prescribed heat sources are examined, while the baroclinic responses to SSTs are discussed in Chapter 6. Finally, a summary of the present work and the concluding remarks are given in Chapter 7.

2. REVIEW OF PREVIOUS RESEARCH

As background for the present study it is useful to summarize the previous observational and numerical studies which are most relevant to this research. Some theoretical background is also given to aid in the interpretation of the results of this work and to understand the dynamics involved.

2.1 Observations

2.1.1 Some observed spatial characteristics of teleconnections

The characteristics and spatial patterns of planetary-scale standing oscillations in the Northern Hemisphere have been documented by many authors (van Loon and Rogers, 1978; Wallace and Gutzler, 1981; Lau, 1981; Gambo and Kudo, 1983). Among these studies the most comprehensive summary is provided by Wallace and Gutzler. They discussed in detail the teleconnection patterns of 500 mb heights, and found two types of distinctive reproducible patterns. One pattern is the north-south seesaw between the high and middle latitudes which occurs in the North Pacific and North Atlantic oceans, and the other pattern is the PNA pattern. These patterns are shown in their teleconnectivity map (Fig. 2.1b). It is interesting to note that the distinctive teleconnectivity patterns in the 500 mb height are generally found for the sea-level pressure (Fig. 2.1a). Wallace and Gutzler also try to identify the teleconnection pattern using EOF analysis. Figures 2.2a-d show the first four eigenvectors of the normalized covariance matrix derived from 500 mb height time series consisting of 45 winter months.

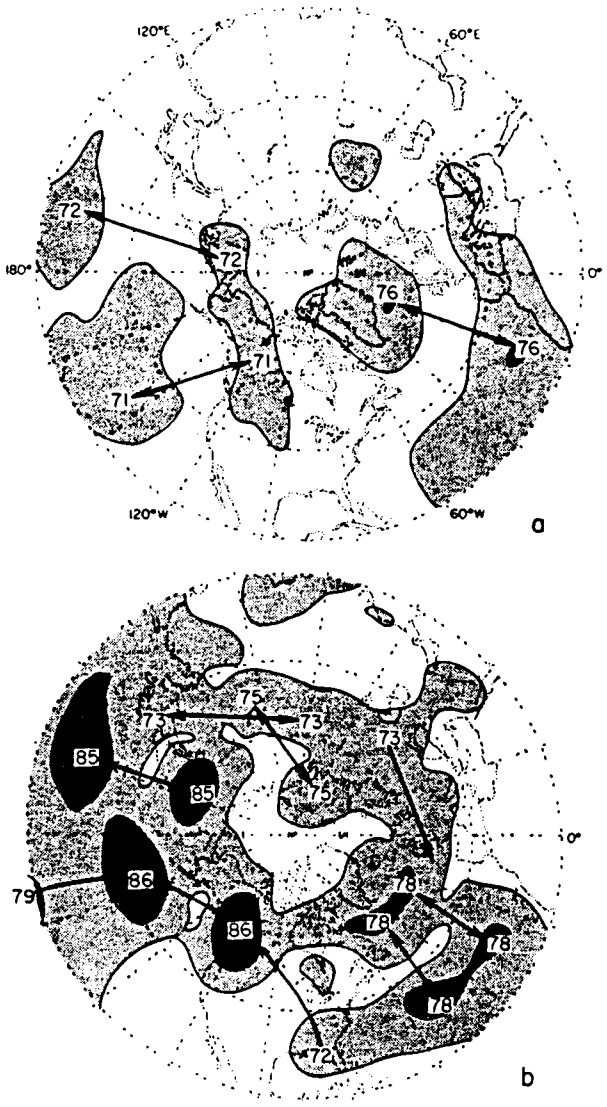

Fig. 2.1. Strongest negative correlation $\rho_{\hat{}}$ on each one-point correlation map, plotted at the base grid point (referred to as "teleconnectivity") for (a) sea-level pressure and (b) 500 mb height. Based on 45 winter months (Decembers, Januarys, and Februarys for winters 1962-63 through 1976-77). Taken from Wallace and Gutzler (1981).

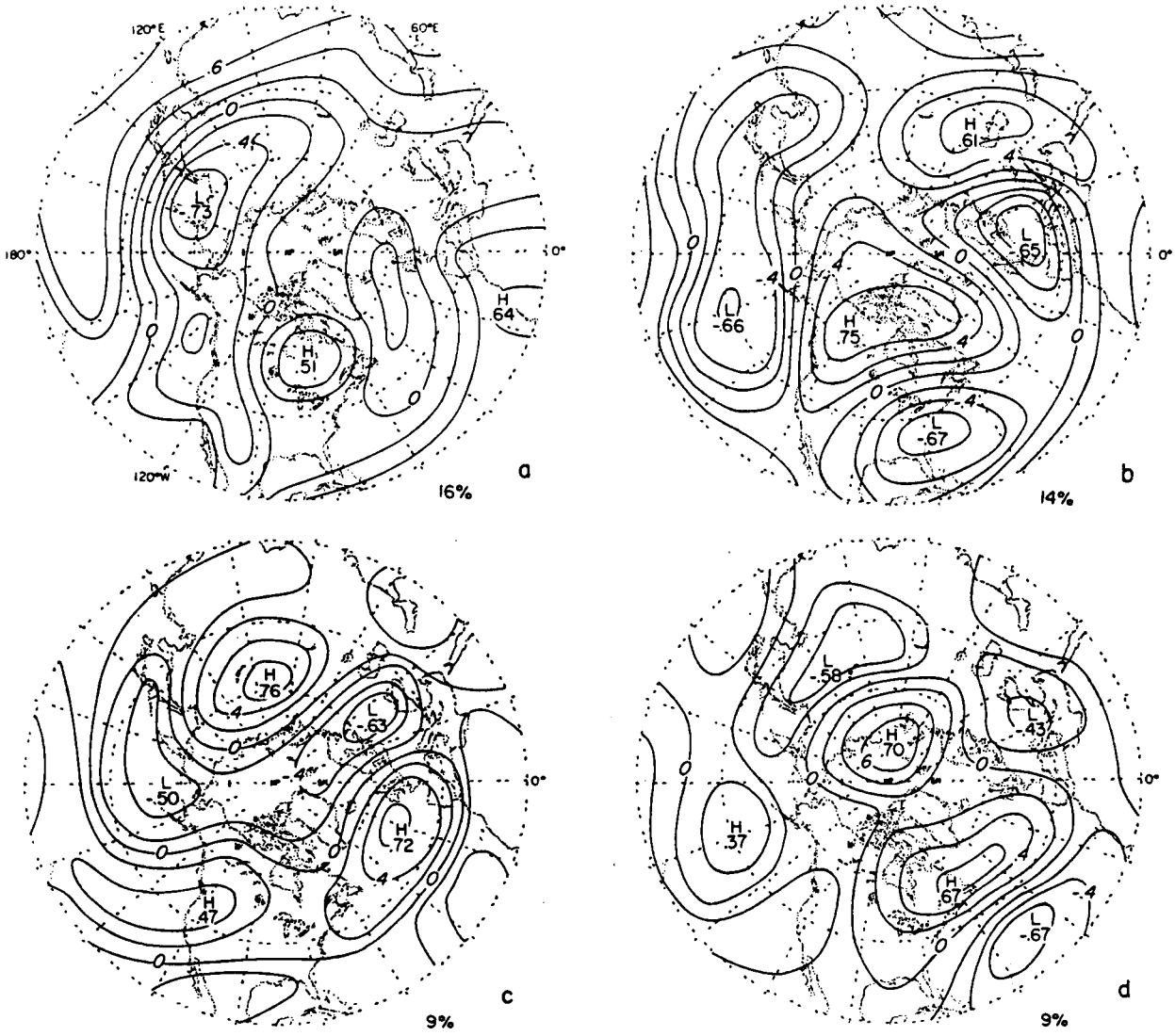

Fig. 2.2. Horizontal structure of the first four modes of an eigenvector analysis expansion of 500 mb height as computed from the normalized covariance matrix R. Based on the 45 month data set. Numbers below each chart indicate the percentage of the hemispherically integrated normalized variance explained by that mode. Taken from Wallace and Gutzler (1981).

In these figures the leading eigenvectors are characterized by distinctive patterns of regional scale with certain dominant zonal wavenumber components. The first principal component shown in Fig. 2.2a appears to be dominated by the north-south seesaw between the high and middle latitudes with zonal wavenumber 2 component. The third principal component (Fig. 2.2c) shows the north-south seesaw between the middle latitudes and the subtropics with dominant zonal wavenumber 3. Figures 2.2b and d show the other two modes which are also dominated by planetary-scale wave components.

van Loon and Rogers (1978) calculated the correlation coefficients of mean sea-level pressure between the point (70°N, 20°W) and all other grid points north of 20°N based on data for 53 winters. The pattern of their correlation coefficients also appears to be characterized by the north-south seesaw between the high and middle latitudes with the scale of planetary waves. Gambo and Kudo (1983) also calculated correlation coefficients but using the zonally asymmetric geopotential heights for 30 winter months, and found that a predominent standing oscillation has a zonal wavenumber 1 component. In their study, because of barotropic nature of the standing wave oscillation, the 500 mb level height fields are used. As shown in Fig. 2.3a, regardless of which longitude they choose for the base grid point along the 75°N latitude in the Asian-Europian sector, maximum amplitudes occur in the polar region and in the middle latitudes near 45°N with a minimum amplitude occurring at about 55°N. The phase difference between the two amplitude maxima is about 180° (Fig. 2.3b). Over the Pacific and Atlantic sectors, the correlation patterns (not shown) are similar to those of Fig. 2.3.

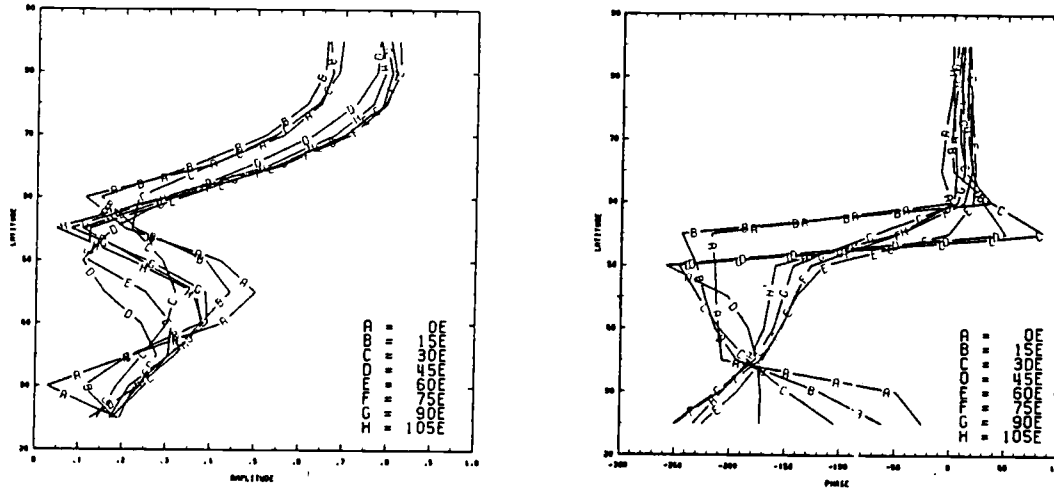

Fig. 2.3. (a) Latitudinal distribution of amplitude of the k-component of $\rho(\lambda, \Phi)$ (k: zonal wavenumber) over Asia-Europe. Here k=1 and latitude of base grid point, ϕ^* is 75°N. Longitude of base grid point, λ^* is denoted by A, B, ..., H. (b) As in (a), but for longitude of relative phase, $\lambda - \lambda^*$ Taken from Gambo and Kudo (1983).

These results thus indicate that the north-south seesaw of zonal wavenumber 1 between the polar and middle latitudes is a distinctive feature of the planetary-scale oscillation.

2.1.2 Observations related to the tropical SST anomalies

Recent observations indicate that the standing oscillation in the tropics (Southern Oscillation) is closely correlated with the inter-annual variability of tropical SST. For example, Rasmusson and Carpenter (1982) documented more recent observational evidence of such correlations in connection with El Niño episodes during which warm SST anomalies are usually found in the eastern and central equatorial Pacific. The earlier study by Krueger and Winston (1974) also revealed that during an anti El Niño episode (Feb. 1971), both the trade and upper tropospheric westerlies over the Pacific Ocean (Walker circulation) were unusually strong. The upper tropospheric westerlies were associated with well developed high-level oceanic troughs over the central Pacific. During the period of an El Niño episode (Feb. 1969), on the other hand, the Walker Circulation was considerably weaker and the high-level mid-oceanic troughs were even replaced by anticyclonic flow. The low-level circulation changes documented in their study were also found in Rasmusson and Carpenter. Recently, Kahlsa (1983) investigated the precipitation changes during the 1972-73 El Niño event, and found that the position and time variation of rainfall were closely related to moisture convergence rather than to the SST. In fact, he showed that the maximum rainfall anomaly was located about 20° west of the maximum SST anomaly.

In conjunction with the changes of tropical ciculation related to the tropical SST anomalies, the teleconnections to extratropical latitudes have also been documented (Bjerknes, 1969; Horel and Wallace, 1981; van Loon and Madden, 1981). A typical global teleconnection pattern at upper tropospheric level associated with El Niño is illustrated schematically in Fig. 2.4 (Horel and Wallace, 1981). During the Northern Hemisphere winter which falls within warm episodes of tropical SST anomalies, the following features have been noted:

a) The Pacific jet stream is stronger and farther to the south than normal.

b) There are negative mid-tropospheric geopotential height anomalies over the North Pacific, which reflect deepening of the Aleutian Low.

c) There are positive mid-tropospheric geopotential height anomalies over western Canada.

d) There is a negative anomaly center over the southeastern United States, which is reflected in both surface temperature and sea-level pressure.

In an attempt to link the change of middle latitude circulations to the tropical SST anomalies, Bjerknes (1969) invoked a chain of nonlinear general circulation processes. In contrast, Horel and Wallace (1981) provided observational evidence of direct propagation of linear Rossby waves from the tropics to the middle latitudes, which was suggested by HK. From a general dynamical point of view, both

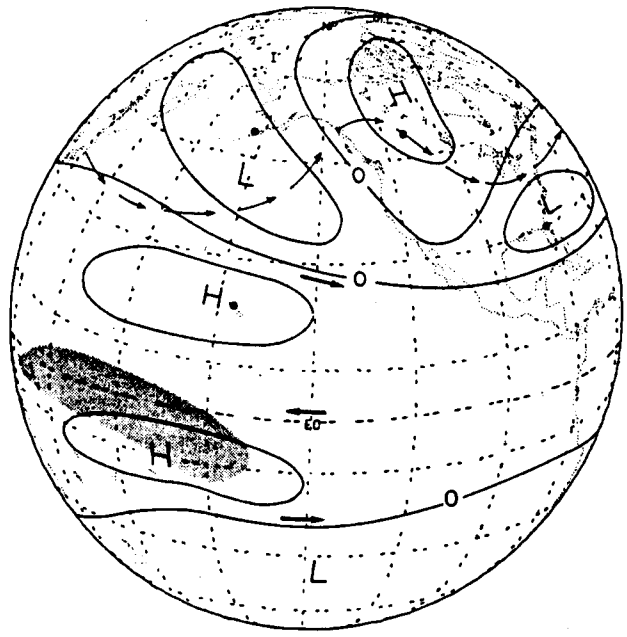

Fig. 2.4. Schematic illustration of the hypothesized global pattern of middle and upper tropospheric geopotential height anomalies (solid lines) during a Northern Hemisphere winter which falls within an episode of warm sea surface temperature in the equatorial Pacific. The arrows in darker type reflect the strengthening of the subtropical jets in both hemispheres along with stronger easterlies near the equator during warm episodes. The arrows in lighter type depict a mid-tropospheric streamlines as distorted by the anomaly pattern, with pronounced "troughing" over the central Pacific and "ridging" over western Canada. Shading indicates regions of enchanced cirriform cloudiness and rainfall. Taken from Horel and Wallace (1981).

possibilities seem to be plausible. But the unique anomaly pattern which resembles the typical normal mode of propagating Rossby waves on the sphere suggests the importance of the linear wave dynamics.

2.2 Numerical studies

2.2.1 GCM experiments with SST anomalies

A logical extention of the observational studies may be numerical experiments in which relevant physical processes are included. In fact, several general circulation model experiments have already been carried out. Rowntree (1972) performed the first tropical SST anomaly experiment and found strong local and remote responses which possessed many of the characteristics noted by Bjerknes (1966). However, Rowntree's experiment had serious limitations because of the presence of an equatorial wall and the rather short integration period. Ramage and Murakami (1973) argued that the equatorial wall in Rowntree's model was responsible for the large responses. Julian and Chervin (1978) also conducted a set of GCM experiments using the NCAR GCM. They found a statistically significant upper-level easterly anomaly over the eastern Pacific and strengthening of subtropical jet stream, but their extratropical response did not appear to be statistically significant. The model that they used, however, was deficient in its ability to simulate the observed wintertime stationary waves (Shukla and Wallace, 1983).

Motivated by more recent observations and theoretical studies, a new series of GCM experiment has been performed using models which simulate the global climatology reasonably well. Blackmon et al.

(1983) have made an experiment using the NCAR Community Climate Model. Their results, as illustrated in Fig. 2.5, show that the simulated tropical anomaly fields of precipitation (Fig. 2.5b), 990 mb wind (Fig. 2.5c), and 200 mb wind (Fig. 2.5d) have high statistical significance, and are in good agreement with observations. In extratropical latitudes, the 500 mb height anomalies (not shown) generally agree with the observed PNA pattern. It should be mentioned that their experiments were carried out with twice the SST anomaly in Fig. 2.5a. Some additional remarks on these results will be given in Chapter 6 in comparison with the results of the present study.

Three separate experiments using the GLAS GCM with observed January initial conditions and a realistic SST anomaly field of Rasmusson and Carpenter (1982) have been made by Shukla and Wallace (1983). These simulations also reproduced many aspects of the observed circulation changes in the tropics as well as in the middle latitudes. The simulated eastward shift of the heavy convective precipitation belt in the western Pacific was particularly notable in all three experiments. It was also found that the simulated 300 mb height anomaly fields resemble the two-dimensional Rossby waves propagating along a great circle path, poleward over the North Pacific and eastward across North America. Although there was considerable variability from experiment to experiment, the results are generally consistent with observations.

In view of their particular relevance to the later discussion of the present study, some of the common features of the GCM sensitivity experiments with tropical SST anomalies are summarized below:

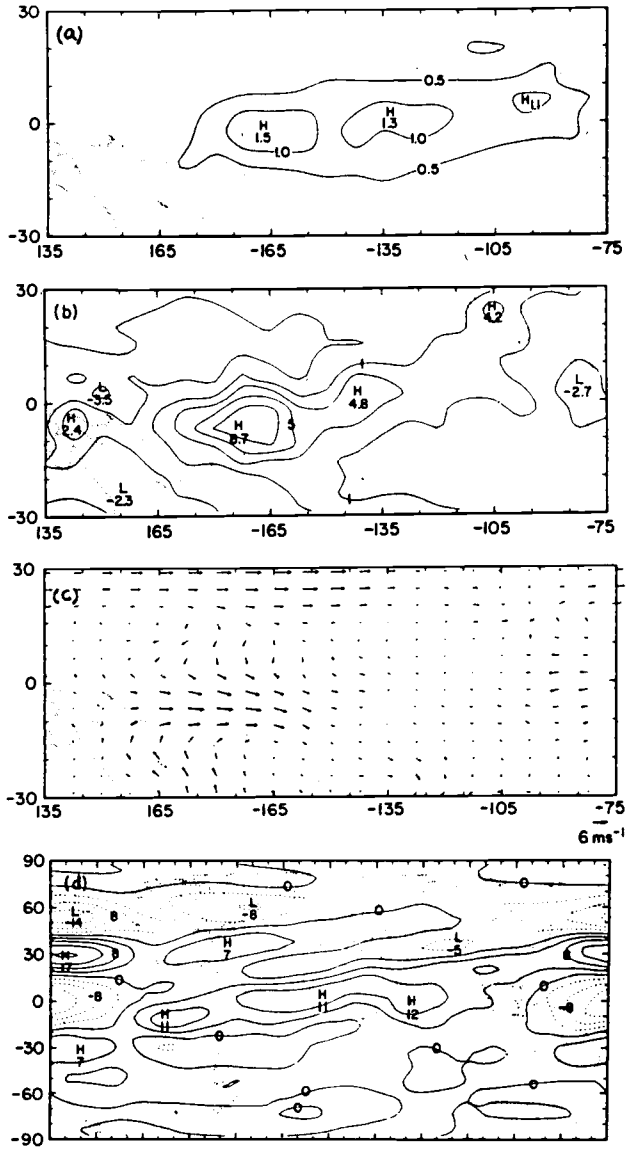

Fig. 2.5. (a) Tropical Pacific SST anomaly referred to as the warm anomaly. (b) The ensemble-average precipitation anomaly (mm/day). Twice as warm minus control case. (c) Vector plot of the 990 mb wind anomaly in the twice as warm minus control case. (d) The 200 mb zonal wind anomaly in the twice as warm minus control case. Taken from Blackmon et al. (1983).

a) The largest increase in precipitation occurs somewhat to the west of the largest SST anomalies.

b) The precipitation changes are accompanied by low-level convergence and high-level divergence.

c) The zonal wind anomalies are westerly at low levels and easterly at high levels over and to the west of the region of enhanced precipitation.

d) There is a tendency for an enhancement of westerly jetstream over the subtropical Pacific.

e) The pattern of the remote responses in the middle latitudes is similar to the observed PNA pattern.

For future reference in the present study, it is also noted that the GCM responses to the middle latitude SST anomalies, unlike those to the tropical SST anomalies, are very weak, and do not even emerge above the inherent noise levels of the models. A statistically significant response was found only when a super anomaly of magnitude ±12°C was prescribed in the North Pacific Ocean (Chervin et al., 1976).

2.2.2 Linear model studies

The GCM experiments, while very useful for certain sensitivity studies, are usually too complicated to provide specific information concerning the planetary-scale motions. For this reason simplified linear models have been developed to provide understanding. The studies by Matsuno (1966) and Gill (1980), for example, elucidate some important linear aspects of the forced planetary waves in the tropics.

Gill, in particular, explained the low-level easterly wind over the Pacific and the low-level westerly wind over the Indonesian Ocean in terms of Kelvin waves propagating eastward and Rossby waves propagating westward from the heated region. The solutions for the velocity and stream function fields obtained by Gill (1980), as shown in Fig. 2.6, nicely exhibit several of the observed features in the tropics (see legend for details).

As was evident in both observations and GCM experiments, the atmospheric forcing due to tropical SST anomaly induces not only anomalous tropical motion fields but also strong remote responses. The rather unique observed anomaly pattern outside of the forcing region was successfully simulated by several linear baroclinic models (Opsteegh and van den Dool, 1980; HK; Simmons, 1982). Hoskins and Karoly interpreted the middle and high latitude remote responses as a direct consequence of two dimensional Rossby waves propagating along a great circle path. Simmons, invoking the same dynamical mechanism, suggested that tropical heating can be a major energy source for such remote responses.

Recently, Simmons et al. (1983) have proposed that certain observed teleconnection patterns could be identified with the fastest growing mode associated with barotropic instability of the climatological upper level mean wintertime flow. They argued that the instability can be excited in a variety of ways, including not only forcing due to an anomalous tropical heating but also the dispersion of eddy energy excited by baroclinic instability or anomalous extratropical forcing. Among these forcings, however, tropical forcing is suggested to be the most effective source.

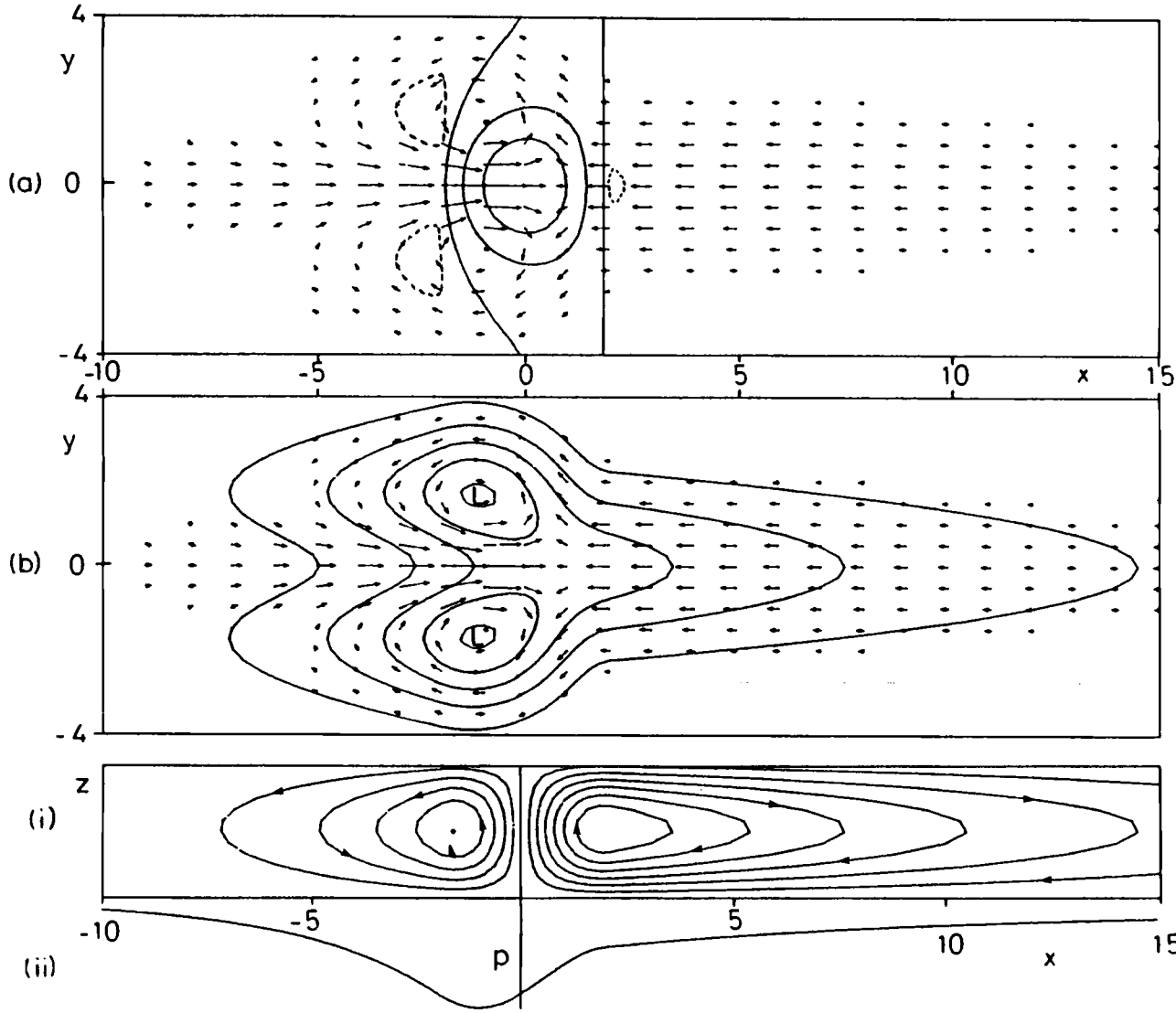

Fig. 2.6. Solution for heating symmetric about the equator in the region $|x| < 2$ for decay factor $\epsilon = 0{\cdot}1$.
(a) Contours of vertical velocity w (solid contours are 0, 0·3, 0·6, broken contour is −0·1) superimposed on the velocity field for the lower layer. The field is dominated by the upward motion in the heating region where it has approximately the same shape as the heating function. Elsewhere there is subsidence with the same pattern as the pressure field.

(b) Contours of perturbation pressure p (contour interval 0·3) which is everywhere negative. There is a trough at the equator in the easterly régime to the east of the forcing region. On the other hand, the pressure in the westerlies to the west of the forcing region, though depressed, is high relative to its value off the equator.
Two cyclones are found on the north-west and south-west flanks of the forcing region.

(c) The meridionally integrated flow showing (i) stream function contours, and (ii) perturbation pressure. Note the rising motion in the heating region (where there is a trough) and subsidence elsewhere. The circulation in the right-hand (Walker) cell is five times that in each of the Hadley cells shown in (c).
Taken from Gill (1980).

In contrast to the investigators who directly prescribe thermal forcing, Hendon and Hartmann (1982) prescribed only the internal heating and computed the surface sensible heat flux in their 12 level, linearized primitive equation model. They found that for the prescribed middle and high latitude deep diabatic heating, the inclusion of the surface heating significantly amplifies the local and remote responses, while it tends to suppress the remote response when the forcing is imposed in the subtropics. In the study by Webster (1981), on the other hand, the surface heat flux is prescribed while the internal heating due to cumulus convection is computed in his model. Webster found that for a given surface heat flux the internal heating is significantly amplified in the tropics but not in the middle latitudes. In both studies, therefore, the potential importance of thermal feedback related to either the surface heating or the internal heating is well demonstrated.

2.3 Theoretical review of the dynamics of forced planetary waves

As an aid to understanding the results of this study, it is worthwhile to review the existing dynamical theories of the forced planetary-wave motion. Since the classical work by Charney and Drazin (1961), the vertical propagation of planetary waves has been investigated by Dickinson (1968), Matsuno (1970) and many others. The main purpose of their works was an investigation of the dynamical coupling of the stratospheric and tropospheric fluctuations. Recently their ideas have been extended to investigate the dynamical coupling between the tropics and middle latitudes (Opsteegh and van den Dool, 1980; HK).

HK, in particular, examined Rossby wave propagation in a slowly varying medium using the nondivergent vorticity equation. As briefly mentioned already, the stationary wave solutions obtained by HK remarkably resemble the observed teleconnection patterns. In this section, closely following HK, we shall lay out some theoretical perspective of the present modeling study.

2.3.1 Baroclinic local responses

Here we examine the local response of a baroclinic atmosphere to a given diabatic heating using a systematic scaling similar to that of HK. Since we are interested in the stationary local response of planetary waves, the following linearized β-plane vorticity and thermodynamic equations, as used in HK, may be most appropriate for the present analysis:

$$\bar{u}\,\zeta_x' + \beta v' = f_o w_z' \tag{2.1}$$

$$f_o \bar{u} v_z' - f_o \bar{u}_z v' + w' N^2 = Q' \tag{2.2}$$

where ζ is the vorticity, f_0 the reference coriolis parameter, N the Brunt-Vaisala frequency, and Q the diabatic heating. The usual notations are used for the Cartesian coordinates and the velocities. The over-bar denotes the zonal mean and the superscript prime denotes the deviation from the mean. In (2.2) the geostrophic thermal wind relationship has been used.

For the purpose of scaling (2.1) and (2.2) the following nondimensional variables are introduced:

$$v' = V\, v^*$$
$$w' = W\, w^*$$
$$Q' = Q\, q^*$$
$$z = H\, z^* \qquad (2.3)$$

where H is the characteristic scale height, and the nondimensional variables are denoted by asterisk. Since we consider the perturbations to be driven by the diabatic heating Q', the scale height H is represented by the characteristic height of the heating. For planetary-scale motion the main balance in the vorticity equation is between the vortex streching and planetary vorticity advection terms. Accordingly, we obtain the characteristic value of W from (2.1) and (2.3).

$$W = \frac{H \beta V}{f_0} \frac{v^*}{\omega^*_{z^*}} \qquad (2.4)$$

Substitution of (2.3) and (2.4) into (2.2) after dividing by $f_0 \bar{u}_z V$ gives

$$\frac{H_u}{H} v^*_{z^*} - v^* + \gamma \frac{\omega^*}{\omega^*_{z^*}} v^* = \frac{Q}{f_0 \bar{u}_z V} Q^* \qquad (2.5)$$

where H_u is the scale height of the zonal mean velocity $H_u = \bar{u}/\bar{u}_z$, and $\gamma = \beta H H_u N^2 / f_0{}^2 \bar{u}$. Since the nondimensional variables defined in (2.3) are chosen to be of order one, the relative significance of terms in (2.5) can be easily examined in terms of the coefficients.

In the tropics where f_0 and u are small, γ is large (>>1) so that a heat source (Q > 0) away from the surface is balanced by adiabatic cooling due to upward motion. By (2.1) this implies low-level creation of vorticity ($\partial w/\partial z > 0$) which, in turn, induces poleward meridional motion. It follows that a low-level trough must be to the west of the thermal source. The opposite situation is true at the high level.

The middle latitude sitution is in complete contrast. There γ is generally small (<1). From (2.5), therefore, the heating is mainly balanced by the horizontal advection. If H is much larger than H_u (deep heating), the heating is balanced by advection of cooler air from polar region. Thus the trough must be to the east of the heat source. The southward motion, in turn, induces descending motion over the heat source resulting from vortex shrinking. For shallow heat sources $H \sim H_u$, the low-level heating is partially balanced by zonal advection with temperature gradient in the direction of flow.

2.3.2 Propagation of Rossby waves

In the previous subsection we have discussed how the atmosphere locally responds to a given heat source. We now consider how the waves can propagate outside the source region. At latitudes away from the source the response must be the particular solution of the homogeneous equations which satisfies the boundary condition at the latitude of the source. This solution includes both barotropic and baroclinic modes of stationary Rossby waves. The question is then whether the wave modes are realizable outside the source region. In this subsection we examine this question within the framework of Rossby wave dynamics.

Equations (2.1) and (2.2) can be combined into a quasi-geostropic potential vorticity equation. In order to simplify the mathematical analysis, we may further assume vertically constant zonal flow. Then, the following two-layer equations, which have similar forms to those of Pedlosky (1979, pp. 394), can be obtained.

$$\bar{u}\frac{\partial}{\partial x}\left[\frac{\partial^2\psi_1}{\partial x^2}+\frac{\partial^2\psi_1}{\partial y^2}-F(\psi_1-\psi_2)\right]+\beta\frac{\partial\psi_1}{\partial x}=0 \tag{2.6}$$

$$\bar{u}\frac{\partial}{\partial x}\left[\frac{\partial^2\psi_2}{\partial x^2}+\frac{\partial^2\psi_2}{\partial y^2}-F(\psi_2-\psi_1)\right]+\beta\frac{\partial\psi_2}{\partial x}=0 \tag{2.7}$$

where $F = f_0^2/N^2D^2$, ψ is the perturbation stream function, which satisfies $V' = k \times \nabla\psi$, and D is the depth of each layer. The subscripts 1 and 2 represent the upper and lower layers, respectively.

On the infinite x, y plane the solutions may be sought in the form of a plane wave:

$$\psi_1 = Re\left\{A_1 e^{i(kx+ly)}\right\}$$

$$\psi_2 = Re\left\{A_2 e^{i(kx+ly)}\right\} \tag{2.8}$$

Substitution of (2.8) into (2.6) and (2.7) gives two homogeneous, coupled, algebraic equations for A_1 and A_2. Then the condition for nontrivial solutions of A_1 and A_2 yields the following frequency equations:

$$\ell^2 = \frac{\beta}{\bar{u}} - k^2 \tag{2.9}$$

$$\ell^2 = \frac{\beta}{\bar{u}} - k^2 - 2F \tag{2.10}$$

The first corresponds to the barotropic mode, while the second is associated with the baroclinic mode. Since $2F \approx 4 \times 10^{-12}/m^2$ and $\beta/\bar{u} = 1 \times 10^{-12}/m^2$ in the middle latitudes, ℓ^2 is always negative in (2.10) regardless of the zonal wavenumber k. Therefore, the baroclinic mode is evanescent in latitude (trapped) and cannot propagate meridionally from the forcing region.

Since the remote response is most likely due to the barotropic Rossby wave mode, we focus on this particular mode in the following. The early theory of energy dispersion in a barotropic atmosphere (Rossby, 1945) was based on the latitudinally uniform westerly flow with the earth's sphericity approximated by a beta plane. Rossby explained how a stationary source of vorticity can propagate downstream in terms of group velocity concept. The assumption of the latitudinally uniform zonal flow is, however, hardly justified for a propagating disturbance which extends over a substantial latitudinal range. HK relaxed this restriction by assuming a slowly-varying zonal flow, and reexamined the behavior of Rossby wave propagation on the sphere. Here, we will review their theory as the main theoretical guide for the present study.

The coordinates on a Mercator projection of the sphere are defined as

$$x = a\lambda \ , \quad y = a \ln[(1+\sin\phi)/\cos\phi] \tag{2.11}$$

where λ is the longitude, ϕ the latitude, and a the earth's radius. In this coordinate system a nondivergent barotropic equation linearized about a zonal mean flow may be written as

$$\left(\frac{\partial}{\partial t} + \bar{u}_M \frac{\partial}{\partial x}\right)\left(\frac{\partial^2\psi}{\partial x^2} + \frac{\partial^2\psi}{\partial y^2}\right) + \beta_M \frac{\partial\psi}{\partial x} = 0 \tag{2.12}$$

where

$$\bar{u}_M = \bar{u}/\cos\phi$$

$$\beta_M = \frac{2\Omega}{a}\cos^2\phi - \frac{d}{dy}\left[\frac{1}{\cos^2\phi}\frac{d}{dy}(\cos^2\phi\,\bar{u}_M)\right] \tag{2.13}$$

In the above equation ψ is the stream function and Ω is the earth's rotation rate.

The plane wave solution of ψ may be used in (2.12) by assuming that the zonal mean flow varies slowly with latitude. Substituting the wave solution in (2.12) the local meridional wavenumber of a stationary wave satisfies the following relationship:

$$\ell^2 = \frac{\beta_M}{\bar{u}_M} - k^2 \tag{2.14}$$

where ℓ is the meridional wavenumber and k the zonal wavenumber. If $\beta_M/\bar{u}_M > k^2$ the meridional wavenumber is real. This corresponds to a sinusoidal wave mode which can propagate energy latitudinally. This

condition is satisfied only by westerly winds and by particular zonal wavenumbers. For easterly winds or large zonal wavenumbers, ℓ is imaginary. The amplitude of a wave in this case exponentially decays with latitude, and the wave is trapped near the source latitudes.

Since the energy of waves propagates in the direction of the local group velocity, the ray path can be given by

$$\frac{dy}{dx} = \frac{v_g}{u_g} = \frac{\ell}{k} \tag{2.15}$$

where

$$u_g = \frac{2\beta_M k^2}{k^2 + \ell^2} \quad , \quad v_g = \frac{2\beta_M k \ell}{k^2 + \ell^2}$$

In the above, u_g is the eastward group velocity and v_g is the northward group velocity.

From (2.14) and (2.15) the following observations can be made: For the case of super-rotation zonal flow, where $\bar{u}_M$ is constant and β_M is propotional to $\cos^2\phi$, (2.14) shows that for a given k the meridional wavenumber is a decreasing function of latitude. The ray path given by (2.15) then becomes more zonally oriented with latitude. In the case of realistic zonal flow, the ray path north of the jet may be thought of as analogous to that of the super-rotation case. However, south of the jet $\bar{u}_M$ is much smaller than the super-rotation flow and even negative at the tropics. In the latter case, the waves will be trapped there.

According to the solution of (2.12) obtained by HK using WKBJ method, the amplitude of a propagating wave is inversely propotional to

the square-root of meridional wavenumber. A physical interpretation of the solution is that the energy density of the wave, which propagates from south to north without dissipation or damping, should increase with latitude. This is because the area of a zonal ring in any two contiguous latitudes decreases poleward, resulting in an increase of the energy density. More details of the Rossby wave propagation in the case of climatological zonal flows will be discussed in Chapter 4.

3. MODELS

Two linear, time-dependent, spectral models developed for the present study are described in this chapter. As reviewed in Chapter 2, most of the observed planetary-scale atmospheric anomalies have been shown to have a barotropic structure. A barotropic model which is appropriate for such an anomaly study is therefore developed first. This simple model is especially useful for the purpose of investigating the dynamics of forced Rossby waves. A two-layer baroclinic model based on the primitive equations is also developed as an extention of the barotropic model. This model is intended to examine to what extent the solutions in the presence of baroclinicity resemble the simple barotropic solutions. Another important purpose of the baroclinic model is to investigate the atmospheric responses to prescribed SST anomalies by incorporating parameterized surface and internal heating mechanisms in the model.

In order to look into the transient behavior of wave responses, a time-marching scheme is used in both models. Another reason for the use of such a scheme is to fully allow the feedback of heating mechanisms in the baroclinic model. The spectral method, instead of a horizontal finite-difference method, is used in the models because of the following advantages: (1) the ease of modeling over the entire globe, (2) the reduction of computation time by using a low-order system, (3) the ease of incorporating a semi-implicit time scheme in the primitive equation model, which also reduces the computation time, (4) the easy interpretation of the wave responses in terms of the amplitude and phase.

3.1 Linear nondivergent barotropic model

The nondivergent, barotropic, vorticity equation linearized about a basic state $[\bar{u}(\phi)]$ may be written as

$$\frac{\partial \zeta'}{\partial t} + \frac{\bar{u}}{a\cos\phi}\frac{\partial \zeta'}{\partial \lambda} + \frac{1}{a\cos\phi}\frac{\partial \psi'}{\partial \lambda}\frac{\partial \bar{\eta}}{a\partial \phi} = S(\zeta') + F(\zeta') \qquad (3.1)$$

where $\zeta' = \nabla^2\psi'$

$$\bar{\eta} = f + \bar{\zeta}$$

In the above equation ζ is the relative vorticity, η the absolute vorticity, ψ the stream function, u the zonal velocity, λ the longitude, ϕ the latitude, and a the earth's radius. The over-bar denotes the zonal mean and the superscript prime denotes the deviation from the mean. The left-hand side (LHS) terms in (3.1) represent, respectively, the local change of relative vorticity, the advection of relative vorticity by the zonal mean flow, and the meridional advection of zonal mean absolute vorticity. $S(\zeta')$ represents the vorticity source which will be discussed in Chapter 4.

The dissipation term, $F(\zeta')$, includes the following two processes,

$$F(\zeta') = -\lambda\zeta' - \beta\nabla^4\zeta'$$

where λ is the linear drag coefficient and β the coefficient of biharmonic horizontal diffusion. It should be noted that the linear drag is scale independent; whereas, the biharmonic horizontal diffusion is

scale dependent. Since very little is known about the dissipation processes on the planetary-scale motion, previous investigators often used the simple drag formula with rather arbitrary coefficients; Holton (1971) used $(20\ d)^{-1}$ for λ, Matsuno (1970) used $(23\ d)^{-1}$, and Grose and Hoskins (1979) used $(14\ d)^{-1}$. In the present model, $(20\ d)^{-1}$ has been used for the coefficient. A comparision with test experiments using a coefficient of $(11.6\ d)^{-1}$ showed a lack of sensitivity in the pattern of the responses to the particular choice of the coefficient. As in Grose and Hoskins (1979), the biharmonic horizontal diffusion is included. The coefficient used in the model is $2.338 \times 10^{16} m^4 s^{-1}$. But, because of its significant scale dependency, the planetary-scale responses are affected very little by this diffusion process.

A spectral form of (3.1) may be obtained via representation of the variable ζ' in terms of orthogonal surface spherical harmonics:

$$\zeta' = \sum_{m=-M}^{M} \sum_{l=|m|}^{|m|+N} \zeta_l^m(t)\, Y_l^m(\lambda, \phi) \tag{3.2}$$

where 1. the term ζ_l^m denotes the time-dependent, generally complex, expansion coefficients.

2. $Y_l^m(\lambda, \phi) = P_l^m(\mu = \sin\phi) e^{im\lambda}$; $P_l^m(\mu)$ is an associated Legendre polynomial of the first kind normalized to unity,

$$\int_{-1}^{1} P_l^m(\mu)\, P_n^k(\mu)\, d\mu = \begin{cases} 1 & \text{for } (m, l) = (k, n) \\ 0 & \text{for } (m, l) \neq (k, n) \end{cases}$$

3. m is the zonal wavenumber, the difference l-m gives the number of nodes from pole to pole, and l is the two-dimensional "wavenumber" appropriate for the spherical geometry.

The choice of M and N in (3.2), depends on the characteristic scale of the motion under consideration. Blackmon (1976) found, in his observational study, that the long-term 500 mb geopotential variance during the northern winter is mostly due to the low-frequency fluctuations which turn out to be dominated by planetary-scale components. HK also argued that the contributions of wavenumbers higher than six to the steady-state responses were very small in their linear model experiments. Based on the above studies, M = 6 and N = 14 are used in the model because the present study concerns the planetary wave motions in a quasi-steady state. This decision is supported aposteriori by the fact that the barotropic and baroclinic model results show that the contributions of relatively small-scale waves to the quasi-steady responses are insignificant.

Substituting (3.2) into (3.1) and using the orthonormality condition over the sphere gives

$$\frac{\partial \zeta_n^k}{\partial t} = -\int_{-1}^{1} \left[\frac{ik\bar{u}}{a\cos\phi} \sum_{\ell} \zeta_\ell^k P_\ell^k - \frac{d\bar{\eta}}{d\mu} ik \sum_{\ell} \frac{\zeta_\ell^k P_\ell^k}{\ell(\ell+1)} \right] P_n^k \, d\mu$$

$$- \left[\lambda + \frac{\beta}{a^4} \{n(n+1)\}^2 \right] \zeta_n^k + S_n^k \qquad (3.3)$$

In the model the latitudinal integration in (3.3) is performed using the Gaussian quadrature formula (details in Krylov (1962)). For the exact calculation of integrals such as in (3.3) Eliasen et al. (1970) suggested that the number of Gaussian latitudes should be larger than M + 3N/2. In the present model 28 Gaussian latitudes are used which are sufficient for the integration to be exact. For the time integration a leapfrog scheme with a forward scheme every 15 time steps has been used with a 1 hour time interval. The forward scheme is needed to avoid the solution separation inherent in the leapfrog scheme (Haltiner and Williams, 1980). Comparisions with test experiments using 15 minute and 30 minute time intervals show negligible differences.

3.2 Linear primitive equation model

The basic formula of the baroclinic model developed for the present study is a linearized version of the primitive equation model described by Hoskins and Simmons (1975). It uses spherical harmonics in the horizontal, a second-order finite difference method in the vertical, and a semi-implicit time scheme.

3.2.1 Formulation of the model

The linearized primitive equations in σ-coordinates may be written:

$$\frac{\partial \zeta'}{\partial t} = -\frac{1}{\cos^2\phi}\frac{\partial A}{\partial \lambda} - \frac{1}{\cos\phi}\frac{\partial B}{\partial \phi} + F_{\zeta'} \qquad (3.4)$$

$$\frac{\partial D'}{\partial t} = \frac{1}{\cos^2\phi}\frac{\partial B}{\partial \lambda} - \frac{1}{\cos\phi}\frac{\partial A}{\partial \phi} + \nabla^2\left(\frac{\bar{U}U'}{\cos^2\phi} + \Phi' + RT_o \ln P_s'\right) + F_{D'} \tag{3.5}$$

$$\frac{\partial T'}{\partial t} = -\frac{1}{a\cos^2\phi}\frac{\partial}{\partial \lambda}\left(\bar{U}T' + U'\bar{T}^*\right) - \frac{1}{a\cos\phi}\frac{\partial}{\partial \phi}\left(V'\bar{T}^*\right) + \bar{T}^* D' - \dot{\sigma}'\frac{\partial \bar{T}}{\partial \sigma} + \frac{\kappa \bar{T}}{P}\omega' + \frac{Q'}{c_p} + F_{T'} \tag{3.6}$$

$$\frac{\partial \ln P_s'}{\partial t} = -\int_0^1 \left[\frac{1}{\cos^2\phi}\frac{\bar{U}}{a}\frac{\partial \ln P_s'}{\partial \lambda} + \frac{1}{\cos\phi}\frac{V'}{a}\frac{\partial \ln P_s'}{\partial \phi} + D'\right] d\sigma \tag{3.7}$$

$$\frac{\partial \Phi'}{\partial \ln \sigma} = -RT' \tag{3.8}$$

where $U = u\cos\phi$, $V = v\cos\phi$

$$A = \frac{\bar{U}}{a}\zeta' + \frac{U'}{a}\bar{\eta} + \frac{R}{a^2}\bar{T}^*\cos\phi\frac{\partial \ln P_s}{\partial \phi} + \frac{R}{a^2}T'\cos\phi\frac{\partial \overline{\ln P_s}}{\partial \phi}$$

$$B = \frac{V'}{a}\bar{\eta} - \dot{\sigma}'\frac{\partial}{\partial \sigma}\left(\frac{\bar{U}}{a}\right) - \frac{R\bar{T}^*}{a^2}\frac{\partial \ln P_s'}{\partial \lambda} \tag{3.9}$$

D is the divergence, Φ the geopotential, P the pressure, P_s the surface pressure, and T the temperature. $\bar{T}(\phi) = \bar{T}_o + \bar{T}^*(\phi)$, where T_o is the global mean temperature at each layer. $\sigma = p/p_s$ is the vertical coordinate. R is the gas constant, c_p the isobaric specific heat of air, and $\kappa = R/c_p$. $Q(\lambda, \phi, \sigma)$ is the total diabatic heating rate which will be discussed in Chapters 5 and 6. Equations (3.4)-(3.8) are,

respectively, the vorticity, divergence, thermodynamic, continuity, and hydrostatic equations.

$F_{\zeta'}$, $F_{D'}$, and $F_{T'}$ represent the dissipative processes which have the same form as in the barotopic model

$$F_{\zeta'} = -\lambda_u(\sigma)\zeta' - \beta\nabla_H^4\zeta'$$

$$F_{D'} = -\lambda_u(\sigma)D' - \beta\nabla_H^4 D' \qquad (3.10)$$

$$F_{T'} = -\lambda_T T' - \beta\nabla_H^4 T'$$

The exponentially decaying processes, represented by the first terms of right-hand side (RHS) in (3.10), are Rayleigh friction for the motion field and Newtonian-type radiative cooling for the temperature. The Rayleigh frictional coefficients used in the model are λ (σ = 0.75) = 7.5×10^{-7}/sec and λ (σ = 0.25) = 4.6×10^{-7}/sec, which correspond to 15 day and 25 day decay rates, respectively. We have chosen the above values by considering surface friction in relation to the drag coefficient of present barotropic model. For the cooling of the earth's atmosphere Schneider and Lindzen (1977) found that the e-folding radiative time is about 20 days and is approximately constant throughout the troposphere. Their estimate was based on the radiative calculations by Rogers and Walshaw (1966). Tung and Lindzen (1979) also estimated the radiative time scale and suggested four weeks for long waves. We therefore have chosen $(25\ d)^{-1}$ as the coefficient of Newtonian cooling for both layers.

The model variables are represented in the horizontal by truncated series of spherical harmonics whose details will be discussed in the next section, and the vertical derivatives are approximated by the finite-difference analogues of second-order accuracy. The arrangement of the variables in the vertical is shown in Fig. 3.1. The vorticity, divergence, geopotential and temperature are carried at the middle of each layer, σ = (0.25 and 0.75). The sigma velocity $\dot{\sigma}$ is calculated only at σ = 0.5 with the boundary condition $\dot{\sigma}$ = 0 at σ = 0 and 1.

The vertical difference scheme, introduced in Appendix A, gives finite-difference analogues of (3.4)-(3.8) of the forms:

$$\frac{\partial \mathfrak{Z}}{\partial t} = \mathbf{N} \tag{3.11}$$

$$\frac{\partial \mathbf{D}}{\partial t} = \mathbf{\Pi} - \nabla^2\left(\mathbf{\Phi}' + \mathbf{T}_0 \ell n P_s' \right) \tag{3.12}$$

$$\frac{\partial \mathbf{T}}{\partial t} = \mathbf{\Gamma} - \tau \mathbf{D}' \tag{3.13}$$

$$\frac{\partial \ell n P_s'}{\partial t} = \mathbf{P} - \mathbf{p} \mathbf{D}' \tag{3.14}$$

$$\mathbf{\Phi}' - \mathbf{\Phi}_s = \mathfrak{g} R \mathbf{T}' \tag{3.15}$$

where $\mathfrak{z}'$, $\mathbf{D}'$, $\mathbf{T}'$, $\mathbf{T}_0$, $\mathbf{\Phi}'$, $\mathbf{N}$, $\mathbf{\Pi}$, $\mathbf{\Gamma}$; column vectors

$\mathfrak{g}$, τ ; constant matrices

P, ℓnP ; scalars

$\mathbf{p}$; row vector

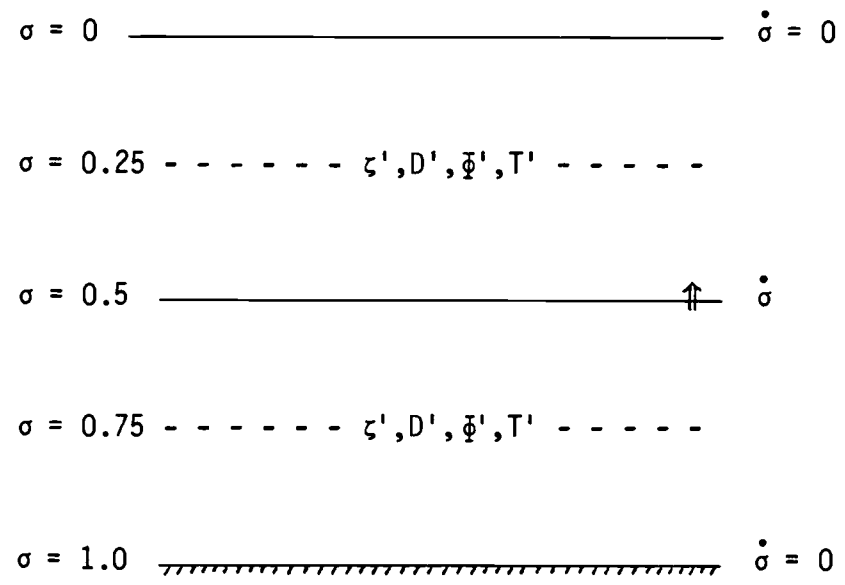

Fig. 3.1. Vertical structure of the baroclinic model.

The matrices, vectors, and scalars in the above equations are defined in Appendix B. Because there are two layers in the vertical, the vectors are 2-dimensional and the matrices are 2 x 2.

A semi-implicit time scheme has been used for the time integration of (3.12)-(3.15). This scheme treats implicitly those terms in the equations that are primarily responsible for the propagation of gravity waves. Robert (1969) initially applied the scheme to the spectral model with a primitive barotropic equation. Subsequently, it has been developed by Hoskins and Simmons (1975) and Bourke et al. (1977) for the use in a multi-level spectral primitive equation model. In a manner similar to that of Hoskins and Simmons (1975), a semi-implicit scheme is applied in the present model as follows: By averaging in time for the pressure gradient and divergence terms in (3.12)-(3.15),

$$\delta_t D' = \Pi - \nabla^2 (\overline{\Phi'}^t + T_0 \overline{\ln p_s'}^t) \tag{3.16}$$

$$\delta_t T' = \Gamma - \tau \overline{D'}^t \tag{3.17}$$

$$\delta_t \ln p_s' = P - \rho \overline{D'}^t \tag{3.18}$$

where the following notations have been used for the representations at discrete times

$$\delta_t X = (X^{t+\Delta t} - X^{t-\Delta t}) / 2\Delta t$$

$$\overline{X}^t = (X^{t+\Delta t} + X^{t-\Delta t}) / 2$$

Elimination of $\Phi'^{(t+\Delta t)}$ and $\ell n P_s'^{(t+\Delta t)}$ in (3.16) using (3.15), (3.17) and (3.18) gives

$$\left[\mathbf{I} - R(g\tau + T_0 P)\Delta t^2 \nabla^2 \right] \overline{D'}^t$$

$$= D'^{(t-\Delta t)} + \Delta t \left[\Pi - \nabla^2 (\Phi'^{(t-\Delta t)} + R T_0 \ell n P_s'^{(t-\Delta t)}) \right]$$

$$- R \Delta t^2 \nabla^2 (g T + T_0 P) \qquad (3.19)$$

This equation can be solved for $\overline{D'}^t$. Then, the temperature and surface pressure at the new time step can be obtained from (3.17) and (3.18) by substituting $\overline{D'}^t$. For the time integration a one hour time step has been used in the present baroclinic model. Comparisons with test experiments using 15 minute and 30 minute time steps showed only minor differences.

3.2.2 Spectral representation

Using finite differences in the vertical and the semi-implicit scheme, (3.19) is obtained from the original primitive equations. We now solve (3.19) in a horizontally truncated system. The variables in each layer may be represented in terms of spherical harmonics Y_ℓ^m as follows:

$$\{ \Psi, \chi, \Phi, T, \ell n P_s \}$$

$$= \sum_{m=-M}^{M} \sum_{\ell=|m|}^{|m|+N} \{ a^2 \Psi_\ell^m, a^2 \chi_\ell^m, \Phi_\ell^m, T_\ell^m, (\ell n P_s)_\ell^m \} Y_\ell^m(\lambda, \phi) \qquad (3.20)$$

and

$$\{U, V\} = a \sum_{m=-M}^{M} \sum_{l=|m|}^{|m|+N+1} \{U_l^m, V_l^m\} Y_l^m(\lambda, \phi) \tag{3.21}$$

In the above the superscript primes for perturbation quantities have been dropped for convenience. The horizontal truncation used in the present model is the same as that of the barotropic model described in the previous section.

The wind vector $\mathbf{V}$ is now defined in terms of the stream function ψ and velocity potential χ.

$$\mathbf{V} = \mathbf{k} \times \nabla\psi + \nabla\chi$$

Accordingly, the quantities ζ and D can be expressed as

$$\zeta = \nabla^2\psi \ , \quad D = \nabla^2\chi \tag{3.22}$$

The diagnostic relationships for U_l^m and V_l^m then become

$$U_l^m = (l-1)\,\varepsilon_l^m \psi_{l-1}^m - (l+2)\,\varepsilon_{l+1}^m \psi_{l+1}^m + i m \chi_l^m \tag{3.23}$$

$$V_l^m = -(l-1)\,\varepsilon_l^m \chi_{l-1}^m + (l+2)\,\varepsilon_{l+1}^m \chi_{l+1}^m + i m \psi_l^m \tag{3.24}$$

where $\varepsilon_l^m = \left[(l^2 - m^2)/(4l^2 - 1) \right]^{1/2}$

Using (3.20) and (3.21) the spectral representation of (3.19) may be written:

$$A_\ell \overline{\chi_\ell^m}^t = \chi_\ell^{m(t-\Delta t)} - \frac{1}{C_\ell} R_\ell^m \tag{3.25}$$

where

$$C_\ell = \ell(\ell+1)$$

$$A_\ell = I + C_\ell \frac{R}{a^2}(g\tau + T_0 p)\Delta t^2$$

$$R_\ell^m = \Delta t\left[\pi_\ell^m - \frac{C_\ell}{a^2}\Phi_\ell^{m(t-\Delta t)} + C_\ell \frac{R}{a^2} T_0 (\ell n P_s')_\ell^{m(t-\Delta t)}\right]$$

$$+ \Delta t^2 \frac{R}{a^2} C_\ell (g\Gamma_\ell^m - T_0 P_\ell^m)$$

The velocity potential at t + Δt can then be calculated using the following equation,

$$\chi_\ell^{m(t+\Delta t)} = -\chi_\ell^{m(t-\Delta t)} + 2A_\ell^{-1}(\chi_\ell^{m(t-\Delta t)} - \frac{1}{C_\ell} R_\ell^m) \tag{3.26}$$

Since A_ℓ is a constant matrix this inversion needs to be computed only once. Using (3.22) and (3.26) we can obtain $\overline{D_\ell^m}^t$. Then the prognostic variables T_ℓ^m and $(\ell n P_s)_\ell^m$, can be obtained from (3.17) and (3.18), calculated directly from (3.11) using the leapfrog scheme. The diagnostic variables Φ_ℓ^m, U_ℓ^m, and V_ℓ^m, can then be obtained from (3.15), (3.23) and (3.24), respectively.

4. FORCED WAVE RESPONSES IN BAROTROPIC ATMOSPHERES

In this chapter the forced wave responses in simple barotropic atmospheres are investigated by experiments with the present barotropic model and by the theory of Rossby wave propagation (HK). The specific issues studied in this chapter are as follows. The first section focuses on a theoretical consideration of the forced Rossby waves superimposed on climatological zonal flows. In the next section the barotropic model described in Chapter 3 is checked by comparing the model responses to the analytic solutions. Using the model the responses to isolated vorticity sources located at various latitudes are calculated, and their local and remote responses are interpreted in terms of the wave dynamics. In the final portion of this chapter an attempt to explain some of the characteristics of the observed teleconnection patterns is made using the model responses to the wavenumber-dependent forcings.

Two zonal-mean flows derived from the January climatology as available from NCAR are used as the basic state of the model. One basic state is chosen to be the climatological 250 mb level wind because the upper-level response of the present baroclinic model resembles a Rossby wave train. Another basic state is obtained by averaging the climatological 250 mb and 750 mb zonal flows. Since this basic state is very similar to the 500 mb zonal flow, hereafter, we call this state "the 500 mb basic state."

4.1 Characteristics of forced Rossby waves in climatological zonal flows

The characteristics of the zonal flows for excitation and propagation of Rossby waves are studied in this section. The latitudinal propagation of Rossby waves can be examined using a stationary wavenumber aK_s which is defined as

$$aK_s = a\sqrt{k^2+\ell^2} = a\sqrt{\frac{\beta_M}{\bar{u}_M}} \tag{4.1}$$

the latter from (2.14). In the above the meridional wavenumber ℓ is real if k is less than K_s. For such a condition the waves can propagate energy latitudinally.

The latitudinal distributions of aK_s, $\bar{u}_M$ and β_M are shown in Fig. 4.1a for the 250 mb zonal flow. In the tropics aK_s has imaginary value (not shown) due to the easterly flow, therefore, all wavenumber components are trapped. β_M has a large value near the northern hemisphere jet and decreases poleward more rapidly than $\bar{u}_M$. As a result aK_s decreases from a value of about 6 in the jet to less than 3 in the high latitudes. Thus, we expect that the waves with zonal wavenumber larger than 3 will be trapped by the northern flank of the jet, while longer waves can propagate to the high latitudes. In particular, it appears that only waves with zonal wavenumber 1 can propagated into the polar region.

The same calculation has been made for the 500 mb basic state, and as shown in Fig. 4.1b, the patterns of aK_s, $\bar{u}_M$ and β_M are very similar

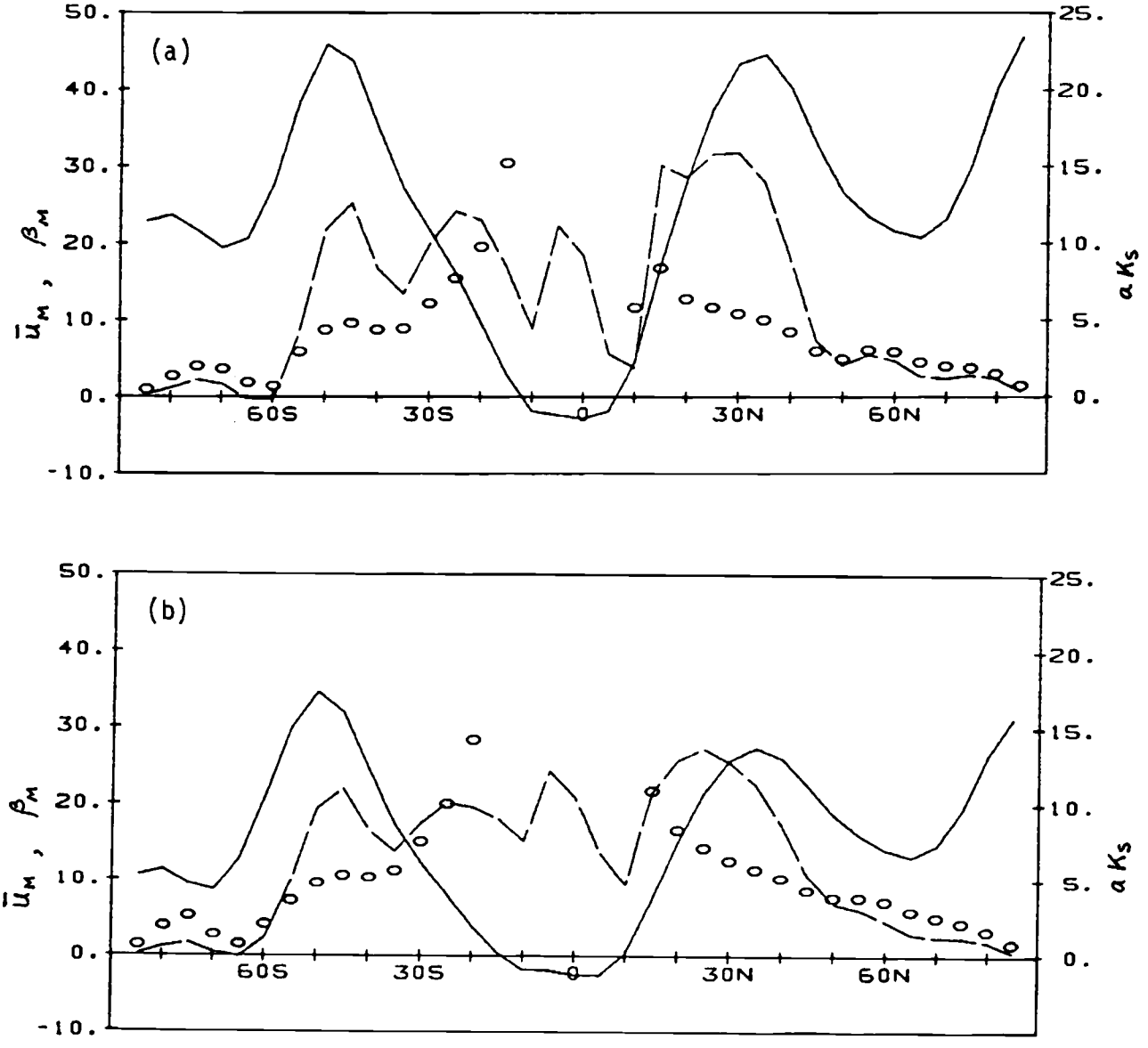

Fig. 4.1. Latitudinal distributions of aK_s, $\bar{u}_M$, and β_M for (a) the 250 mb basic state and (b) the 500 mb basic state. aK_s is shown by the circles, and $\bar{u}_M$ and β_M are represented by the solid and broken lines, respectively. Units for aK_s, $\bar{u}_M$, and β_M are wavenumber, m/sec, and 10^{-12}/sec • m, respectively.

to those for the 250 mb basic state. The main differences are that $\bar{u}_M$ and β_M are somewhat smaller over most of the latitudes compared with those for the 250 mb zonal flow. However, aK_s is somewhat larger which indicates that there is more chance for smaller scale waves to propagate to the high latitudes at the 500 mb level than at the 250 mb.

We now examine the characteristic response of Rossby waves to the forcing of each wavenumber component for the basic states examined above. Although $\bar{u}_M$ and β_M depend on the latitude, a plane wave solution may be used to examine the local characteristics of the forced waves. Substituting a plane wave solution in (2.12) gives for the amplitude of the wave for a steady state

$$\hat{\psi}_{k,\ell} = \frac{-i\,\hat{S}_{k,\ell}}{k[-\bar{u}_M(k^2+\ell^2)+\beta_M]} \tag{4.2}$$

where $\hat{S}_{k,\ell}$ is the amplitude of vorticity forcing for wavenumber k and ℓ. In a Mercator projection of the sphere, k and ℓ may be defined as

$$k = \frac{m}{a}, \quad \ell = \frac{\cos\phi}{a} n$$

where m is the zonal wavenumber and n is the meridional wavenumber. For a given forcing $\hat{S}_{k,\ell}$, the wave amplitude will depend upon the absolute magnitude of the denominator in (4.2). In particular, wave resonance occurs when the denominator is zero.

The latitudinal distributions of the denominator $k[-\bar{u}_M(k^2 + \ell^2) + \beta_M]$ for the 250 mb zonal flow are shown in Fig. 4.2 for selected zonal and meridional wavenumber components. A distinctive

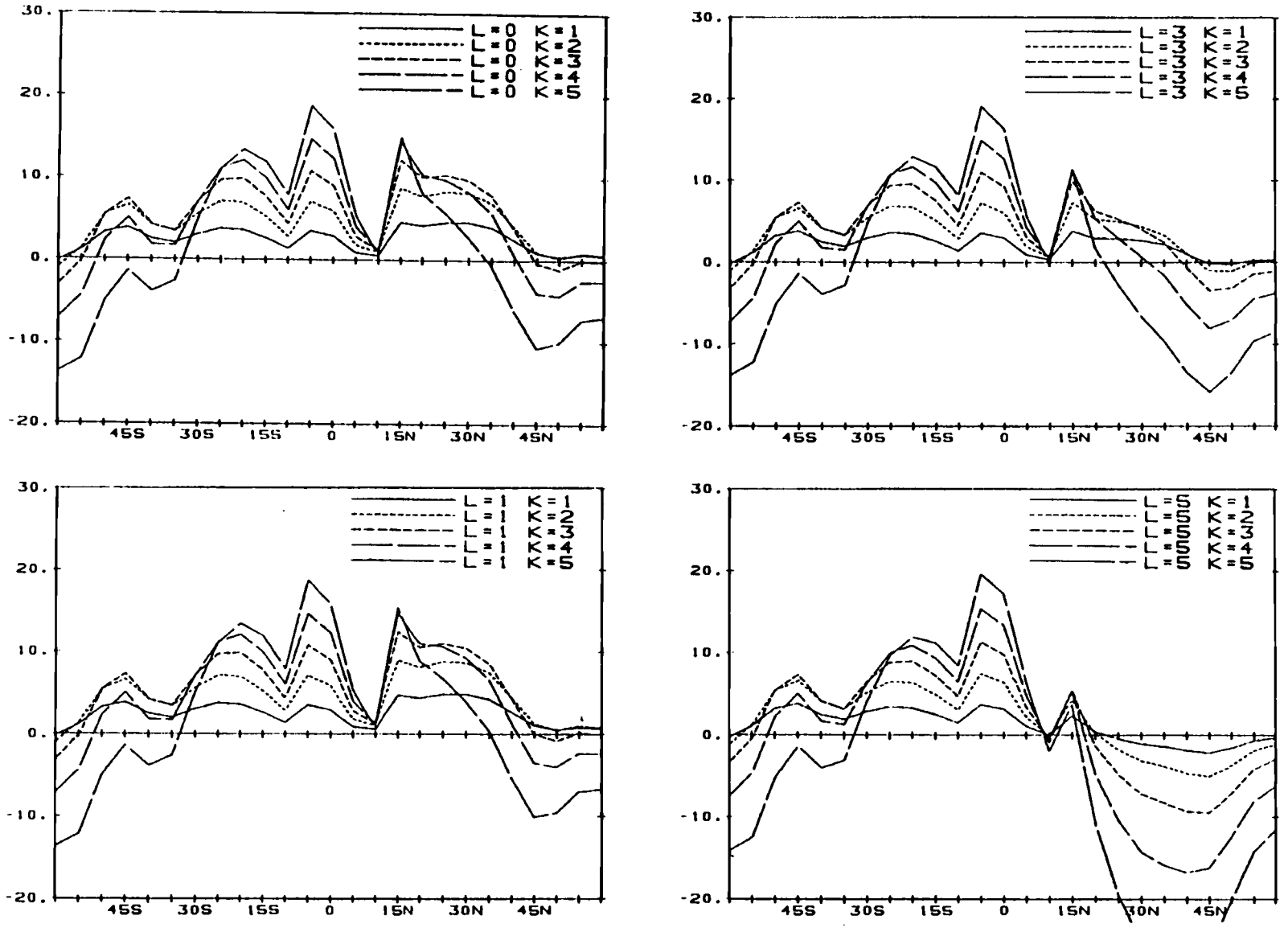

Fig. 4.2. Latitudinal distribution of $k[-\bar{u}_M(k^2 + \ell^2) + \beta_M]$ for each wavenumber k and ℓ. The 250 zonal flow is used for $\bar{u}_M$ and β_M. In each figure, ℓ is fixed and each line is for m =(1, 5). Unit is 10^{-18}/sec · m .

pattern for all wavenumber components is that a minimum occurs at 10°N, and maxima occur at 15°N and 5°S. Another minimum occurs for zonal wavenumbers 1 and 2 in high latitudes north of 45°N. This minimum has a broad latitudinal structure. The minima in the Northern (winter) Hemisphere, are not found at the corresponding latitudes in the Southern (summer) Hemisphere. In the middle latitudes the magnitudes are larger in the winter hemisphere than in the summer hemisphere. It should also be noted that for a given meridional wavenumber, the magnitude increases with zonal wavenumber at most latitudes.

From the above results we expect that the responses are dominated by small zonal wavenumber components, and the large responses mainly occur for the sources located in the subtropics and high latitudes. A middle latitude source in the winter hemisphere is expected to excite the waves of relatively small amplitude. In addition, for a given forcing the wave responses in the winter hemisphere will be generally stronger than in the summer hemisphere.

The calculations have also been made using the 500 mb basic state. As shown in Fig. 4.3, the characteristic wave responses in this basic state are similar to those in the 250 mb basic state. The main difference is that the minima at 10°N are not as distintive as in the 250 mb zonal flows. This implies that a subtropical vorticity source may not excite the waves of large amplitude in the 500 mb zonal flow.

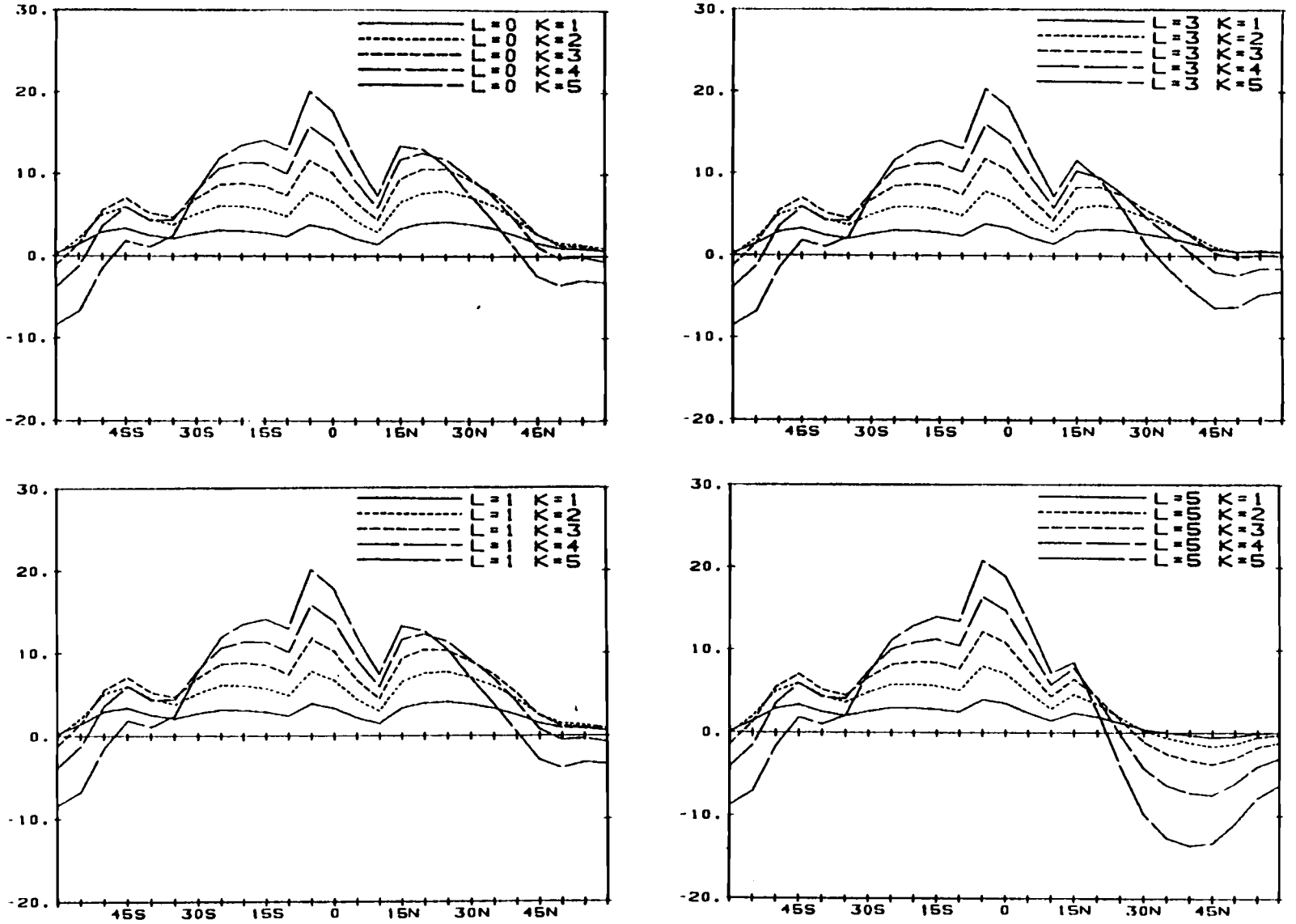

Fig. 4.3. As in Fig. 4.2 except for the 500 mb basic state.

4.2 The responses to isolated vorticity sources

4.2.1 Super-rotation basic state

The linearized vorticity equation in spherical coordinates can be solved analytically with an isolated vorticity source when the basic state is a super-rotation flow. This solution is obtained here to check the numerical solution and to look into the wave responses for this idealized zonal flow.

In a super-rotation flow, the zonal velocity and its latitudinal gradient of absolute vorticity can be written as

$$\bar{u} = a \cos\phi \, \Omega'$$

$$\frac{d\bar{\eta}}{\cos\phi \, d\phi} = 2(\Omega + \Omega') \tag{4.3}$$

where Ω' is the angular velocity of the super-rotation flow. Here we choose $\Omega' = 11.66°/\text{day}$ because this is analogous to the globally averaged angular velocity of the 300 mb zonal flow during the wintertime (Hoskins et al., 1977). Substitution of (4.3) into (3.3) without the biharmonic diffusion gives

$$\frac{\partial \zeta_n^k}{\partial t} = -i \omega_n^k \zeta_n^k + S_n^k \tag{4.4}$$

where

$$\omega_n^k = k\left[\Omega' - 2(\Omega + \Omega')/n(n+1)\right] - i\lambda$$

Assuming the initial perturbation vorticity to be zero, the solution of (4.4) may be written as

$$\zeta_n^k(t) = -\frac{i\,S_n^k}{\omega_n^k}\left(1 - e^{-i\omega_n^k t}\right) \tag{4.5}$$

Then, the analytic solution for vorticity can be obtained by substituting (4.5) into (3.2).

$$\zeta' = \sum_{k=-M}^{M} \sum_{n=|m|}^{|m|+N} \frac{i\,S_n^k}{\omega_n^k}\left(e^{i(k\lambda-\omega_n^k t)} - e^{ik\lambda}\right) P_n^k(\mu) \tag{4.6}$$

Using the above equation, we can calculate the global response of vorticity at any time point if the spectral components of vorticity source S_n^k are known.

For the atmospheric forcing in this study we shall use the following elliptical formula unless otherwise stated.

$$S(\lambda,\phi) = \begin{cases} A\left\{\sin\dfrac{\pi(\theta-\theta_1)}{(\theta_2-\theta_1)}\sin\dfrac{\pi(\lambda-\lambda_1)}{(\lambda_2-\lambda_1)}\right\}^2, & \lambda_1<\lambda<\lambda_2,\ \theta_1<\theta<\theta_2 \\ 0 \quad \text{otherwise} \end{cases} \tag{4.7}$$

In the above, A is the magnitude of the maximum forcing, $\theta_1 = \theta_0 - 15°$, $\theta_2 = \theta_0 + 15°$ where θ_0 is the latitude of the maximum forcing, and $\lambda_1 = 135°E$, $\lambda_2 = 135°W$. Since the responses are linearly proportional to the magnitude of forcing in a linear model, A has been chosen with a rather arbitrary value. In this section $A = -1 \times 10^{-10}/sec^2$ and

θ_0 = 15°N are used. The spectrally truncated field of the present forcing is shown in Fig. 4.4.

The analytic solution for the steady state stream function response to the forcing (when $e^{-\lambda t} \to 0$) is displayed in Fig. 4.5. It is evident in this figure that the wave responses are consistent with the Rossby wave ray theory described in section 2.3; outside the forcing region the ray path (dotted line) is more zonally oriented with increasing latitude, the meridional scale of the waves increases with latitude, and the largest remote responses occur in high latitudes.

We now compare the analytic solution with the barotropic model response. Figures 4.6a and b show the responses of stream function at day 20 for the analytic and numerical solutions respectively. The differences between these two figures are apparently negligible. The comparision thus indicates that in the present numerical model the 28 Gaussian latitudes are sufficient to make an exact latitudinal integration, and that the time truncation is negligible.

4.2.2 Climatological basic states

The problem described above is for a barotropic atmosphere in super-rotation. We now investigate the responses of Rossby waves superimposed on the climatological 250 mb zonal flow. The vorticity source prescribed in the model has the same distribution as that expressed by (4.7).

In order to look into the transient behavior, the stream function response to the source centered at 15°N and 180°E is shown at 5-day intervals in Fig. 4.7. Apparently, these figures show the waves

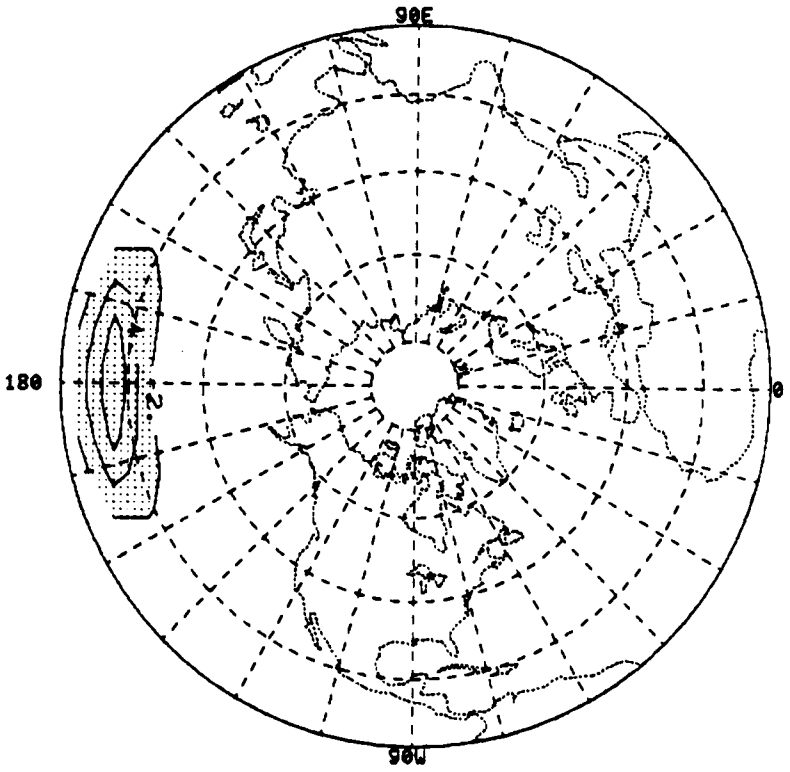

Fig. 4.4. Vorticity forcing field represented by 6 Fourier components and 15 associated Legendre polynomials. Contour interval is $10^{-11}/sec^2$.

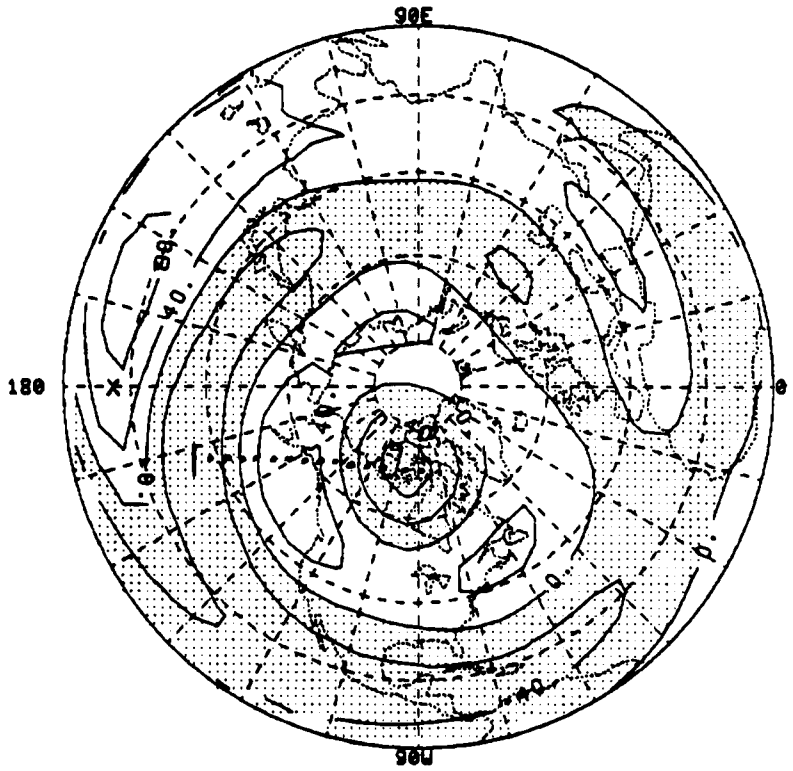

Fig. 4.5. Analytic solution of stream function in a steady-state response to the vorticity source shown in Fig. 4.4. Stippled area denotes the negative response regime. Contour interval is 4×10^6 m^2/sec. x shows the location of the vorticity source.

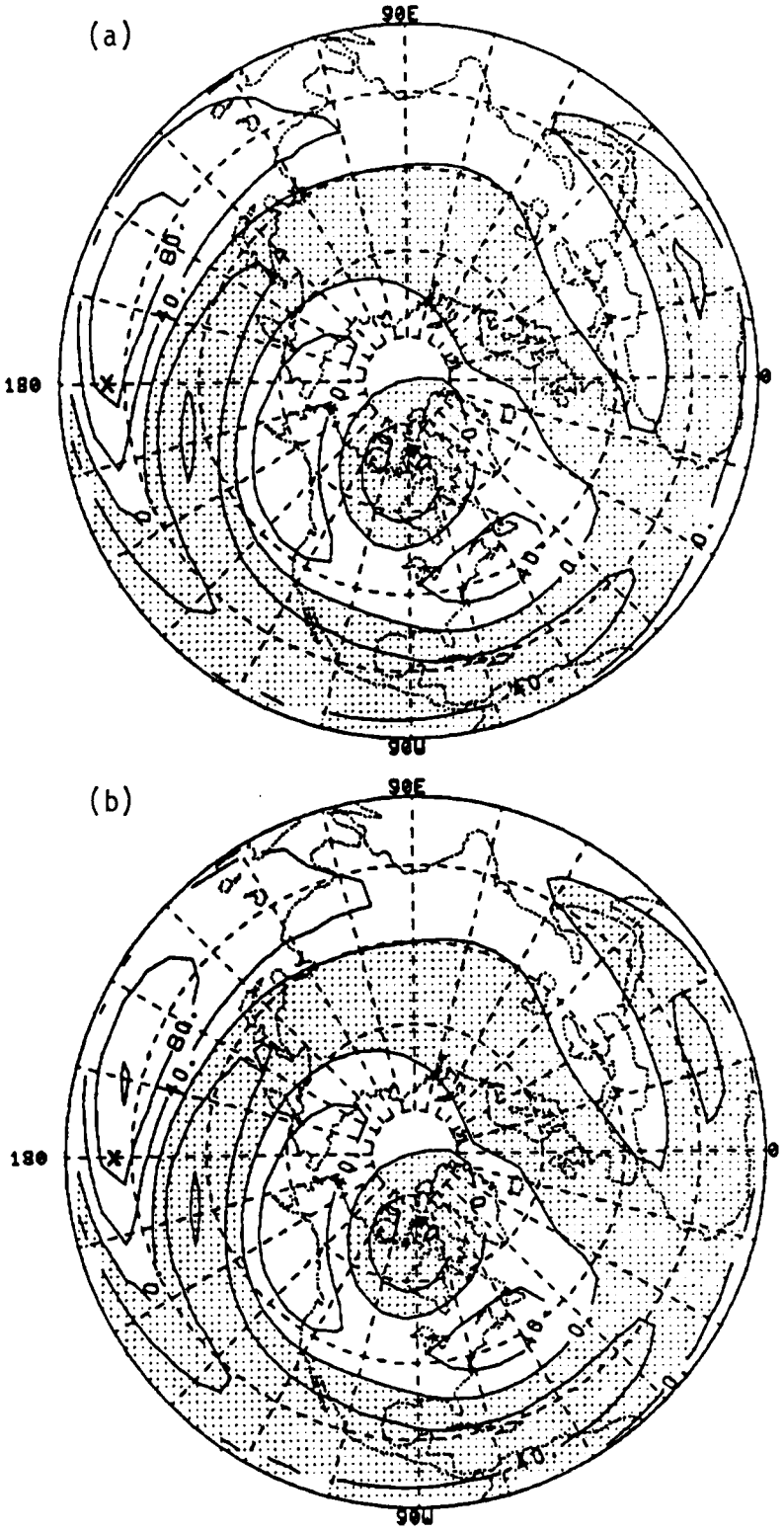

Fig. 4.6. Stream function response at day 20.
(a) Analytic solution. (b) Numerical solution.
Unit: 10^5 m^3/sec. x shows the location of the vorticity source.

propagating along two great circle wavetrains. At day 10, about 60° downstream at 55°N there is a sign of a split in the wavetrain with the longer waves continuing polewards and the shorter waves turning equatorwards. Because the group velocity is proportional to the wavenumber, the equatorward wavetrain is set up much earlier than the poleward wavetrain. It should be noted that the waves have small amplitudes far downstream due to dissipation, and they hardly return to the source region thereby avoiding resonance. Another interesting feature is that the equatorward wavetrain resembles the PNA pattern. This result may also support the previous studies in which this pattern is suggested to be a consequence of the upper-level anticyclonic anomaly over the subtropical central Pacific caused by anomalous tropical heating (Horel and Wallace, 1981). After day 15 the pattern of the response does not change significantly which shows that the quasi-steady state has then been reached. However, for the purpose of presentation, a 15 day time mean running from day 5 to day 20 has been taken for the subsequent results in this chapter.

The stream function response to the latitudinal position of the vorticity source is examined by prescribing the anticyclonic source to be at various latitudes in the model. Figures 4.8a, b, c, and d show the time mean responses to the vorticity sources centered at 0°, 15°N, 30°N, and 45°N, respectively. For the source in the tropics, a positive stream function response is generated to the west of the source. For the middle latitude source, on the other hand, the positive response occurs over the source region. These local responses may be explained in terms of vorticity balance for the steady state. In

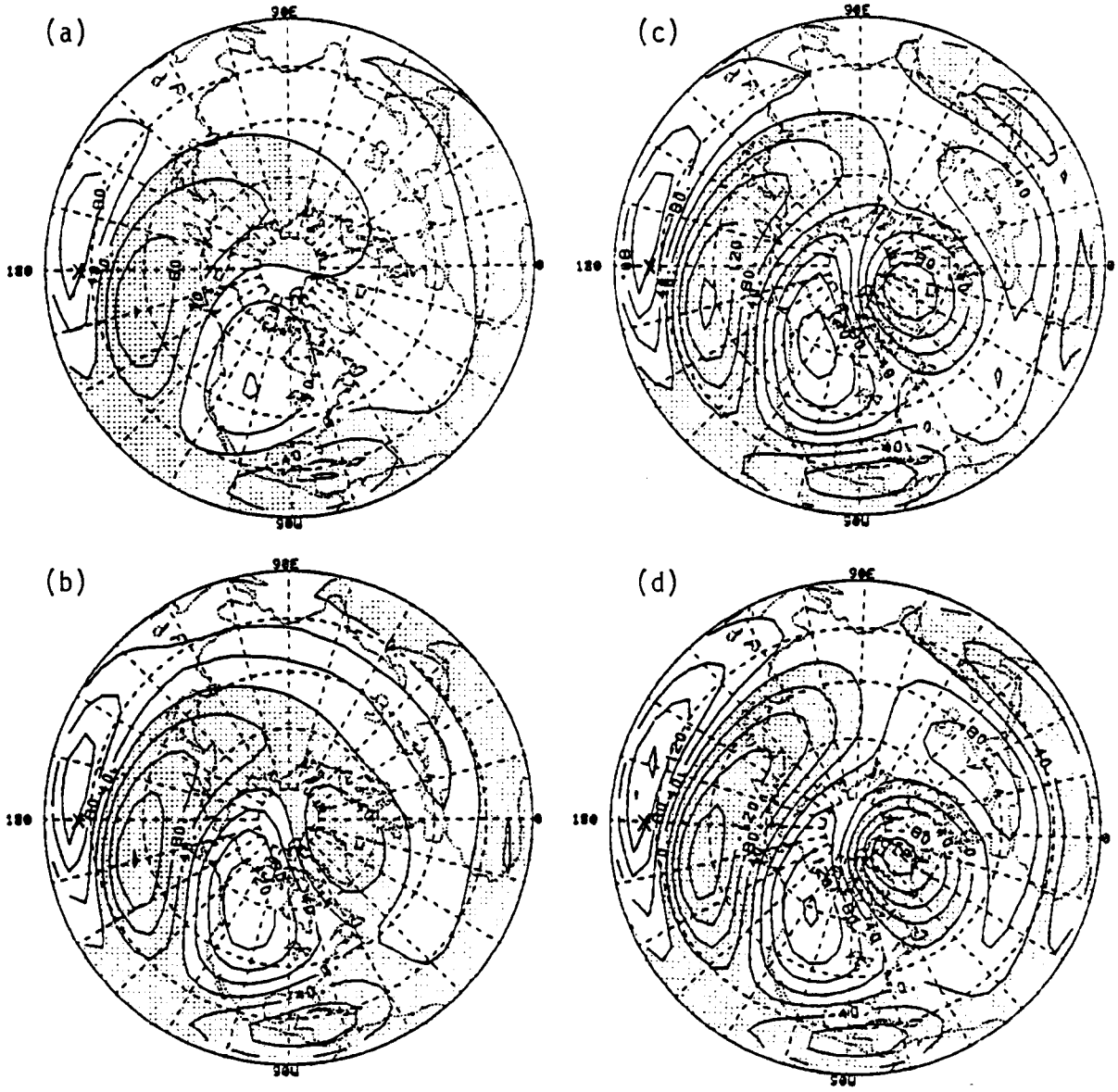

Fig. 4.7. Stream function response to the vorticity source centered at 15°N, 180°E. Shown are the responses at (a) day 5, (b) day 10, (c) day 15, and (d) day 20. Contour intervals are 4×10^6 m^2/sec. x shows the location of the vorticity source.

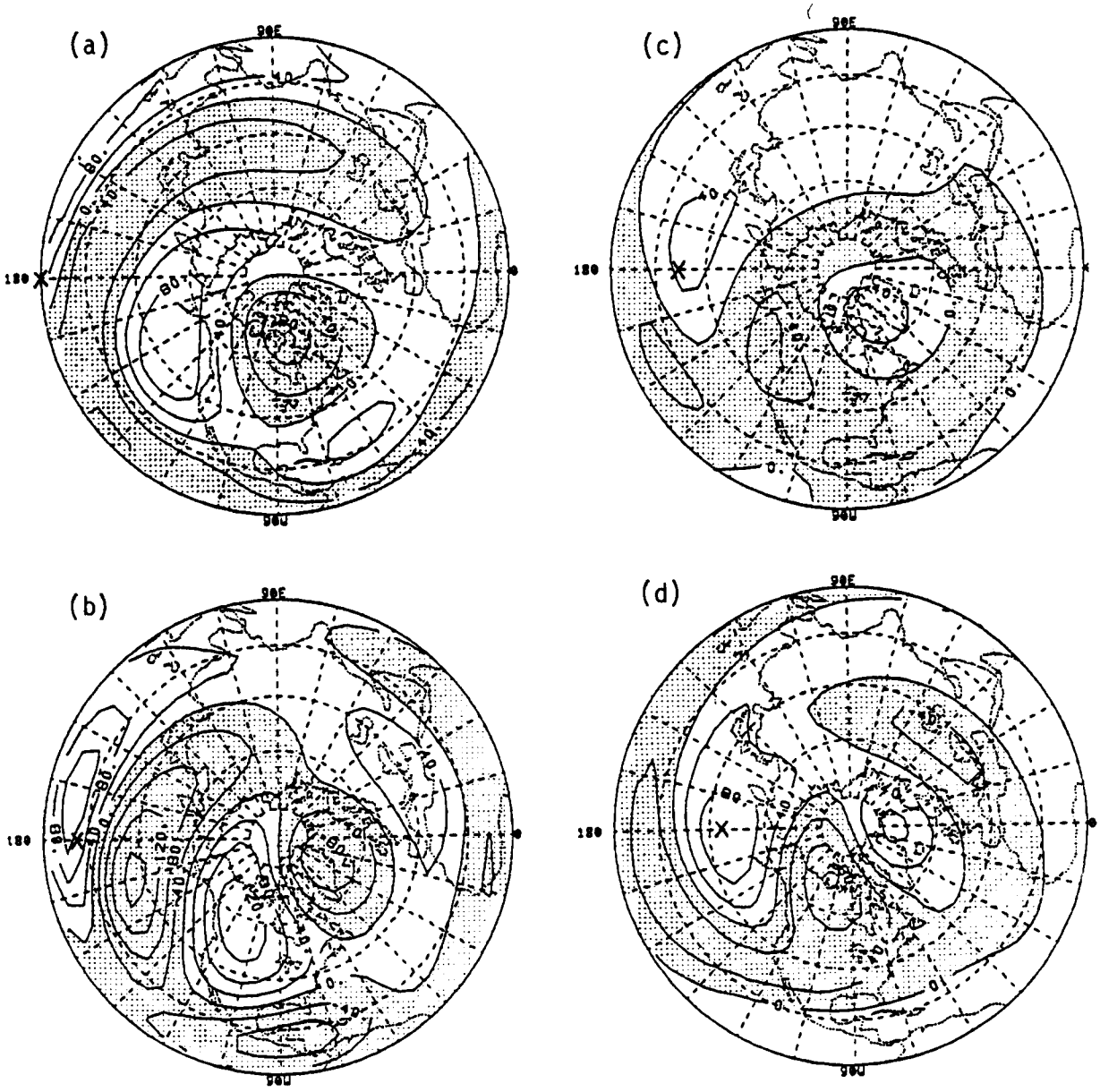

Fig. 4.8. The 15-day mean stream function in response to the vorticity source centered at (a) 0°N, (b) 15°N, (c) 30°N, and (d) 45°N. Contour intervals are 4 x 10^6 m^2/sec. x shows the center of the anticyclonic vorticity source.

the tropics where $\bar{u}$ is small and β is large, the anticyclonic vorticity source should be balanced by planetary (cyclonic) vorticity advection. Therefore, the center of positive stream function locates to the west of the source. For the middle latutude source, both advection terms in the equation are comparable but with opposite signs near the source. Thus, west of the source the zonal advection balances the sum of the negative source and planetary vorticity advection, while east of the source the planetary vorticity advection balances the other two terms. Stronger meridional motion, therefore, should be maintained to the east of the source than to the west. Such balances result in the stream function pattern shown in Fig. 4.8d.

An inspection of Figs. 4.8a-d indicates that the intensity of the response is highly sensitive to the location of prescribed source. The sources centered at 15°N and 45°N excite the waves of relatively large amplitudes (Fig. 4.8b and d), whereas the reponse to the source centered at 30°N is small (Fig. 4.8c). The reason for this small response is that any local forcing near the jet is mainly balanced by the zonal advection instead of the local growth of the perturbation. The dependence of the magnitude of the response on the location of the source is also consistent with what we discussed in the previous section using Fig. 4.2. It is also interesting to note that since the energy tends to be dispersed when it propagates from north to south on a sphere, the large responses are located at latitudes north of the source.

The same calculations have been made for the 500 mb basic state. As shown in Fig. 4.9 the responses are similar to those of Fig. 4.8 except for the following features. In the middle and high latitudes

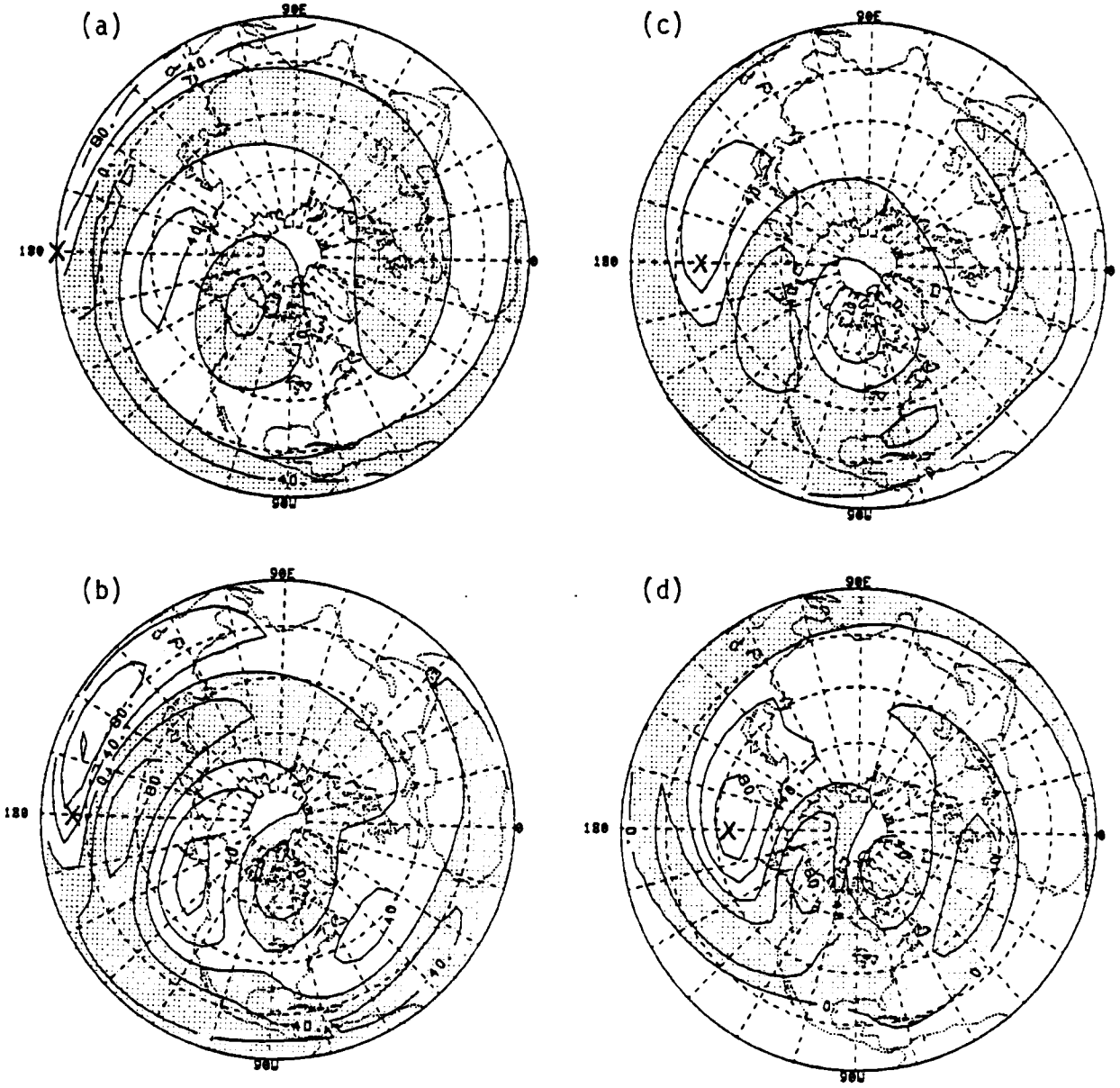

Fig. 4.9. As in Fig. 4.8 except for the 500 mb basic state.

the centers of the stream function response in Fig. 4.9 are located farther to the west than the corresponding centers in Fig. 4.8; this occurs because the zonal mean velocity in this case is smaller than the 250 mb zonal flow and the vorticity source is balanced principally by planetary vorticity advection. As expected from the previous section, the subtropical source excites waves with much smaller amplitudes than those in Fig. 4.8b.

4.3 Characteristics of the barotropic responses in the zonal wavenumber domain

In section 4.1 the characteristics of forced Rossby waves were examined theoretically. However, the plane wave solutions used in the examination there are justified only for the local response because the climatological zonal flows depend highly on latitude. Therefore, to extend the theoretical consideration we reexamine the forced waves for each wavenumber component using the barotropic model, and we also examine the phase of the wave response. For this purpose we prescribe vorticity sources that are sinusoidal in the zonal direction with a sine-square form in latitude.

$$S(\lambda,\phi)=\begin{cases} A\left\{\sin\dfrac{\pi(\theta-\theta_1)}{(\theta_2-\theta_1)}\right\}^2\cos\dfrac{m}{a}\lambda\,, & \theta_1<\theta<\theta_2 \\ 0\,, & \text{otherwise}\end{cases} \tag{4.8}$$

where $A = -1 \times 10^{-10}/\text{sec}^2$, θ_1 and θ_2 are defined as in (4.7). The model solution is derived separately for each zonal wavenumber m from 1 to 6 for the 250 mb basic state.

For the vorticity sources centered at the equator, the responses for each wavenumber are shown in Fig 4.10 in terms of the amplitude and phase. The phase is defined as the longitude of the ridge minus the longitude of the source. In Fig. 4.10 the amplitudes in the winter hemisphere are much larger than in the summer hemisphere, indicating the importance of the zonal flow on the wave response. For ultra-long waves (m = 1, 2, and 3) two amplitude maxima occur in each hemisphere, and the phase differences between the adjacent maxima are about 180°. We may therefore expect the north-south seesaw in the remote responses of the ultra-long wave components for tropical vorticity sources. On the other hand, the responses of the long waves (m = 4, 5, and 6) are localized in the subtropics with relatively small amplitudes. Similar characteristics are also found in the case of vorticity source specified in the middle latitudes for the ultra-long wave components (Fig. 4.11). In this figure, in particular, the amplitudes of the long waves are almost negligible compared with those for the ultra-long wave components.

Since the most significant responses are revealed in the ultra-long wave components, the discussion will be concentrated on these wave responses. The model solutions for zonal wavenumbers m = 1, 2, 3 are shown in Fig. 4.12-4.14, respectively. In each figure, panels (a)-(d) show the responses to the sources centered at 0°N, 15°N, 30°N, and 45°N respectively. The most prominent feature for zonal wavenumber 1 is that no matter where the wavenumber 1 source is located, three amplitude maxima occur in the subtropics, middle latitudes and polar region in the Northern Hemisphere (Fig. 4.12). These adjacent

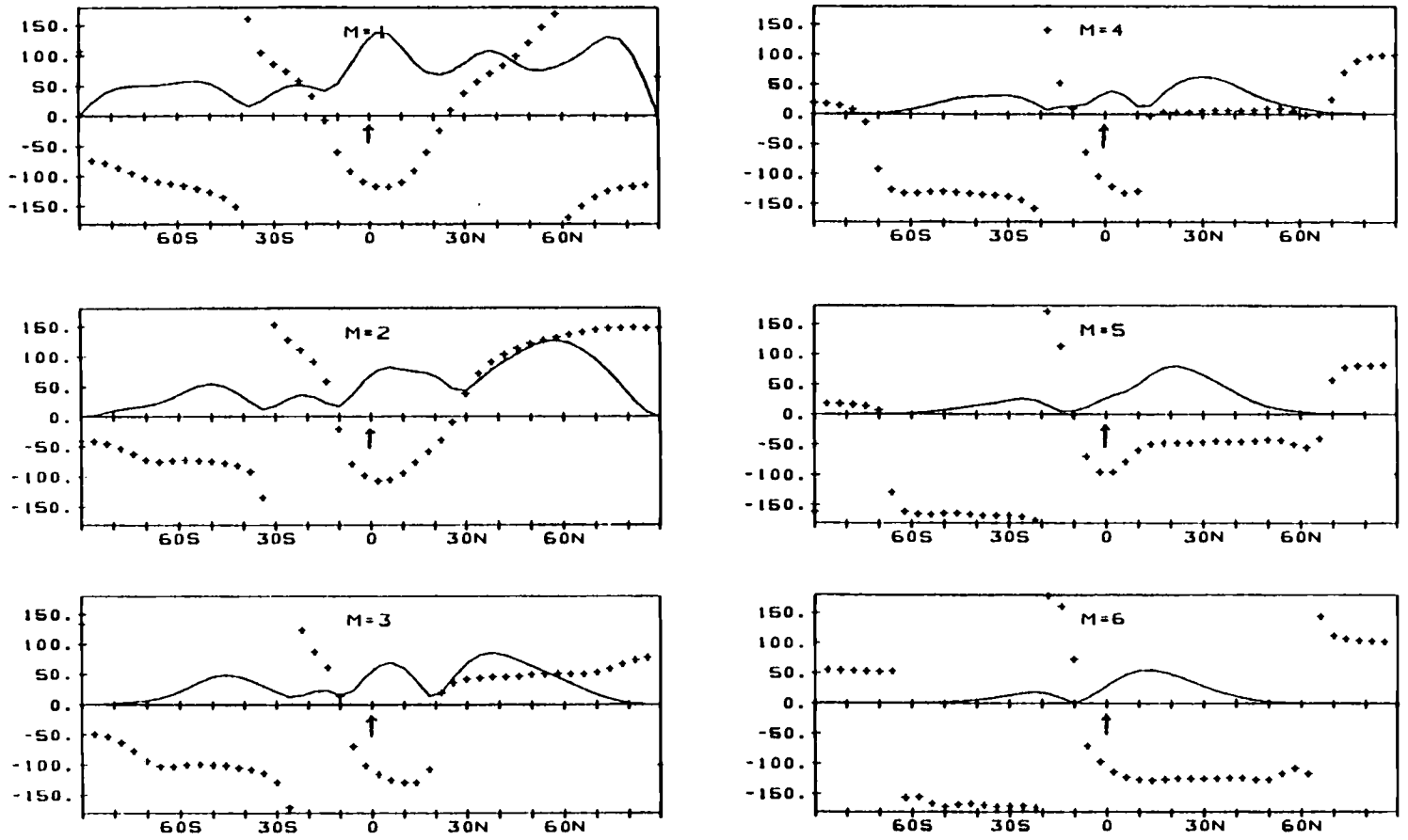

Fig. 4.10. Amplitude and phase of the stream function response for a vorticity source centered at equator with zonal wavenumber M. The 250 mb zonal flow is used for the basic state. Solid line represents the amplitude (unit: 3×10^5 m^2/sec), and the crosses represent the phase (degree). ↑ shows the location of the center of the source.

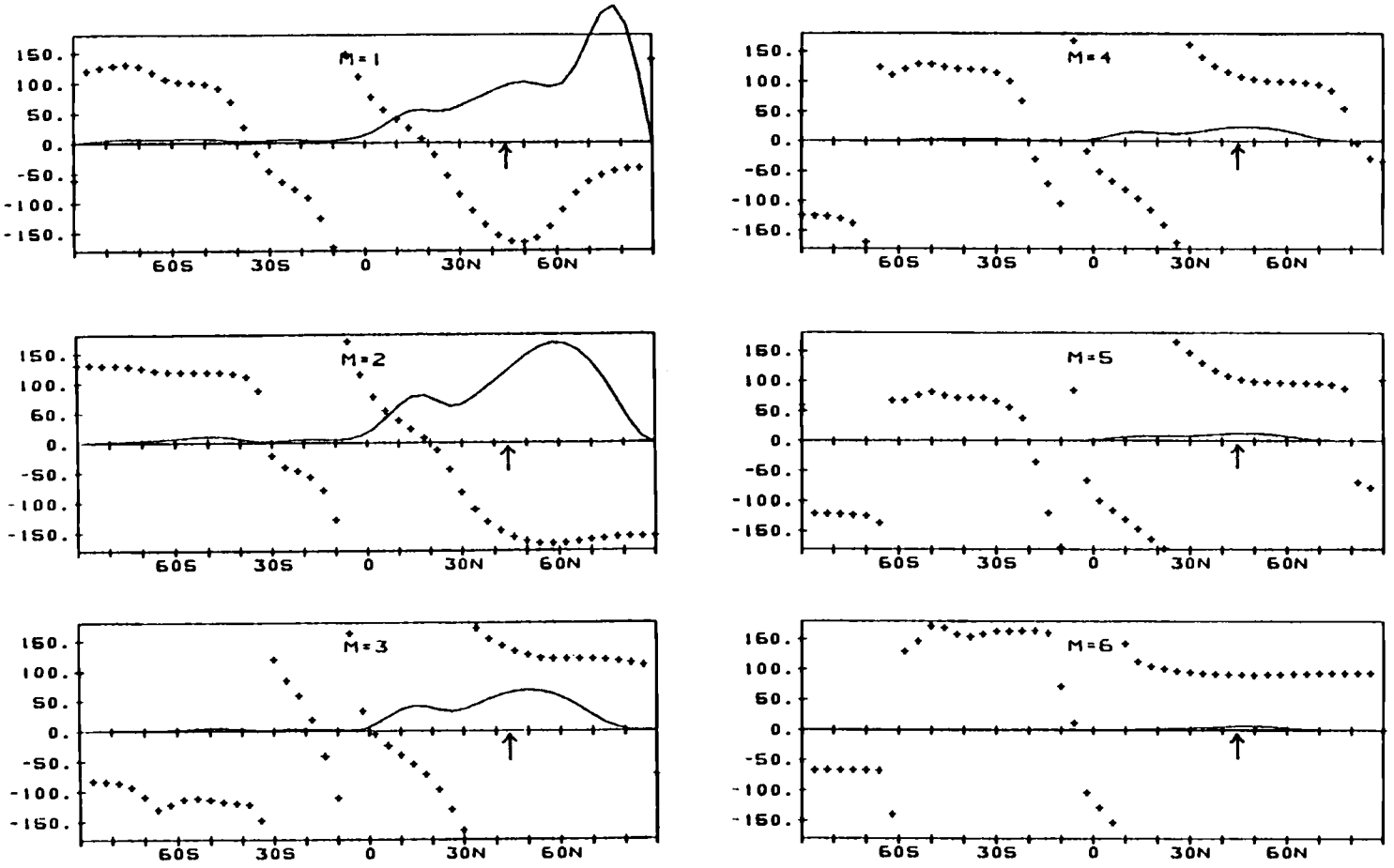

Fig. 4.11. As in Fig. 4.10 except for the response to the vorticity source centered at 45°N.

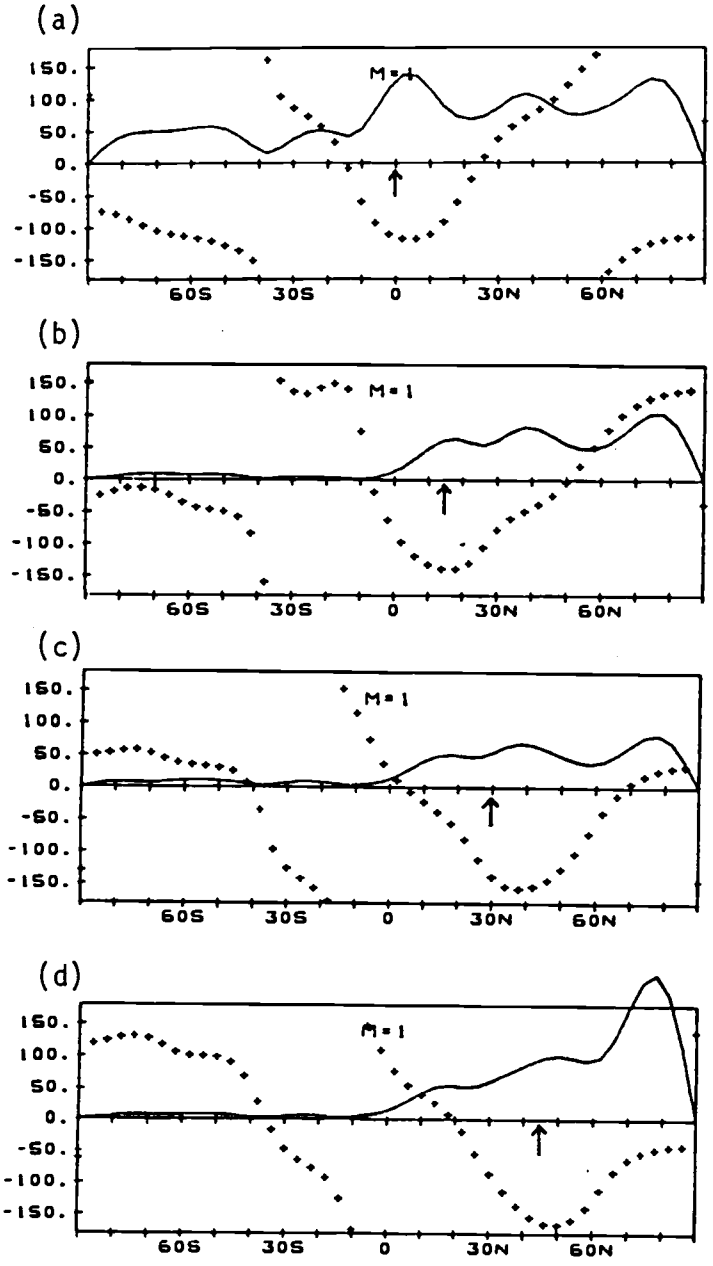

Fig. 4.12. Amplitude and phase of the stream function response to a vorticity source of zonal wavenumber 1 centered at (a) 0°N, (b) 15°N, (c) 30°N, and (d) 45°N. The lines and units are as in Fig. 4.10.

maxima have an eastward tilt with increasing latitude. The largest remote responses occur in the polar region near 75°N which is consistent with the theoretical result given in section 4.1. In the case of wavenumber 2 (Fig. 4.13) two maxima occur at the high latitudes near 60°N and in the subtropics for each vorticity source. These maxima tilt to the west with increasing latitude for the sources centered at 0° and 15°N, but tilt to the east for the sources centered at 30°N and 45°N. The wavenumber 3 responses (Fig. 4.14) also show two maxima generally at the middle latitudes and the subtropics which are out of phase except for the sources in the subtropics.

The above characteristic behavior of the model has also been examined with the 500 mb basic state (not shown). The overall characteristics are similar to those for the 250 mb basic state. The major differences are: the remote responses of ultra-long waves are relatively small, and the north-south seesaw of the wavenumber 2 occurs between the high latitudes and the middle latitudes near 30°N instead of the subtropics.

The north-south seesaws occurring in the present barotropic model are quite consistent with observations. As shown in section 2.1, the seesaw in the wavenumber 1 component is observed between the polar and middle latitudes with a center near 55°N (Fig. 2.3), and the seesaw in the wavenumber 2 component (Fig. 2.2a) appears to occur between the high and middle latitudes. The remote responses dominated by ultra-long waves are also consistent with the observed teleconnection patterns.

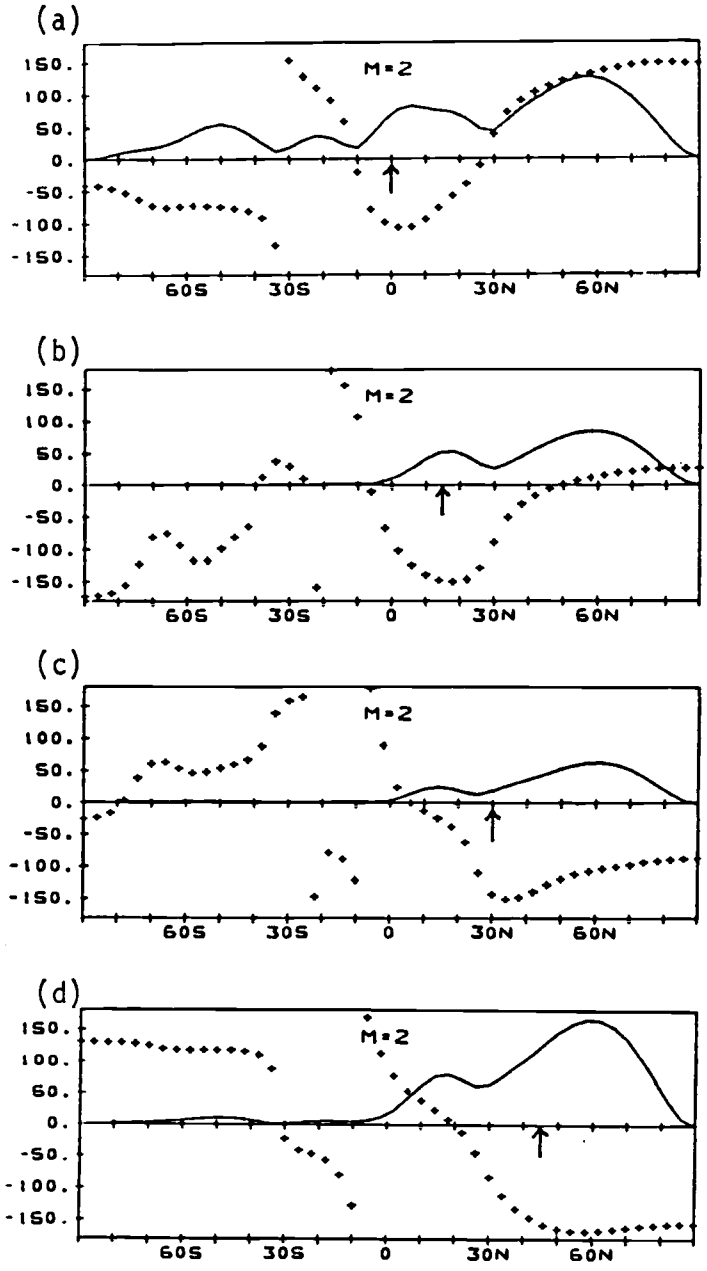

Fig. 4.13. As in Fig. 4.12 except for zonal wavenumber 2.

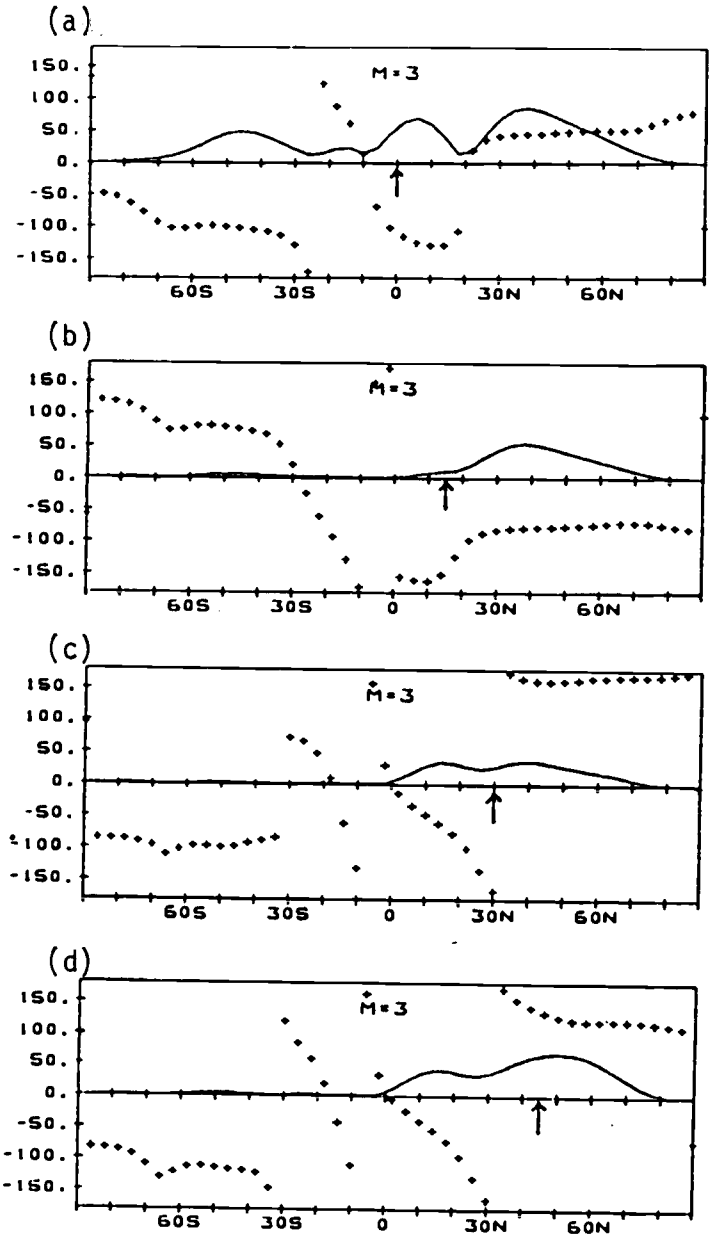

Fig. 4.14. As in Fig. 4.12 except for zonal wavenumber 3.

5. ATMOSPHERIC RESPONSES TO PRESCRIBED HEATING

The baroclinic responses to isolated heat sources have recently been studied by several investigators with linear models (Gill, 1980; HK; Simmons, 1982). Since these studies provide a guide to understanding the atmospheric responses to prescribed SST anomalies, we reproduce the previous works in this chapter using the baroclinic model described in Chapter 3. To better understand the baroclinic responses to the heating, the model results are interpreted in terms of the quasi-geostropic wave dynamics given in section 2.3. In order to delineate the effects of baroclinicity the characteristics of forced planetary waves simulated using the baroclinic model are also examined and compared with the barotropic model results.

For all baroclinic experiments the climatological January 250 mb and 750 mb zonal means are used as the upper and lower layer basic states, respectively.

5.1 Baroclinic responses to isolated heat sources

The baroclinic responses to isolated thermal forcings prescribed at the various latitudes are examined in this section. The forcings are specified using the elliptic formula expressed by (4.7), where the location of the source is determined by θ_0. The maximum heating rate A used in this section is 4°/day. In Holton (1979) a 5°/day heating rate corresponds to precipitation rate of about 10 mm/day, a value appropriate for the wettest regions in the tropics. Therefore, the present

heating rate is a reasonable choice for a tropical heat source, while it may be somewhat large for a typical heating in the middle latitudes.

5.1.1 Subtropical heat source

We now discuss the model responses to the thermal source in the subtropics ($\theta_0 = 15°N$). Since a subtropical heating anomaly generally has a deep structure in the vertical, the same heating has been prescribed at both layers in the model.

To examine the time evolution of the responses, the 250 mb height responses are displayed every 5 days in Figs. 5.1a-d. As in the barotropic case, these figures clearly show the waves propagating along a wavetrain which splits into two near 60°N and 90° downstream from the source. An interesting feature in Fig. 5.1 is the existence of baroclinic eddies apparently due to the baroclinic instability of the climatological basic state. Such an instability would be eliminated by using large dissipations (e-folding time of a few days) characteristic of these synoptic systems. However, the use of such a large dissipation here would also give unrealistically weak responses for the planetary waves. Therefore, we eliminate the synoptic eddies by taking a 15-day time mean from day 5 to day 20. This is consistent with the purpose of the present study, namely, to examine the quasi steady-state planetary-scale responses.

The height responses at 250 mb and 750 mb are shown in Figs. 5.2a and b respectively. Apparently, the baroclinic eddies have been removed. The equivalent barotropic structure of the remote response is also evident in these figures. In particular, the pattern of the

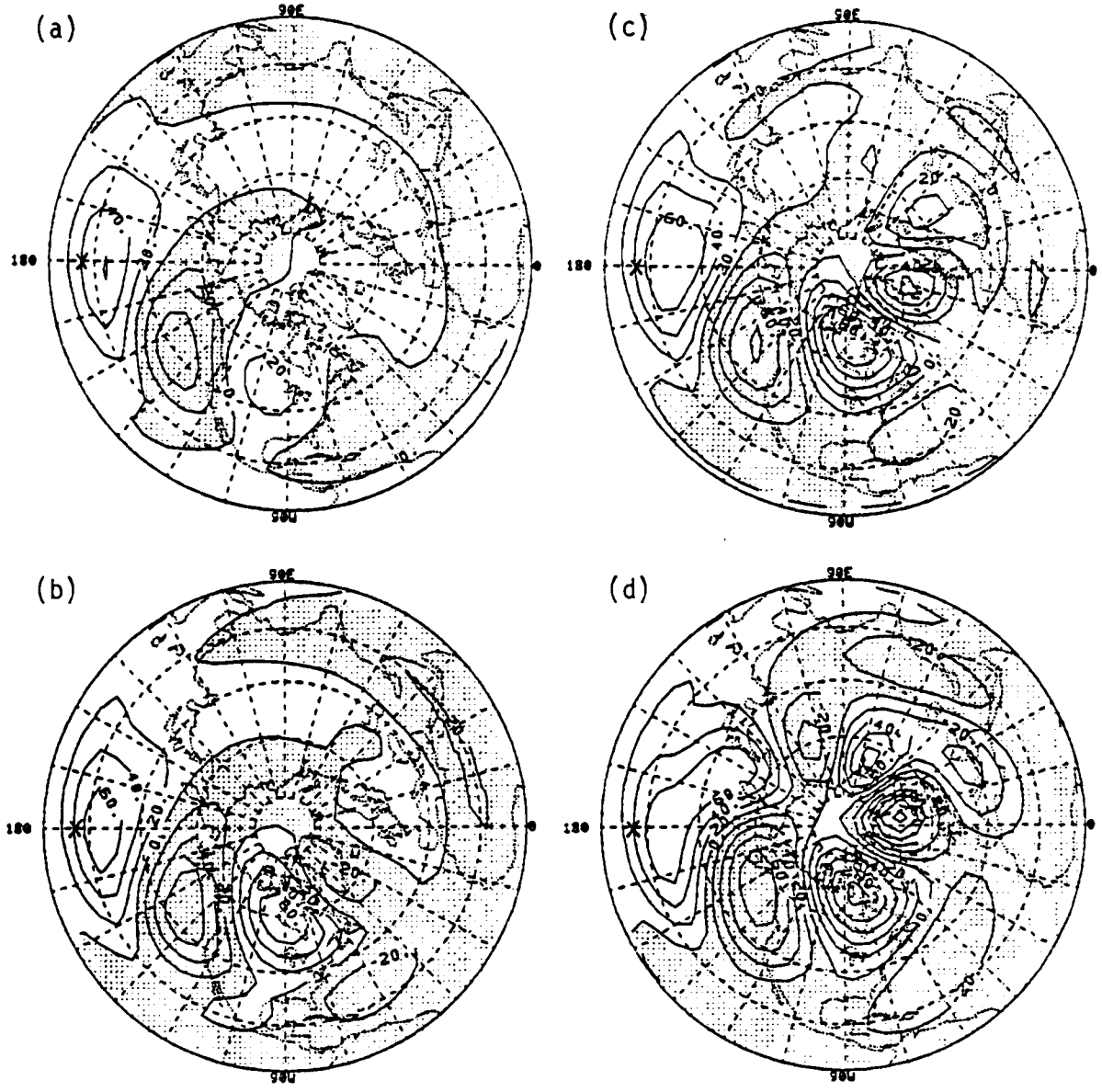

Fig. 5.1. 250 mb height response to the heat source centered at 15°N and 180°E. Shown are the responses at (a) day 5, (b) day 10, (c) day 15, (d) day 20. Contour intervals are 20 meters. x shows the center of the source.

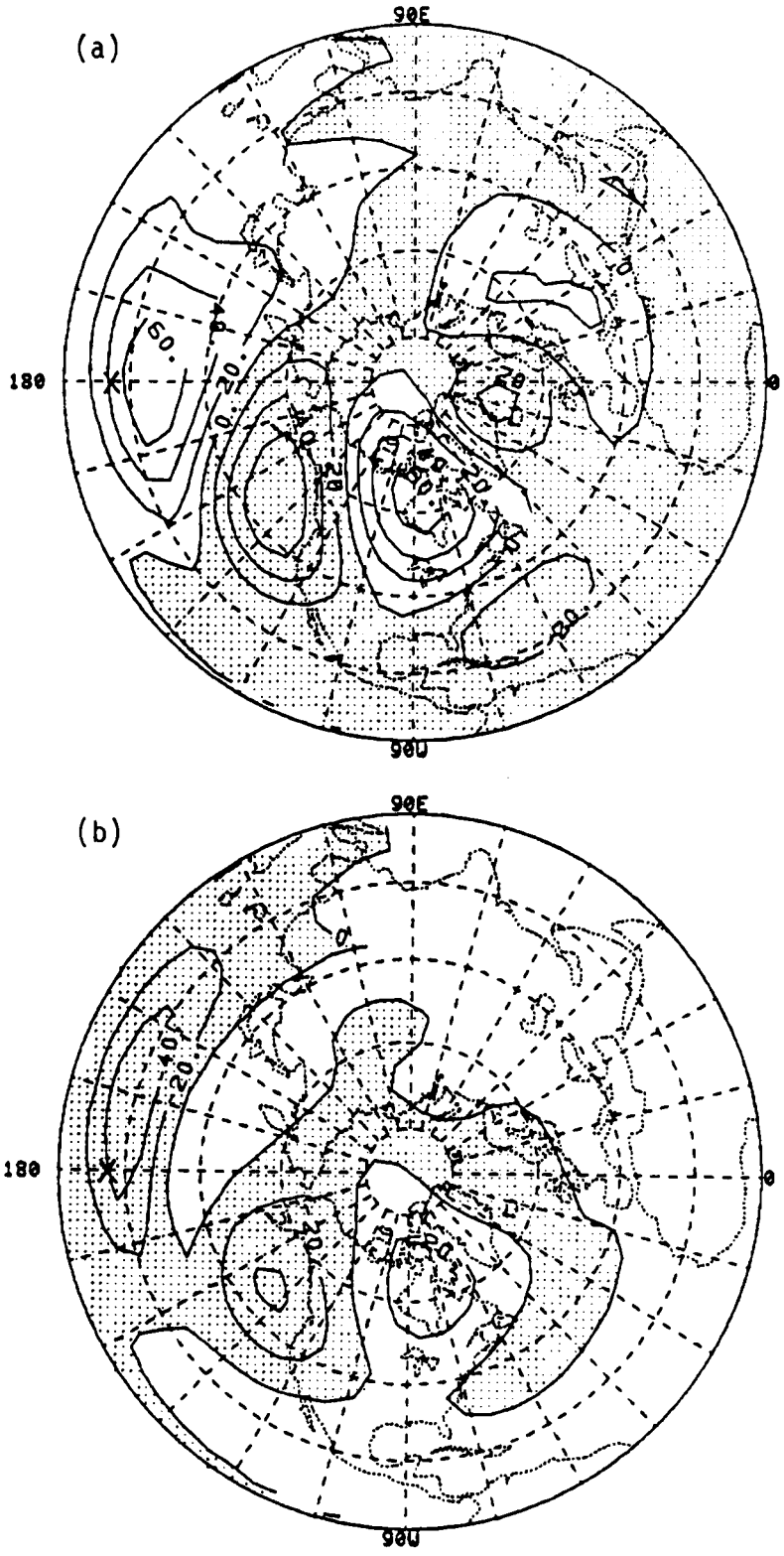

Fig. 5.2. The 15-day mean height response to the subtropical heat source. (a) 250 mb, (b) 750mb. Unit: meter. x shows the center of the source.

250 mb height response is very similar to the barotropic response shown in Fig. 4.8b, although different kinds of forcing are used in the models. Over the source latitudes, on the other hand, the responses are dominated by a baroclinic mode; a negative response at 750 mb is located over and west of the source, while a positive response is located aloft over the source.

The vertical velocity dp/dt at 500 mb is shown in Fig. 5.3. Since the present model has only two layers, the vertical velocity is calculated only at the 500 mb level. This figure shows that a strong ascending motion (in stippled region) is maintained over the subtropical source, indicating that the main thermal balance is between the source and adiabatic cooling due to the upward motion. For the vorticity balance, in the lower layer the vortex stretching should induce a northward motion (shown in Fig. 5.2b) which in turn advects warm air from the south to the source. To balance this warming with the zonal advection, the lower-layer temperature perturbation should have a negative zonal gradient $(\partial T'/\partial \lambda < 0)$ over the source since $\bar{u}$ is negative in this region. As shown in Fig. 5.4 the 750 mb temperature response has a maximum located to the west of the source, and this is consistent with such a thermal balance. Clearly, the model's local and remote responses are quite consistent with the theoretical considerations given in section 2.3.

5.1.2 Middle latitude heat source

We now consider the responses to the heat source located in the middle latitudes ($\theta_0 = 45°N$). Since large-scale diabatic heating is

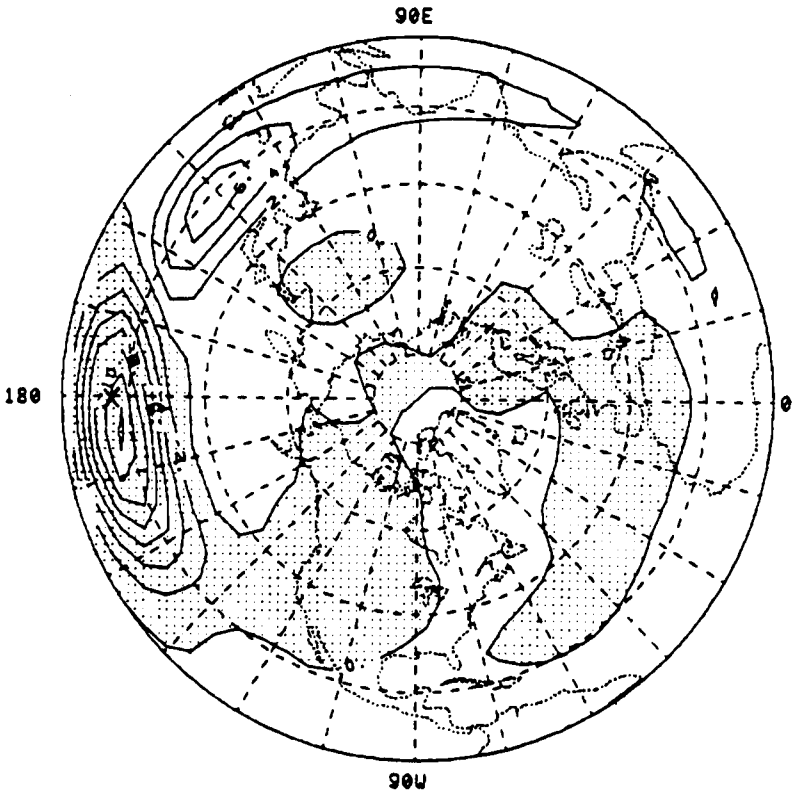

Fig. 5.3. Vertical velocity (dp/dt) field at $\sigma = 0.5$ for the subtropical heat source. Contour interval is 2×10^{-4} mb/sec.

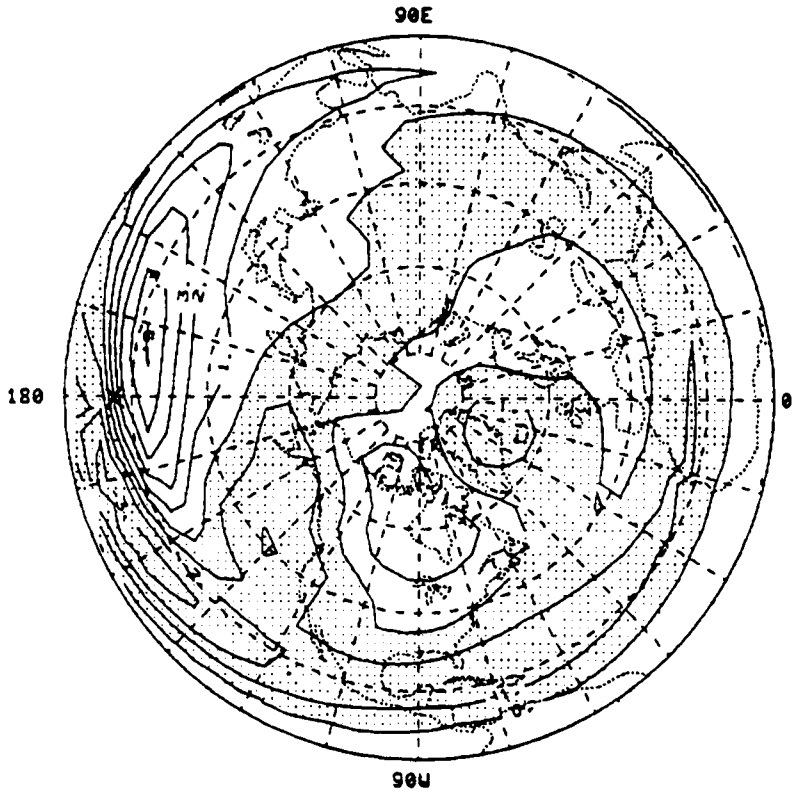

Fig. 5.4. 750 mb temperature response to the subtropical heat source. Contour interval is 1°K.

generally confined below the 500 mb level in the middle latitudes, the source is prescribed only at the lower layer in the model.

Figures 5.5a and b show the 250 mb and 750 mb height responses, respectively. The local responses are also consistent with the theoretical inferences, showing negative 750 mb and positive 250 mb responses to the east of the source. As expected from section 5.1.1, the remote responses are typically barotropic. It is interesting to note that although HK used a different horizontal distribution for the source (circular distribution rather than an ellipse), the pattern of their 300 mb height field is remarkably similar to the present 250 mb response. This strongly suggests that the remote responses are due to the normal modes of Rossby waves on the sphere.

The corresponding vertical motion is very small and even downward over the heat source (Fig. 5.6). As discussed in section 2.3, this small vertical velocity is due to the fact that the middle latitude source is mainly balanced by the horizontal advection rather than adiabatic cooling. In this experiment $H \sim H_u$. Therefore, the zonal advection as well as the meridional advection is important to balance the source as shown by the negative temperature perturbation to the west of the source in the lower layer (Fig. 5.7).

5.1.3 Tropical heat source

It is conceivable from the previous studies (e.g., Horel and Wallace, 1981) that an anomalously warm ocean leads to extra convective heating in the tropics. Thus, before attempting to study the effects of tropical SST anomalies on the atmospheric circulation, it is worth

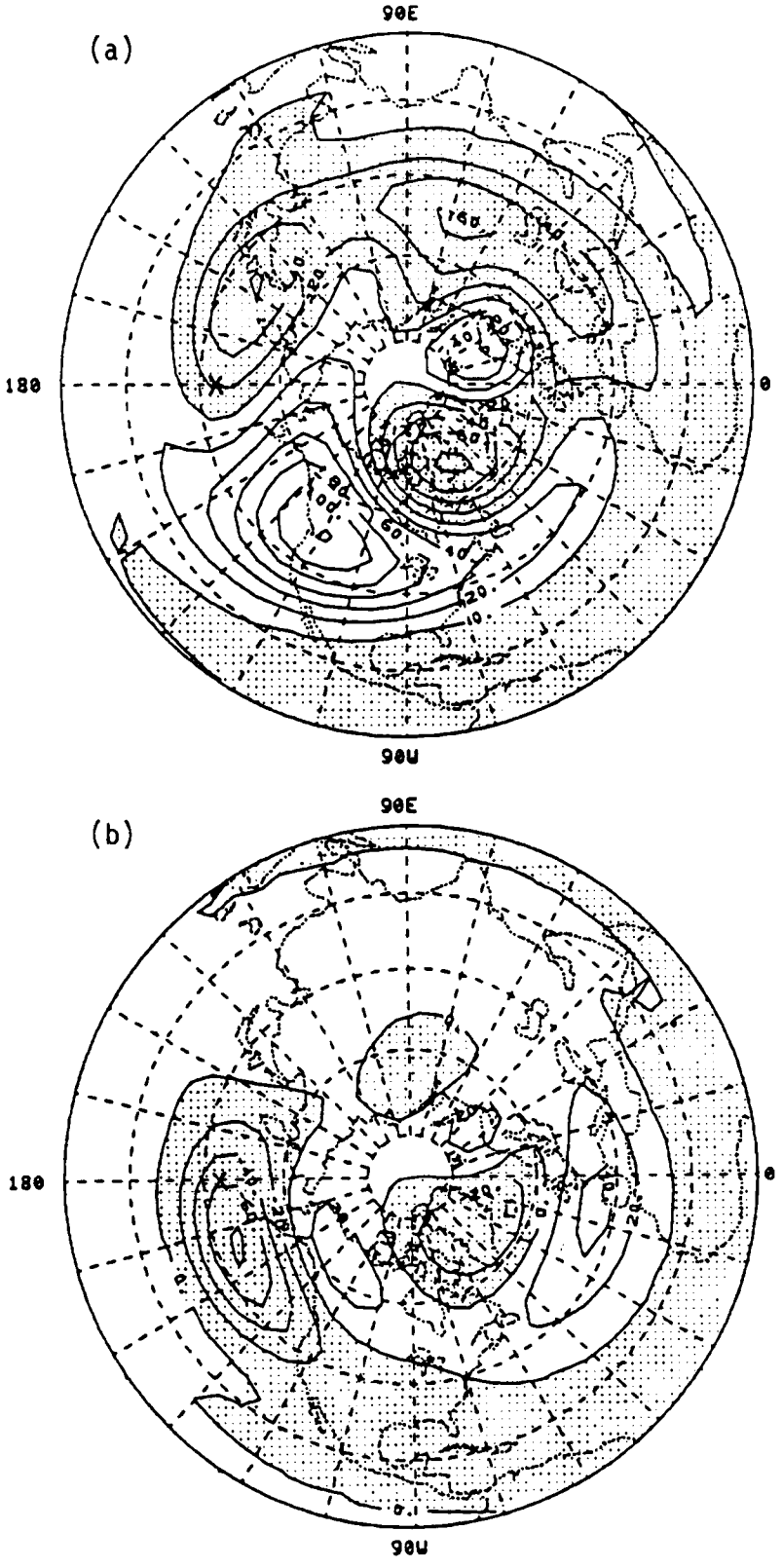

Fig. 5.5. As in Fig. 5.2 except for a shallow heat source in the middle latitudes (Θ_0 = 45°N).

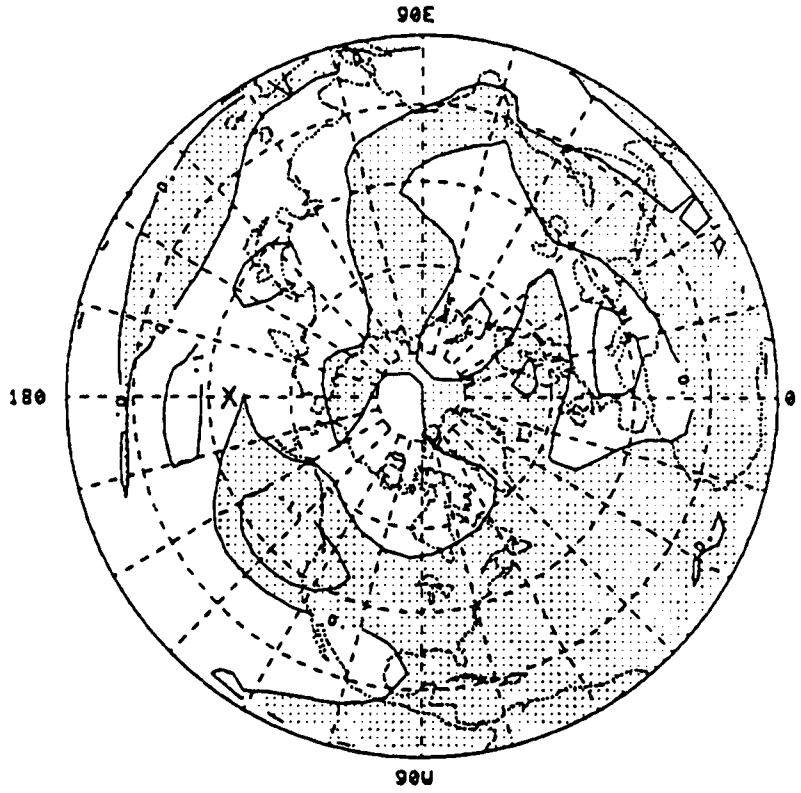

Fig. 5.6. Vertical velocity (dp/dt) field at $\sigma = 0.5$ for the middle latitude heat source. Contour interval is 10^{-4} mb/sec.

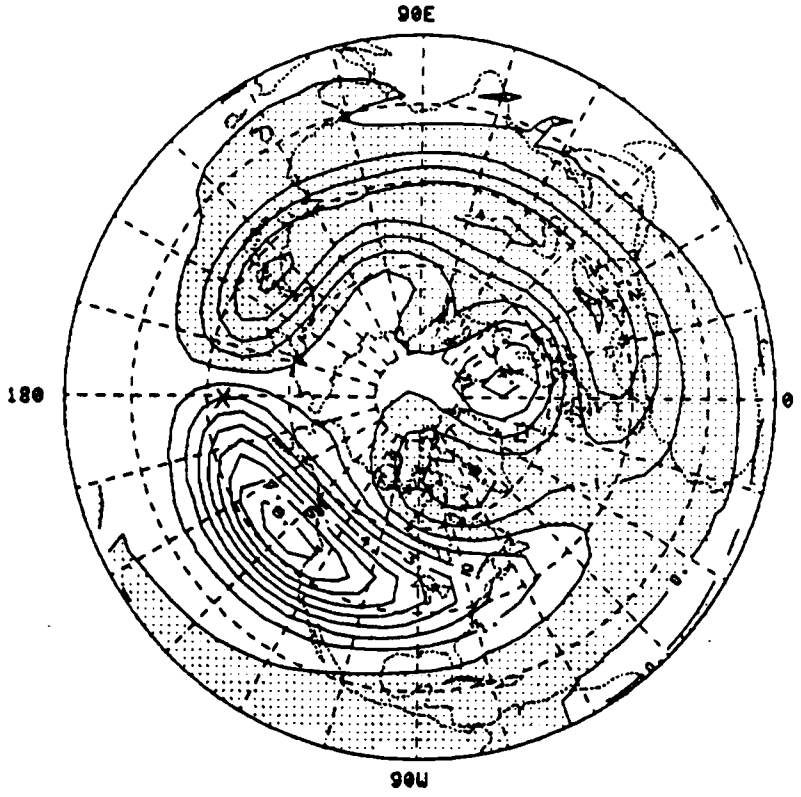

Fig. 5.7. 750 mb temperature response to the middle latitude heat source. Contour interval is 1°K.

while to examine the model responses to tropical atmospheric heating. Here we use the tropical heat source (θ_0 = 0) shown in Fig. 5.8 whose pattern is made to be similar to the observed one illustrated in Fig. 2.4. As in the subtropical case the heat source is equally distributed at both layers of the model.

The 250 mb and 750 mb height responses are shown in Figs. 5.9a and b respectively. Although the 250 mb response has phase discrepancy about 30° relative to the observed shown in Fig. 2.4, the general patterns of both cases are similar to each other. It is also seen in Fig. 5.9 that there exists a substantial difference in the remote responses between two hemispheres, indicating the significant influence of the basic state on the wave propagation.

We now discuss the responses in terms of the motion fields. As theoretically argued in section 2.3, strong upward motion is simulated over the source region (Fig. 5.10). Interestingly, the intensity of the upward motion is approximately proportional to the prescribed heating. For the zonal velocity, as shown in Fig. 5.11, the strong responses are mainly simulated in the tropics. In the lower layer westerly inflow occurs to the west of the source, and easterly inflow occurs to the east with a longer longitudinal extent. A reversed circulation is found aloft. Gill (1980) explained that the greater longitudinal extent to the east is due to the fact that Kelvin waves propagate eastward faster than planetary waves propagate westward. The meridional velocity fields at both layers are shown in Fig. 5.12. The upper-layer field (Fig. 5.12a), in particular, clearly shows the wave propagation along a great circle path. The reason for such a pattern

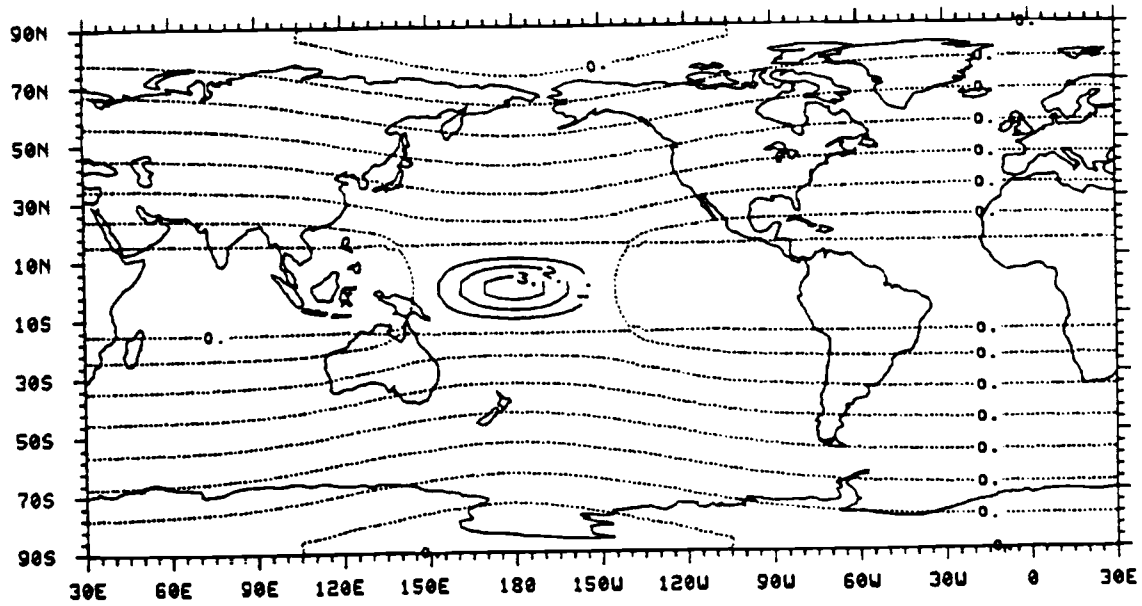

Fig. 5.8. Tropical heating field represented by 6 zonal wavenumber components and 15 associated Legendre polynomials. Unit: °K/day.

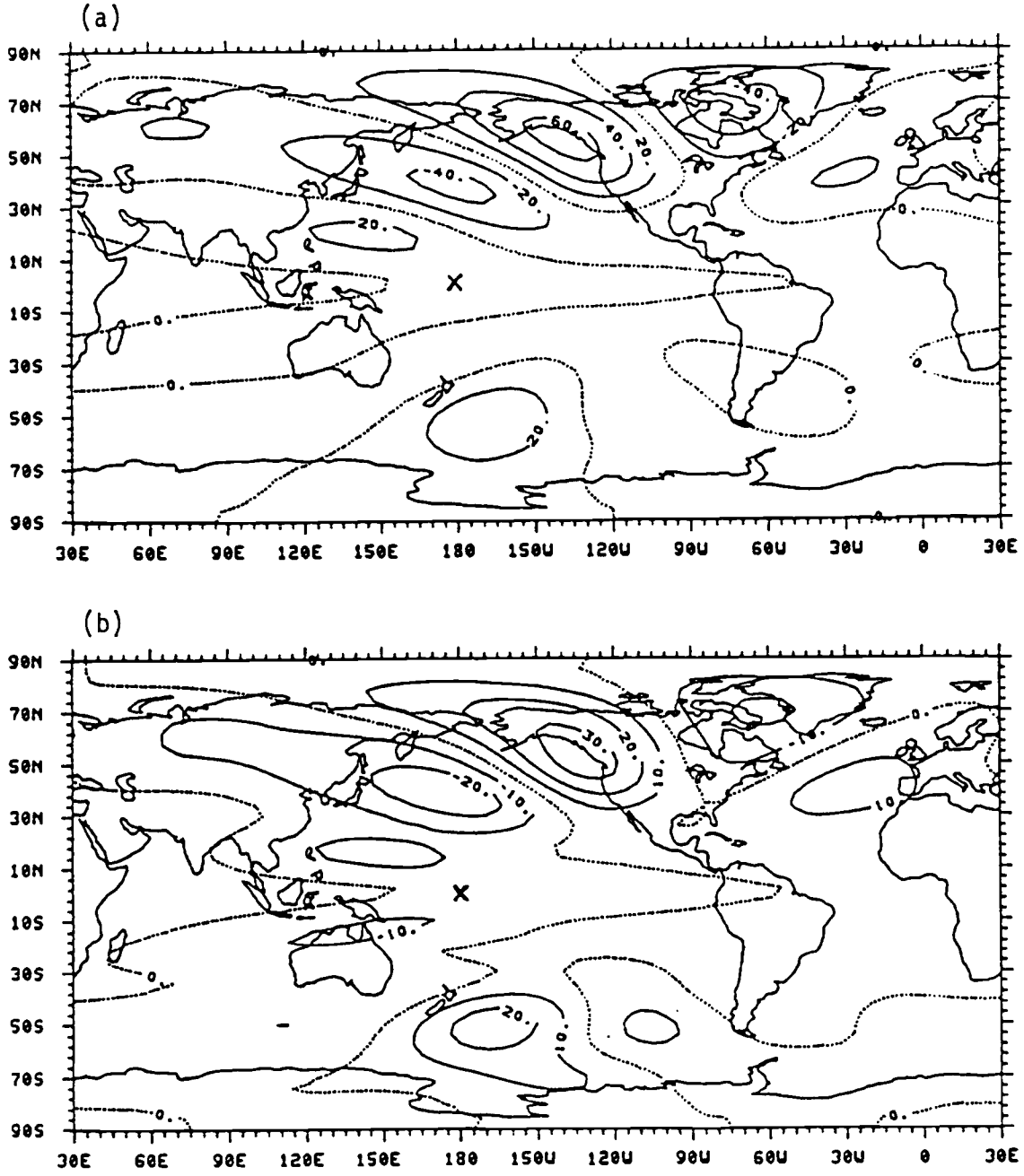

Fig. 5.9. The response to the tropcal heating. Shown are the height field at (a) 250 mb and (b) 750 mb. Contour intervals are 20 meters. x shows the center of the source.

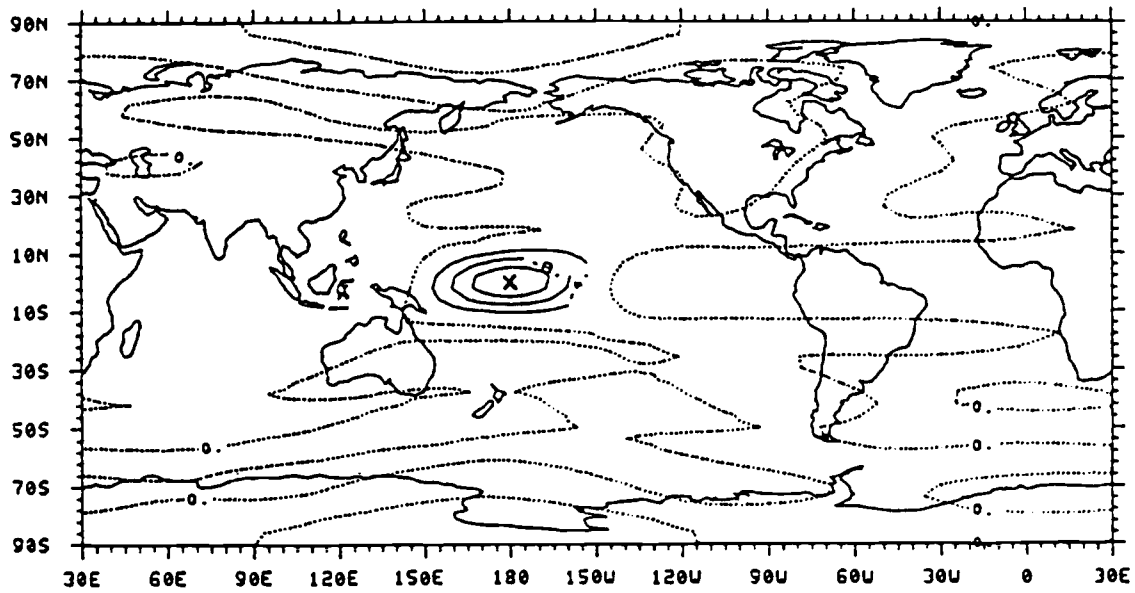

Fig. 5.10. Vertical velocity (dp/dt) field at $\sigma = 0.5$ for the tropical heating. Contour interval is 2×10^{-4} mb/sec.

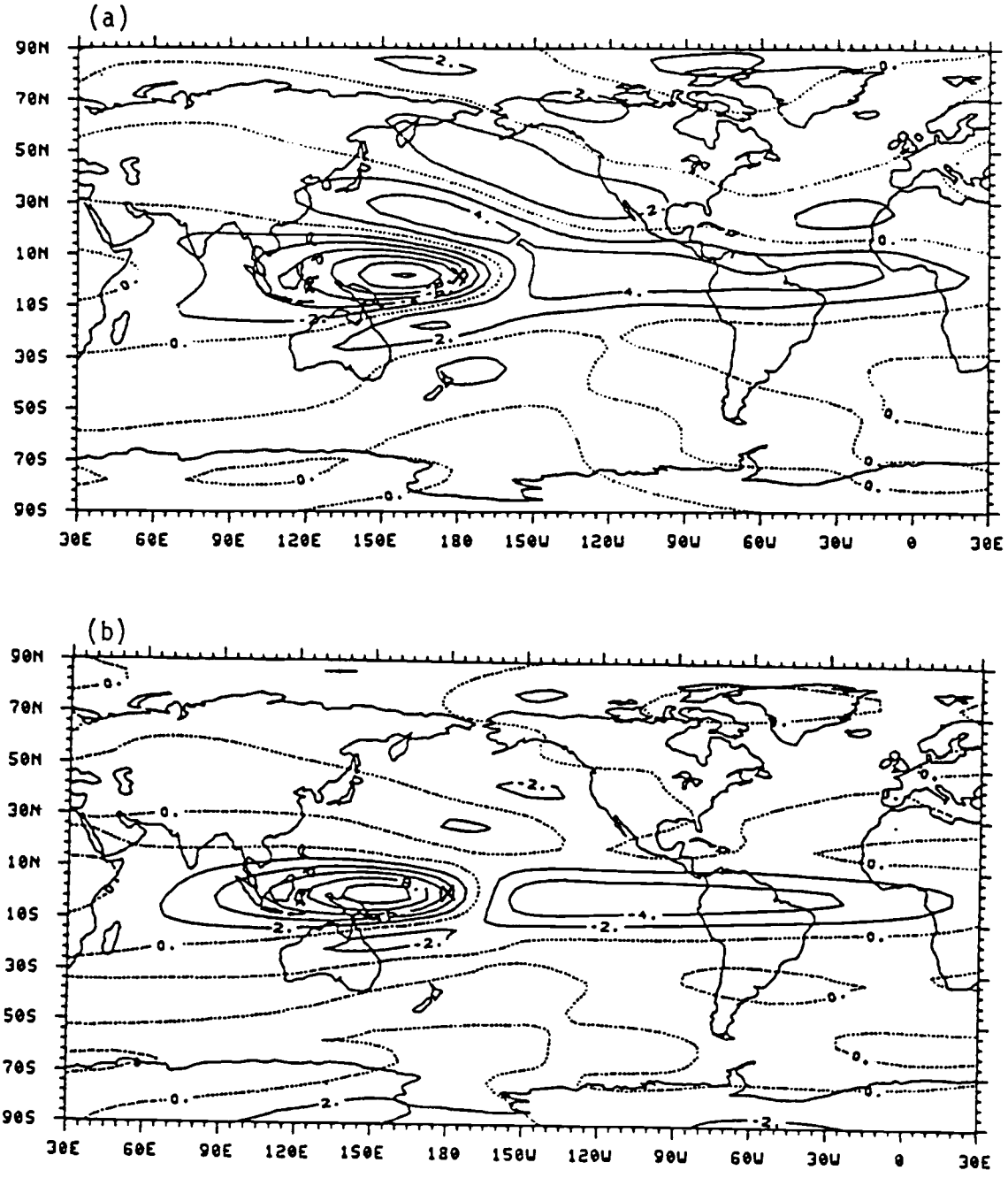

Fig. 5.11. Zonal wind responses to the tropical heating at (a) the upper layer and (b) the lower layer. Contour intervals are 2 m/sec. x shows the center of the source.

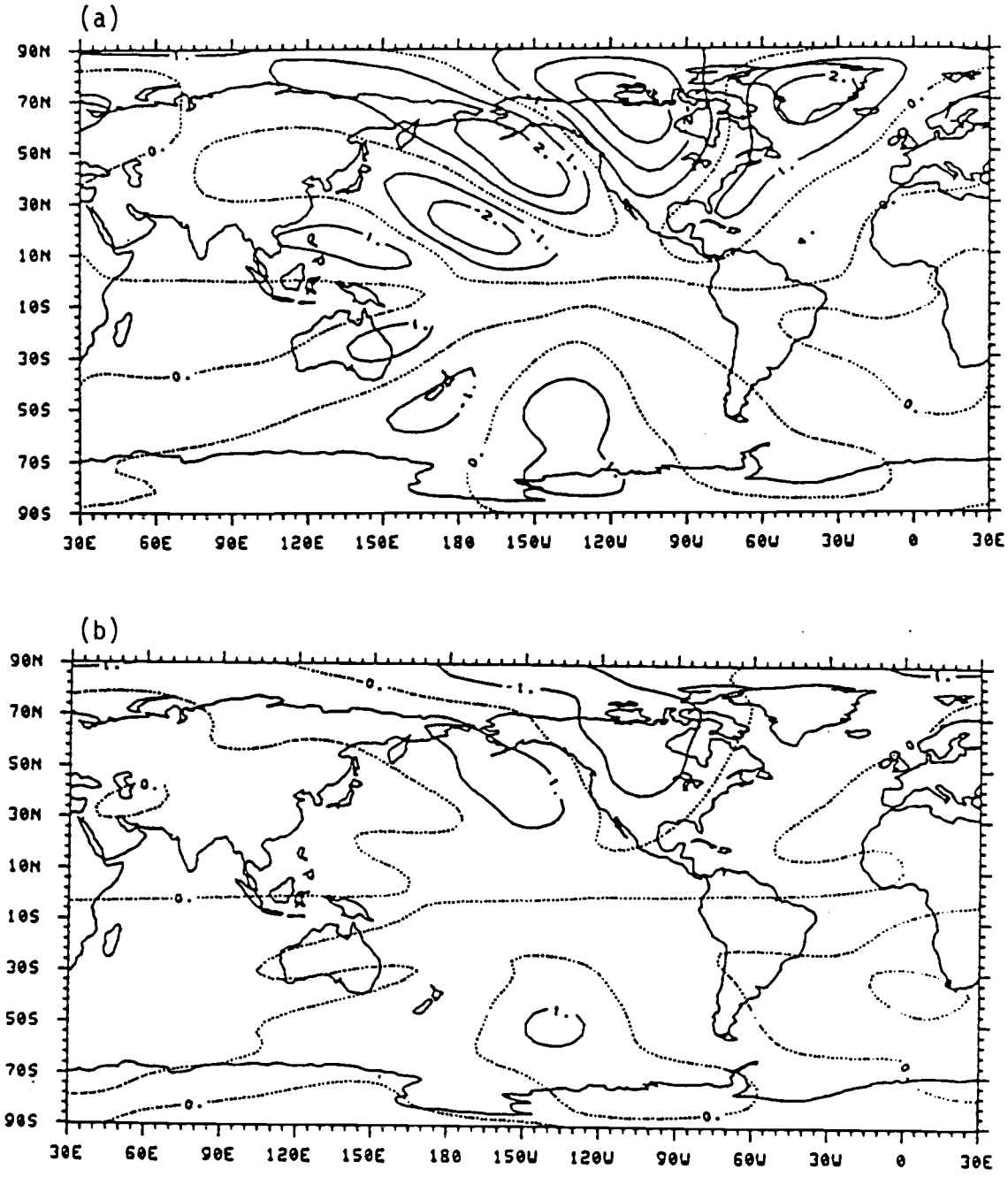

Fig. 5.12. Meridional wind fields for the tropical heating at (a) the upper layer and (b) the lower layer. Contour intervals are 1 m/sec.

is that the planetary wave mode is mainly represented by meridional motion field because the vorticity balance in a steady-state is expressed as $\beta v' + \bar{u}\nabla^2 v' = 0$. The velocity potential fields are shown in Fig. 5.13. These fields show simple global patterns. The lower-layer convergence is seen over the source with the maximum at the source and the divergence outside the source longitudes (Fig. 5.13b), while exactly the reversed circulation is seen aloft (Fig. 5.13a). In comparing the present motion fields with those in Fig. 2.6, one finds that the present model remarkably reproduces the simple model results of Gill (1980).

5.2 Characteristics of the baroclinically forced waves in the zonal wavenumber domain

In the previous chapter ultra-long wave north-south seesaws were found for the barotropic atmosphere. Here we investigate whether this finding still holds in the baroclinic case. We again prescribe wavenumber-dependent heat sources at both layers in the baroclinic model. The source function is given by (4.8) with maximum heating rate $A = 2°/day$.

The model calculations have been done for each wavenumber from $m = 1$ to 6. The responses to the sources with wavenumbers $m = 4, 5, 6$ are found to be localized near the sources and to have much smaller amplitudes than those for ultra-long wave components. We therefore concentrate on the responses of ultra-long waves. The latitudinal distributions of the amplitude and phase for the 15-day mean heights are shown in Figs. 5.14-16. For the wavenumber 1 component the 250 mb

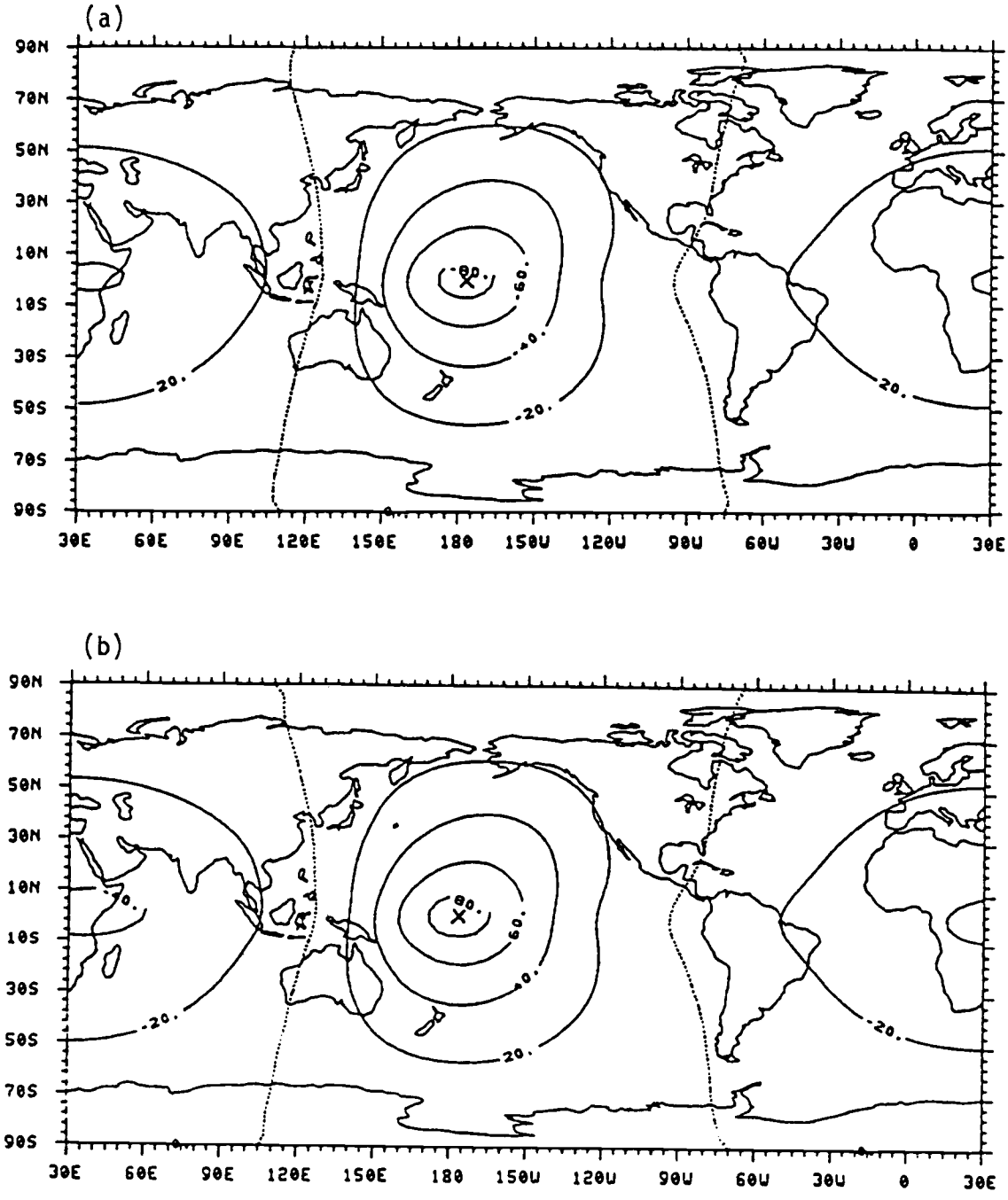

Fig. 5.13. Velocity potential fields at (a) the upper layer and (b) the lower layer induced by the tropical heating. Unit: 10^5 m^2/sec.

responses to the source centered at 0°N, 15°N, 30°N, and 45°N are shown in Figs. 5.14a-d, respectively, and the 750 mb responses for the same sources are shown Figs. 5.14e-h. The 250 mb responses (Fig. 5.14a-d) have maximum amplitude in the middle latitudes and there is an eastward tilt with increasing latitude from middle to polar latitudes with a phase difference of about 180°. We therefore expect a north-south seesaw between the polar and middle latitudes in the 250 mb response to a wavenumber one source located at any northern latitude. The seesaw pattern is also identified at 750 mb for the sources specified at 0°N and 15°N, but is not evident for the middle latitude sources, mainly due to the baroclinicity near the source. In the case of zonal wavenumber 2 the seesaw between the high and middle latitudes is also generally identified at both 250 mb and 750 mb for all heat sources except that at 45°N and 250 mb (Fig. 5.15). For the wavenumber 3 sources the seesaw pattern is not found (Fig. 5.16). The responses in this case display only a single maximum in the high latitudes regardless of the geographical location of the sources.

The 250 mb remote responses for the present case are much weaker than for the barotropic case shown in Fig. 4.12. The weak baroclinic responses are due to the influence of the lower-layer basic state on the upper-layer wave propagation. In fact, the characteristic patterns of the present 250 mb responses are similar to those of the barotropic response for the 500 mb basic state rather than for the 250 mb zonal flow.

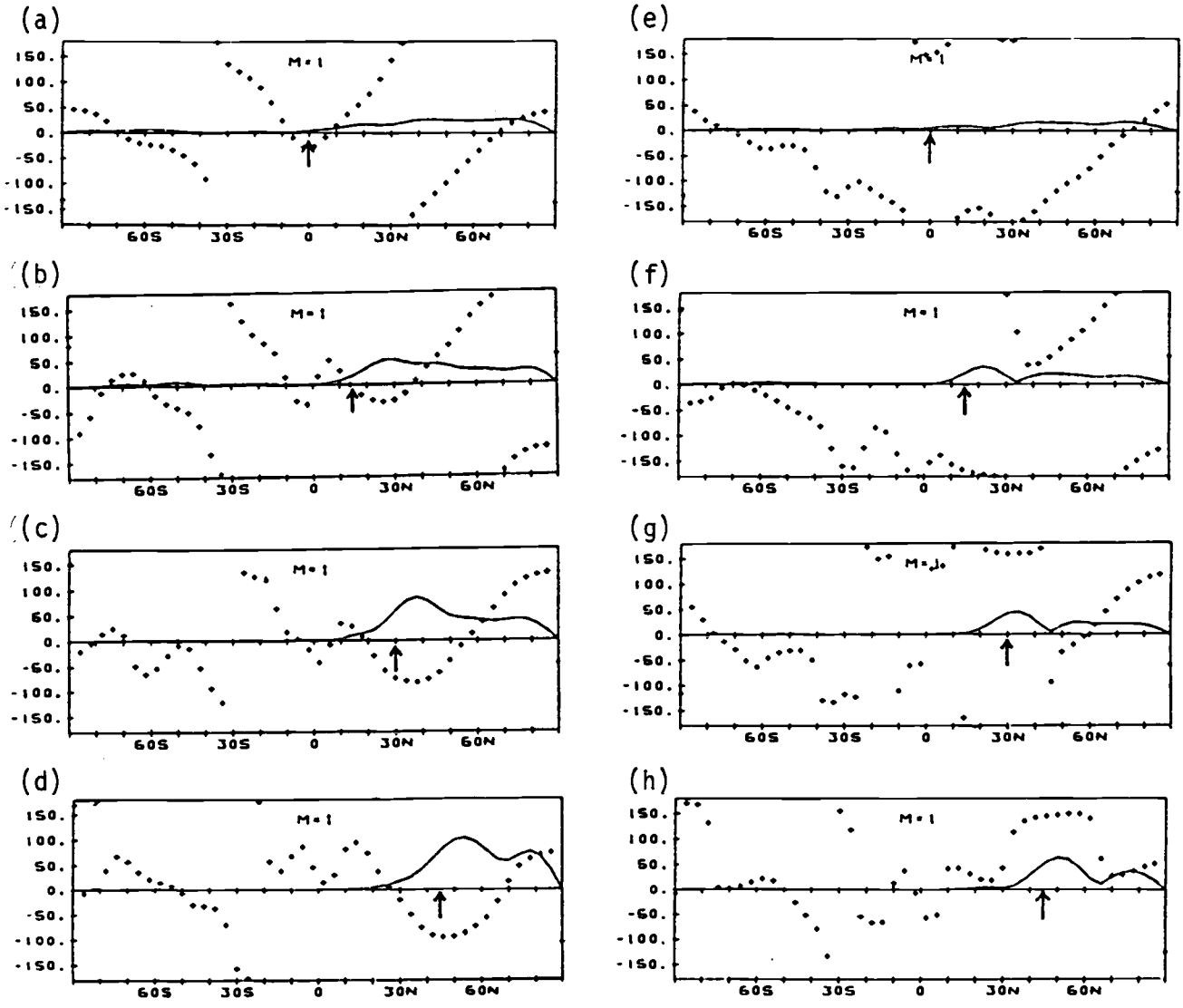

Fig. 5.14. Amplitude and phase of the height response to a heat source of zonal wavenumber 1. The 250 mb responses to the source centered at 0°N, 15°N, 30°N, and 45°N are shown in (a)-(d) respectively, and the 750 mb responses to the same sources are shown in (e)-(h). Units for amplitude and phase are meter and degree respectively.

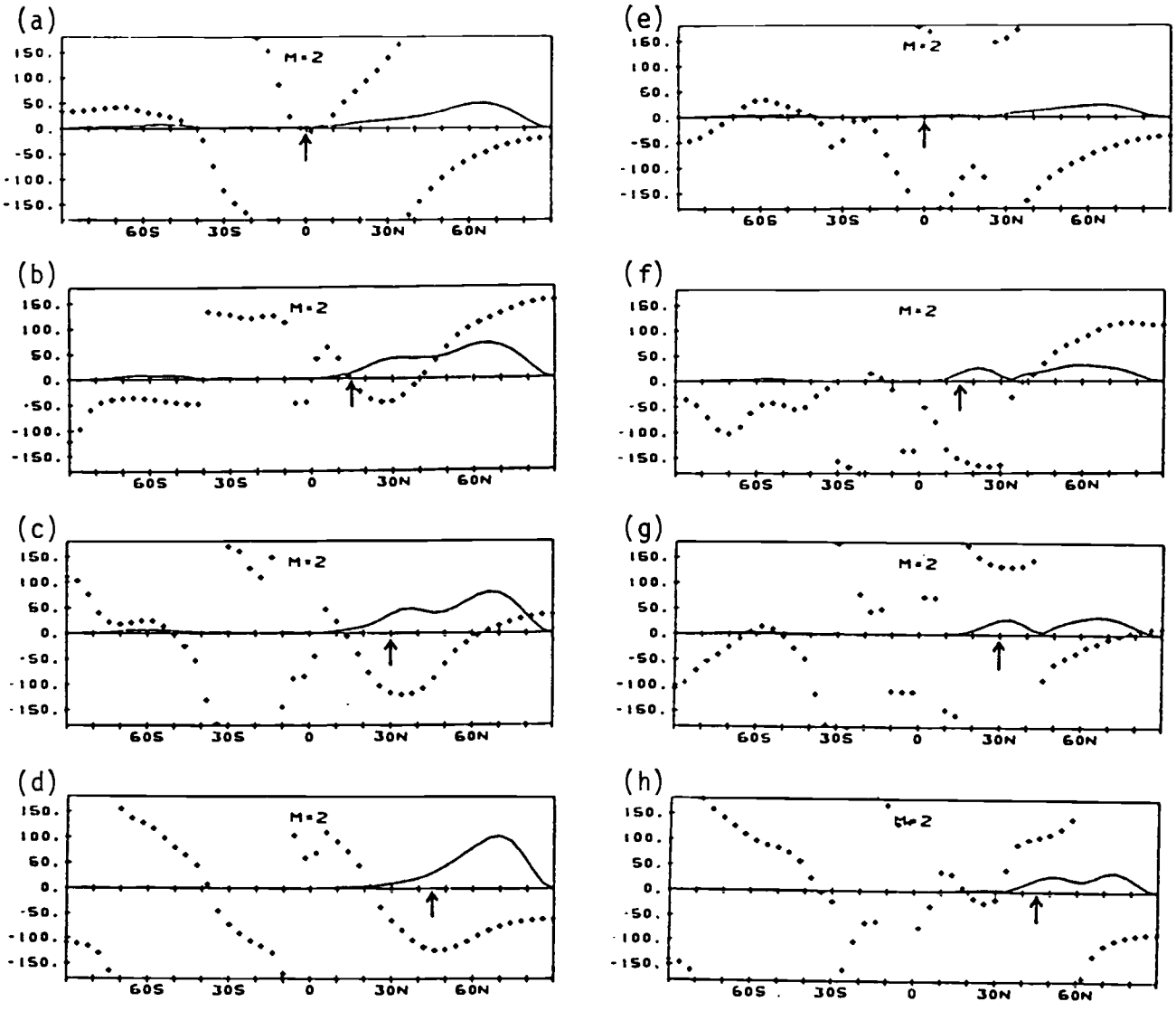

Fig. 5.15. As in Fig. 5.14 except for zonal wavenumber 2.

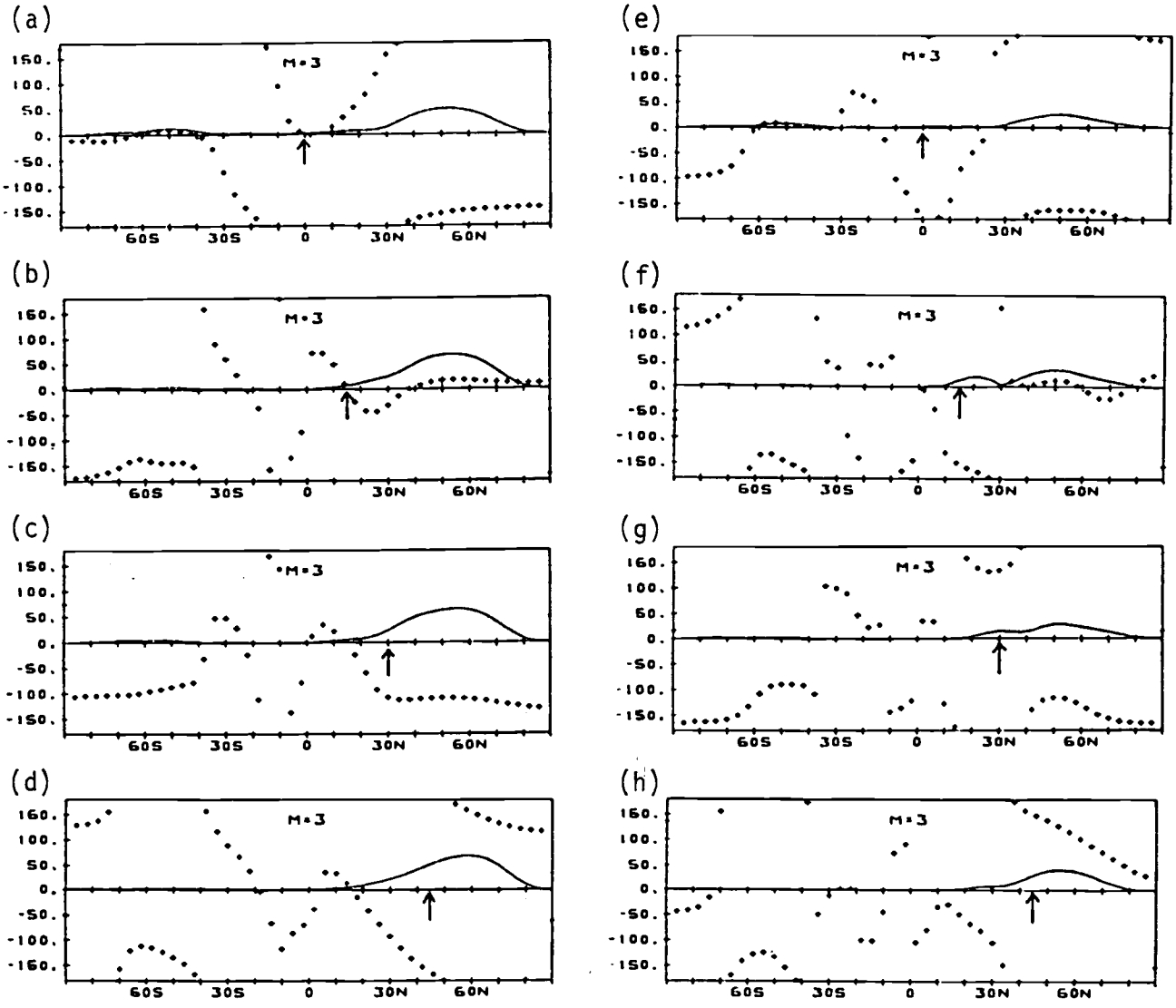

Fig. 5.16. As in Fig. 5.14 except for zonal wavenumber 3.

6. QUASI-STATIONARY ATMOSPHERIC RESPONSES TO SEA SURFACE TEMPERATURE ANOMALIES

As discussed in Chapter 2 several observational and GCM studies have demonstrated the importance of tropical SST anomalies on the planetary wave fluctuations. To understand the dynamics involved many simple model studies have recently been performed (Opsteeph and van den Dool, 1980; HK; Webster, 1981; Simmons, 1982). These studies have explained the general aspects of the observed atmospheric anomalies using the dynamics of Rossby wave propagation. In the above studies, however, the atmospheric heating rates which might result from the SST anomaly were prescribed, frequently in an idealized way which might not be consistent with the observations. Because of the simple treatments of SST anomalies in the previous studies there is still uncertainty in the linear response to the SST anomalies. In this chapter we therefore attempt to clarify this issue by using a comprehensive linear model which directly takes into account the SST anomalies. In particular, because both surface and cumulus heating may be important mechanisms for atmospheric heating by SST anomalies especially in the tropics, these processes are parameterized in the present baroclinic model. This model is also used here to investigate the effect of climatological tropical and Pacific SST distribution on the atmospheric standing waves, and the response to midlatitude SST anomalies.

In the present experiments the dissipations discussed in Chapter 3 appear to be too small, and the 20-day integration period of the model is too short to obtain a quasi-steady state solution. Thus the

dissipation coefficients are increased here to the value of $1. \times 10^{-6}$/sec., and the model integration period is extended to 40 days.

6.1 Parameterization of the atmospheric heating

6.1.1 Sensible heat flux

The sensible heat flux at the surface is often parameterized by the following bulk aerodynamic formula,

$$H_s = c_p C_D |V_s| (T_o - T_a) \tag{6.1}$$

where C_D is the transfer coefficient, $|V_s|$ the surface wind speed, T_o the ocean surface temperature, and T_a the air temperature above the surface. In the present experiment, $C_D = 1.2 \times 10^{-3}$ is used, and $|V_s|$ is approximated by the following linearized form assuming $\bar{u}^2 \gg u'^2$ and $\bar{u}^2 \gg v'^2$,

$$|V_s| \approx |\bar{U}_s| \left\{ 1 + \frac{u_s'}{\bar{u}_s} \right\} \tag{6.2}$$

Substituting (6.2) into (6.1), a linearized form for the sensible heat flux can be obtained as

$$H_s' = c_p C_D \left[|\bar{u}_s| (T_o' - T_a') + |\bar{u}_s| \frac{u_s'}{\bar{u}_s} (\bar{T}_o - \bar{T}_a) \right] \tag{6.3}$$

In the above formula the sensible heat flux is determined not only by the difference between the temperature deviations of ocean and air at the surface, but also by the deviation of zonal wind magnitude.

6.1.2 Latent heat flux

The bulk aerodynamic formula for the latent heat flux at the surface may be written as

$$H_E = L C_D |V_S| (q_o^* - q_a) \tag{6.4}$$

where L is the latent heat of vaporization per unit mass of water, q_o^* the saturation specific humidity at the surface, and q_a the specific humidity of air above the surface. Since the present model does not have a water vapor equation the perturbation part of the specific humidity is expressed in terms of the atmospheric temperature as discussed below.

The specific humidity and the saturation vapor pressure to a first order of approximation may be expressed as in (6.5) and (6.6), respectively

$$q = 0.622\, e / p_o \tag{6.5}$$

$$e^* = 10^{\left(9.4051 - \frac{2354}{T}\right)} \tag{6.6}$$

where p_o is the pressure at the surface, e the vapor pressure, and the superscript star represents saturation. Substituting the temperature

($T_0 = \overline{T}_0 + T_0'$) into (6.6), the saturation vapor pressure may be further approximated as follows:

$$e_o^* \approx 10^{\left(9.4051 - \frac{2354}{\overline{T}_o}\right)} 10^{\frac{2354\, T_o'}{\overline{T}_o^2}}$$

$$\approx \overline{e}_o^* \left[1 + (a \ln 10)\, T_o' \right] \tag{6.7}$$

where $a = 2354/\overline{T}_o^{\,2}$ and e_0^* is given by (6.6) with T replaced by $\overline{T}_o$. The above equation has used the following approximation.

$$10^x = (e^x)^{\ln 10} \approx 1 + x \ln 10$$

The vapor pressure of the air above the surface may also be approximated as in (6.7)

$$e_a \approx \varepsilon\, \overline{e}_a^* \left[1 + (b \ln 10)\, T_a' \right] \tag{6.8}$$

where $b = 2354/\overline{T}_a^{\,2}$ and ε is the relative humidity which is assumed to be a constant. This assumption is based on the fact that on the climatological time scale the relative humidity is approximately constant in the tropics. Then, using (6.7), (6.8) and (6.5), the specific humidity difference, $q_o^* - q_a$, is approximated as

$$q_o^* - q_a = \overline{q}_o^* \left[1 + \ell\, T_o' \right] - \overline{q}_a \left[1 + \ell\, T_a' \right] \tag{6.9}$$

where $\ell \approx a\ell n10 \approx b\ell n10$.

The substitutions of (6.2) and (6.9) into (6.4) now give the following linearized equation for the latent heat flux.

$$H_E' = L C_D \left[|\bar{u}_s| \ell \left(\bar{q}_o^* T_o' - \bar{q}_a T_a' \right) + |\bar{u}_s| \frac{u_s'}{\bar{u}_s} \left(\bar{q}_o^* - \bar{q}_a \right) \right] \tag{6.10}$$

where the value of $0.06/(^\circ K)^2$ is used for ℓ. In (6.10) H_E' depends on two factors: the difference between the humidity deviations of the ocean and air at the surface, represented in terms of the zonal mean humidity and the temperature deviations, and the deviation of zonal wind magnitude.

In the present model the surface fluxes uniformly heat the lower layer. Therefore, the lower-layer heating due to the surface fluxes Q_s' is obtained by dividing the sum of (6.3) and (6.10) by the total mass per unit area in the lower layer.

$$Q_s' = \frac{H_s' + H_E'}{500mb/g} \tag{6.11}$$

The zonal mean quantities used in the above calculation have been obtained from the global January climatology documented by Esbensen and Kushnir (1981).

6.1.3 Cumulus heating

The latent heat release by cumulus convection is now known to be the major heat source for the tropical atmosphere, although details of the actual heating process are not clearly understood. Charney and Eliassen (1964) parameterized the cumulus heating to be proportional to the vertical velocity at the top of the boundary layer. Similar methods have been widely used in the tropical modeling studies with considerable successes (Yamasaki, 1968; Hayashi, 1970). We thus adopt a similar technique and formulate the cumulus heating as

$$Q_L'(\sigma) = -C(\sigma)\,\omega' \tag{6.12}$$

where ω' is the vertical velocity (dp/dt) at $\sigma = 0.5$, and $C(\sigma)$ is a heat distribution parameter. The cooling due to $\omega' > 0$ in (6.12) is interpreted as a less than average heating. This interpretation is partly based on the observational evidence that over the Indonesian Ocean upward motion is reduced during El Niño episodes, resulting in weaker convective activity there. At present there is little theoretical or observational basis from which one can determine $C(\sigma)$. We therefore tune this parameter so that the simulated heating is comparable with the observed heating in the tropics. The value of $C(\sigma)$ is chosen to be -22 for both layers, by assuming that the maximum heating due to cumulus convection occurs at 500 mb, and that the partition between the upper and lower layers in the tropics is equal.

6.2 Tropical SST anomaly experiment

We examine here the responses of the model atmosphere to the equatorial Pacific SST anomaly taken from Rasmusson and Carpenter (1982). This SST anomaly depicts the mature phase of an El Niño episode. It should be noted, however, that the magnitude of the present anomaly is twice as large as that observed. This choice is largely based on the fact that the magnitude of the observed anomaly field, with maximum about 1.5°C, appears to be too small to be representative of distinctive El Niño events. In fact, Weare (1982) suggested that El Niño should be modeled with a warm anomaly of 2.5°C in the east, and a weak cold anomaly of -0.5°C west of the dateline. The SST anomaly shown in Fig. 6.1 is consistent with what Weare suggested.

The height responses in the Northern Hemisphere to the SST anomaly are shown in Fig. 6.2. Figs. 6.2a, b, and c show the 250 mb heights at day 20, 30, and 40, respectively, and Fig. 6.2d the 750 mb height at day 40. The pattern of the 250 mb height at day 20 shows planetary-scale waves. By day 40 this pattern is completely masked by relatively small-scale waves. These small-scale waves are evidently due to baroclinic instability. In fact, several characteristics of growing baroclinic waves are evident in Figs. 6.2c and d. The phase of the waves is tilted to the west with height, and the horizontal orientation is NW-SE to the north of the center of the waves and NE-SW to the south. Both the horizontal and vertical structures of these waves are in good agreement with those of baroclinically unstable waves as analysed by Eady (1949) and Charney (1947).

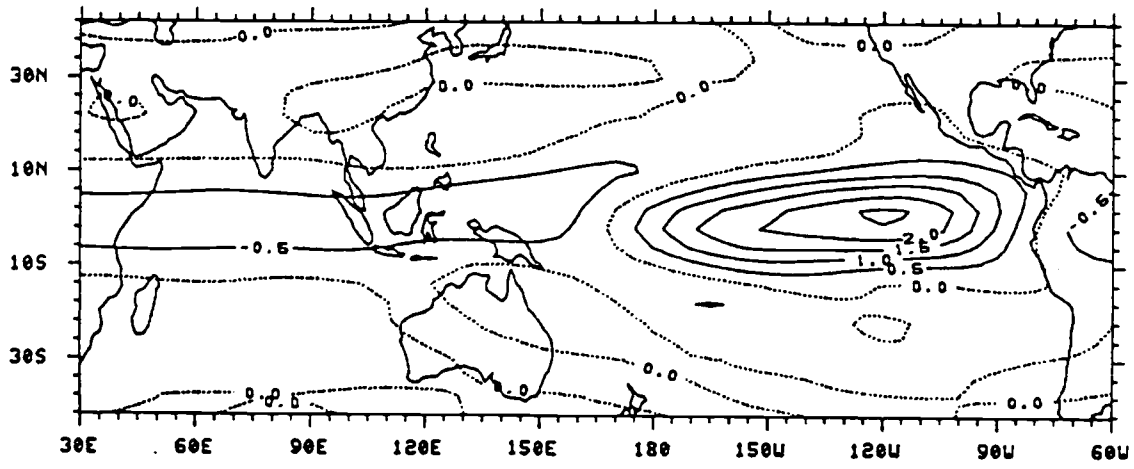

Fig. 6.1. Tropical SST anomaly represented by 6 zonal wavenumber components and 15 associated Legendre polynomials. Unit: °C.

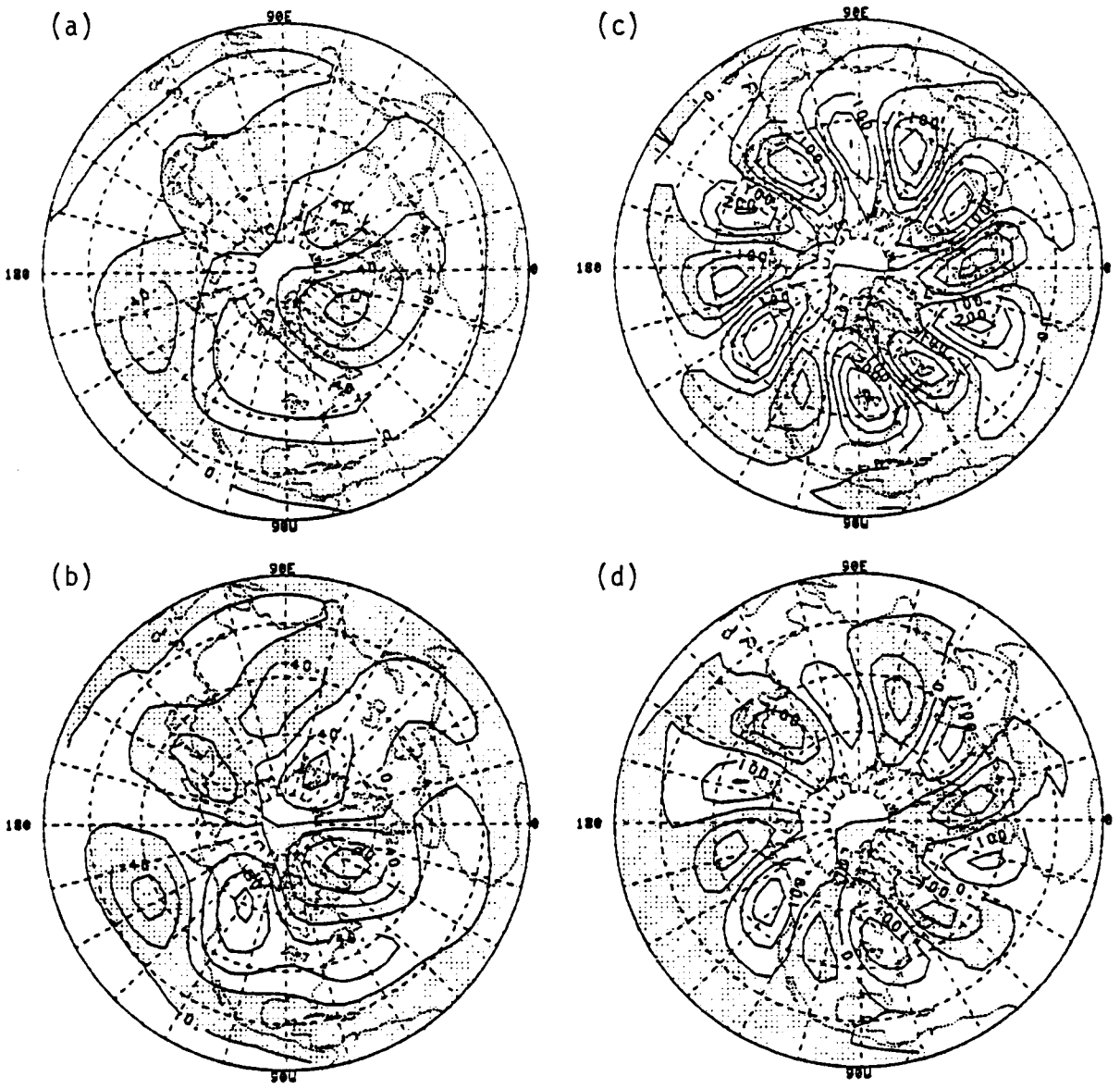

Fig. 6.2. Height response to the tropical SST anomaly. Shown are the 250 mb responses at (a) day 20, (b) day 30, and (c) day 40, and (d) the 750 mb response at day 40. Calculations have been made with 6 zonal wavenumber components. Contour intervals are 40 meters for (a) and (b), and 100 meters for (c) and (d).

Since the baroclinically unstable waves (m = 5 and 6) are not of our immediate interest in the present study, these wave components have been excluded. The panels in Fig. 6.3 show the 250 mb height responses with only wavenumbers m = 1, 4. The arrangement of the figures is as in Fig. 6.2. As expected, the baroclinic eddies are completely eliminated, and only the planetary-scale waves propagating along a great circle are evident. The stationary wave pattern appears to be well established by day 20, although the amplitudes still increase with time, particularly to the east of the anomaly. After day 30 the amplitudes do not change significantly, indicating a quasi-steady state being reached. Figs. 6.3c and d also show typical barotropic structure in the wavetrain.

Although a quasi-steady state is reached after day 30, the time mean over last 20 days of the 40-day integration has been taken for the purpose of presentation of subsequent results. The time mean height responses are shown in Figs. 6.4a and b for 250 mb and 750 mb, respectively. In general, the pattern of the responses is found to resemble the observed atmospheric anomalies documented by Horel and Wallace (1981) and shown schematically in Fig. 2.4. The negative response over the North Pacific and the positive response over Canada are especially notable. The amplitude of the response over the North Pacific, however, appears to be somewhat weaker than the observed. This may be due to the lack of a zonally varing basic state as suggested by Simmons et al. (1983). Interestingly, the large negative response over Greenland has also been simulated by Shukla and Wallace

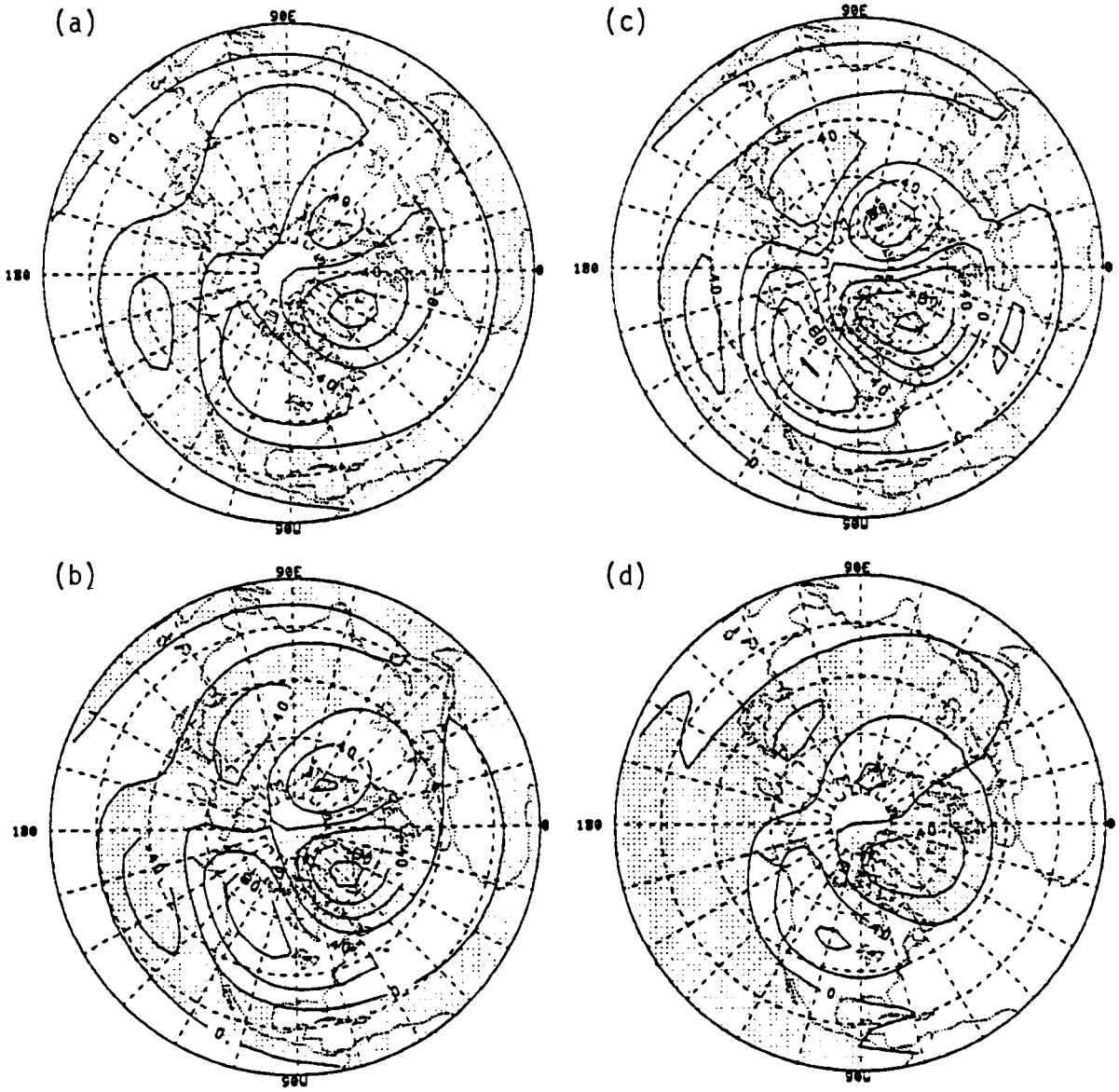

Fig. 6.3. As in Fig. 6.2 except for the responses with zonal wavenumber components 1 through 4.

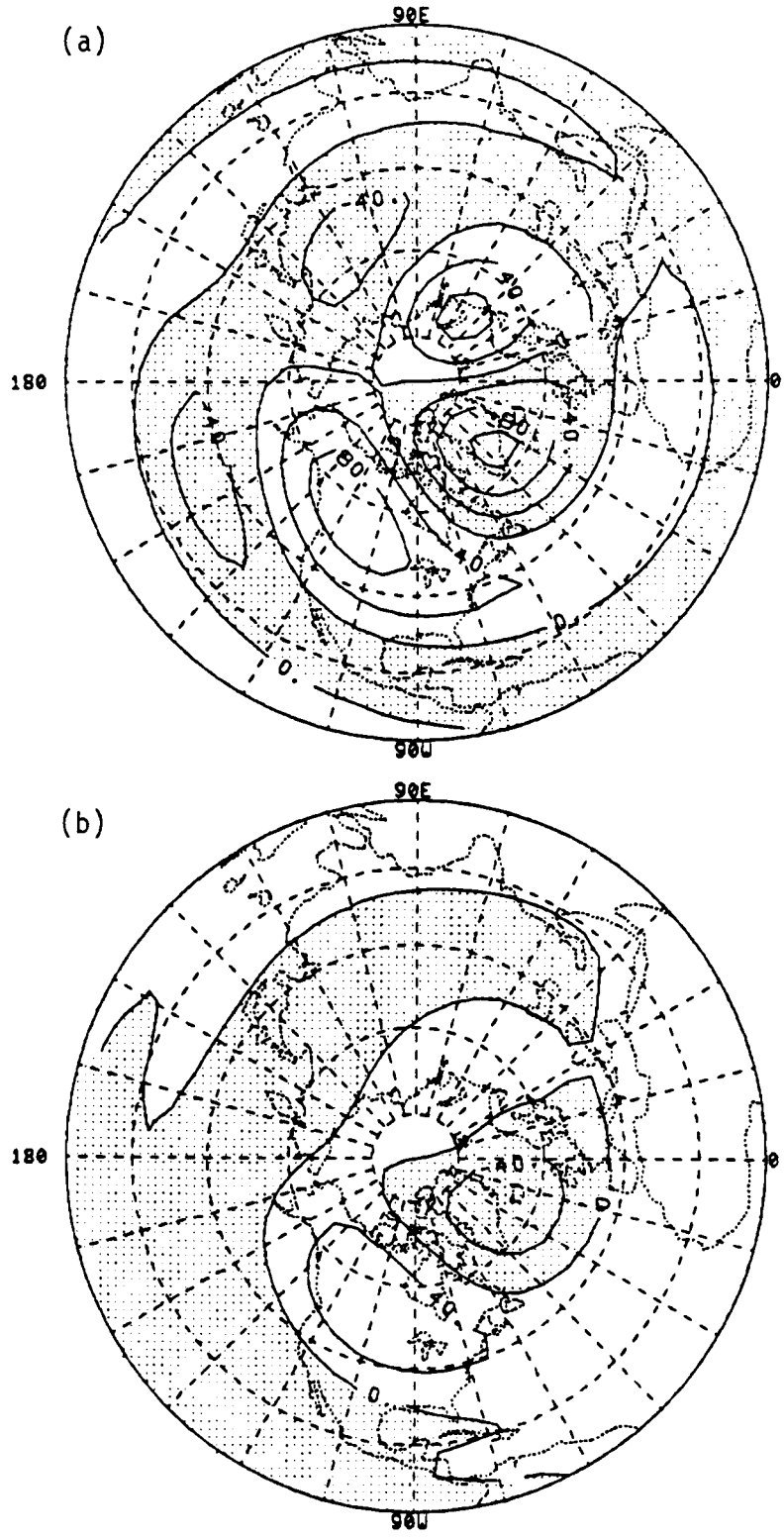

Fig. 6.4. The 20-day mean response with zonal wavenumber components 1 through 4. Shown are (a) 250 mb height and (b) 750 mb height. Contour intervals are 40 meters.

(1983) in their GCM experiments for a tropical SST anomaly whose horizontal distribution is the same as that of the present SST anomaly.

For the purpose of comparision we have also taken the time mean of the results in which all 6 zonal wavenumber components are included. In comparing Fig. 6.5 with Fig. 6.4 the differences between the two cases are found to be small. To better portray the planetary-scale responses, we shall therefore present the experimental results obtained using only four zonal wavenumbers.

The heating fields simulated by the model are shown in Figs. 6.6a and b for the upper and lower layers, respectively. Although the magnitudes of the lower-layer heating are somewhat larger than those of the upper layer, the patterns of both layers are very similar. These results indicate that a large portion of the total heating is due to the cumulus heating. As discussed in the previous chapter, in the tropics the initial heating due to the surface heat fluxes should be balanced by adiabatic cooling due to upward motion. This vertical motion, in turn, induces cumulus heating in both layers; this is a positive feedback between the heating and dynamically-induced motion field. We may therefore expect large heating anomalies in the tropics. Both the horizontal shape and magnitude of the positive heating over the central equatorial Pacific, with vertically averaged maximum of order 5°/day (10 mm/day), are in good agreement with the observations (Horel and Wallace, 1981; Kahlsa, 1983) and the GCM result shown in Fig. 2.5b. The simulated phase lag of the positive heating anomaly relative to the SST is also found in the observations of Kahlsa (1983). The negative heating anomaly over South America appears to be significant, although

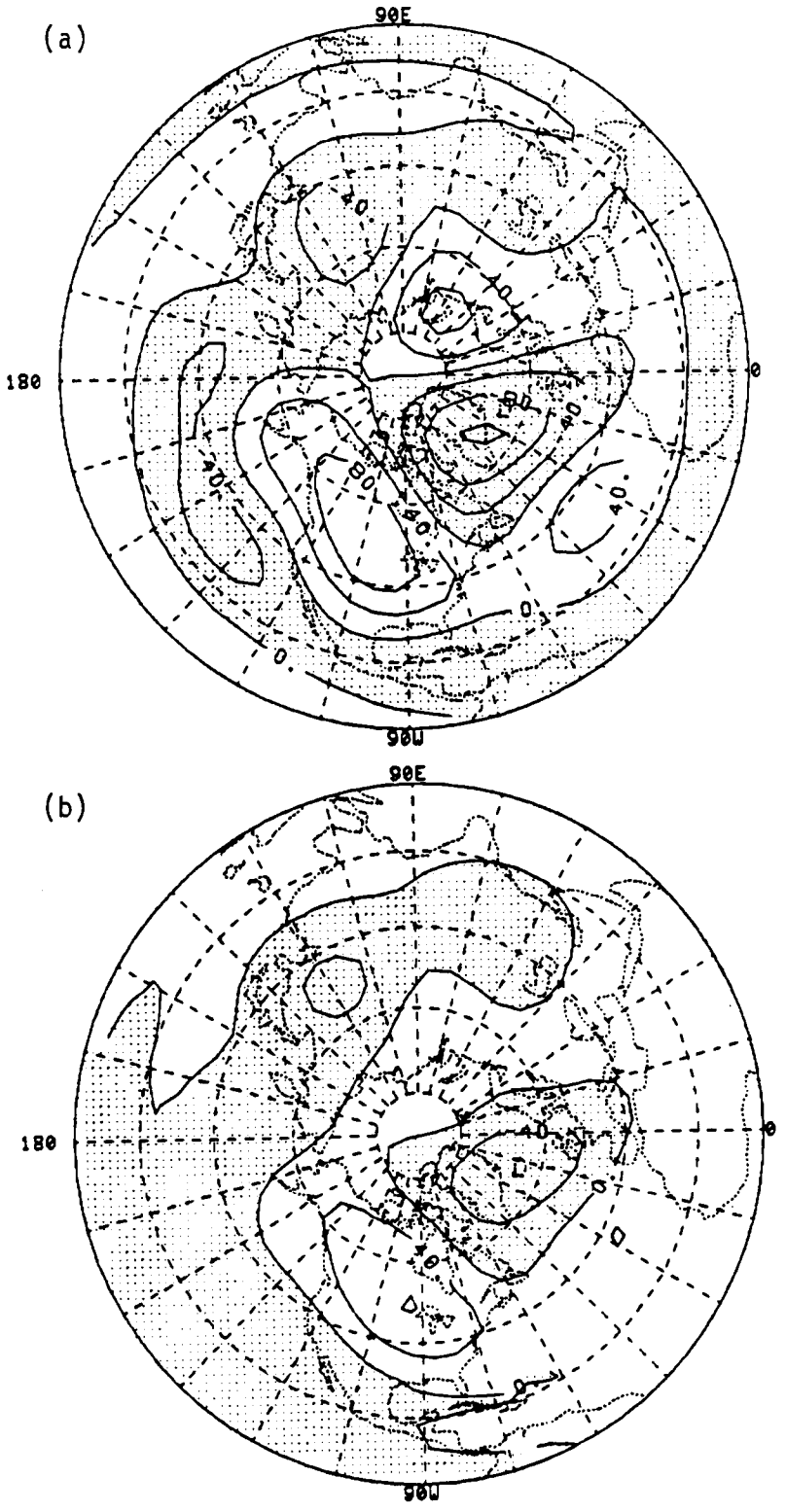

Fig. 6.5. As in Fig. 6.4 except for the responses with zonal wavenumber components 1 through 6.

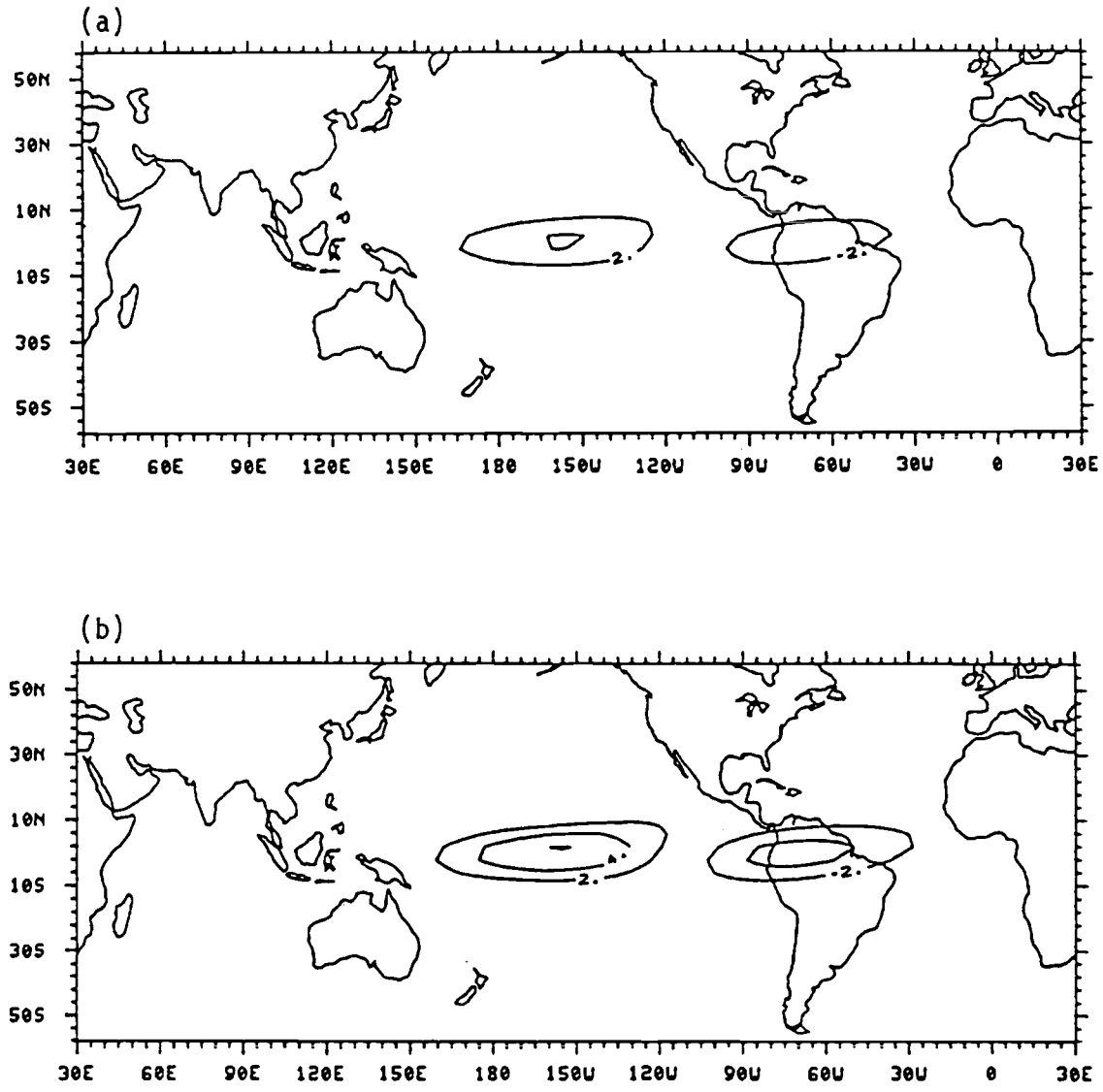

Fig. 6.6. The model simulated heating fields for the tropical SST anomaly. (a) The upper layer. (b) The lower layer. Unit: °K/day.

the degree of its realism cannot be judged at present due to the lack of observations. Interestingly, however, a similar feature with relatively smaller magnitude was simulated by a GCM (Blackmon et al., 1983).

We now discuss the associated motion fields. The simulated zonal winds at the upper and lower layers are shown in Figs. 6.7a and b, respectively. These figures clearly show a lower-layer westerly to the west of the maximum SST anomaly and an easterly to the east, and the reversed circulation aloft. Another interesting feature in the upper layer is the westerly anomaly over the subtropical central Pacific, which supports the observational evidence of an enhancement of the subtropical jet during El Niño periods. These results are also found to be consistent with the GCM experimental results displayed in Fig. 2.5. The simulated meridional winds shown in Fig. 6.8 reveal several interesting features. The upper-layer southerly and lower-layer northerly over the central tropical Pacific in the Northern Hemisphere certainly imply an enhancement of the local Hadley circulation. Unfortunately, the significance of this feature cannot be asserted at present because of the weak amplitudes. The velocity potentials which represent the divergent part of the motion fields are shown in Figs. 6.9a and b. In the lower layer there is a simple dipole structure of convergence when the atmosphere is being heated and divergence where there is cooling. In the upper layer the same structure occurs with opposite signs. These features of course are intimately related to the simulated vertical velocity and heating patterns. As a matter of fact, the vertical

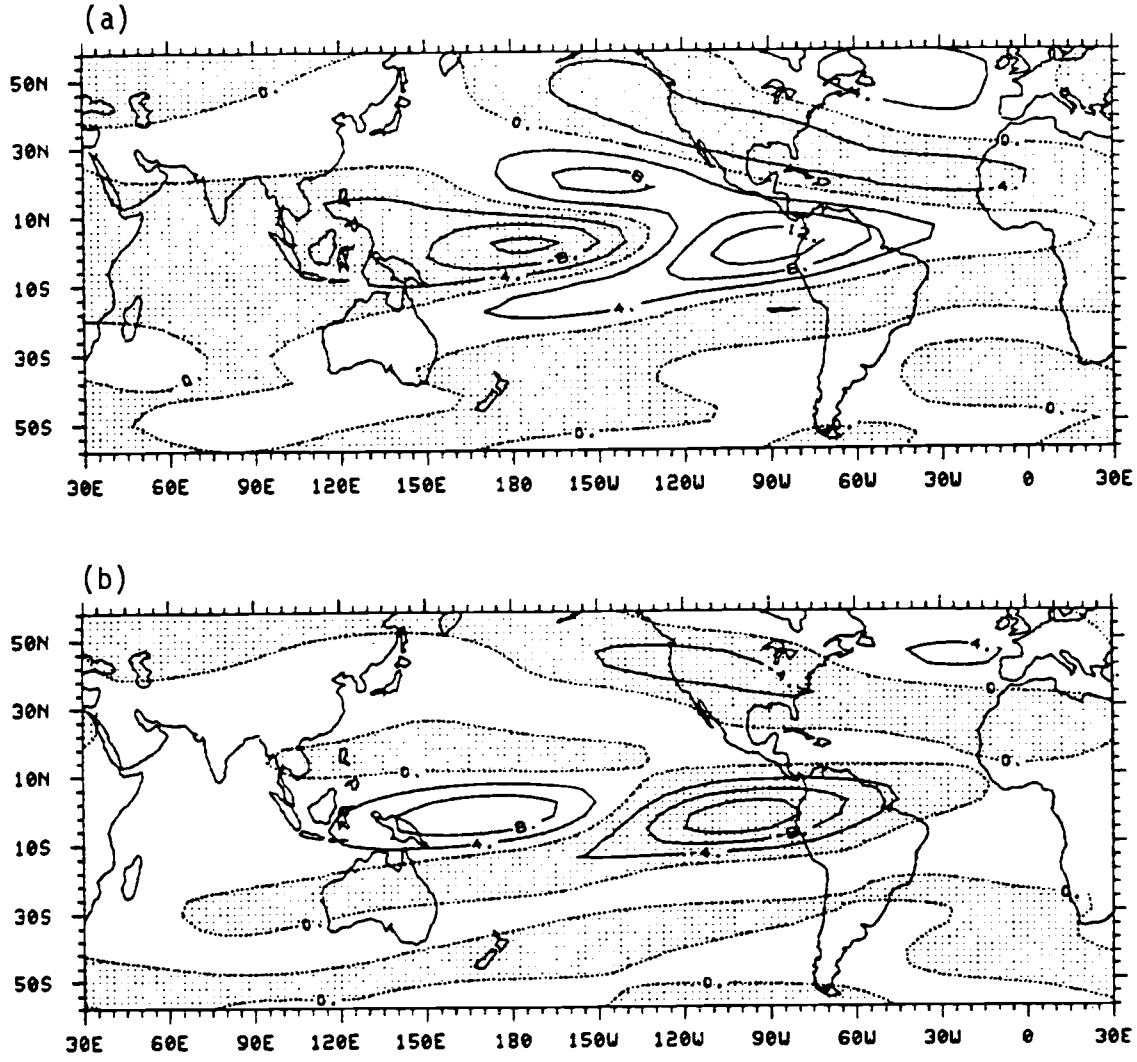

Fig. 6.7. Zonal wind field for the tropical SST anomaly. (a) The upper layer. (b) The lower layer. Contour intervals are 4 m/sec.

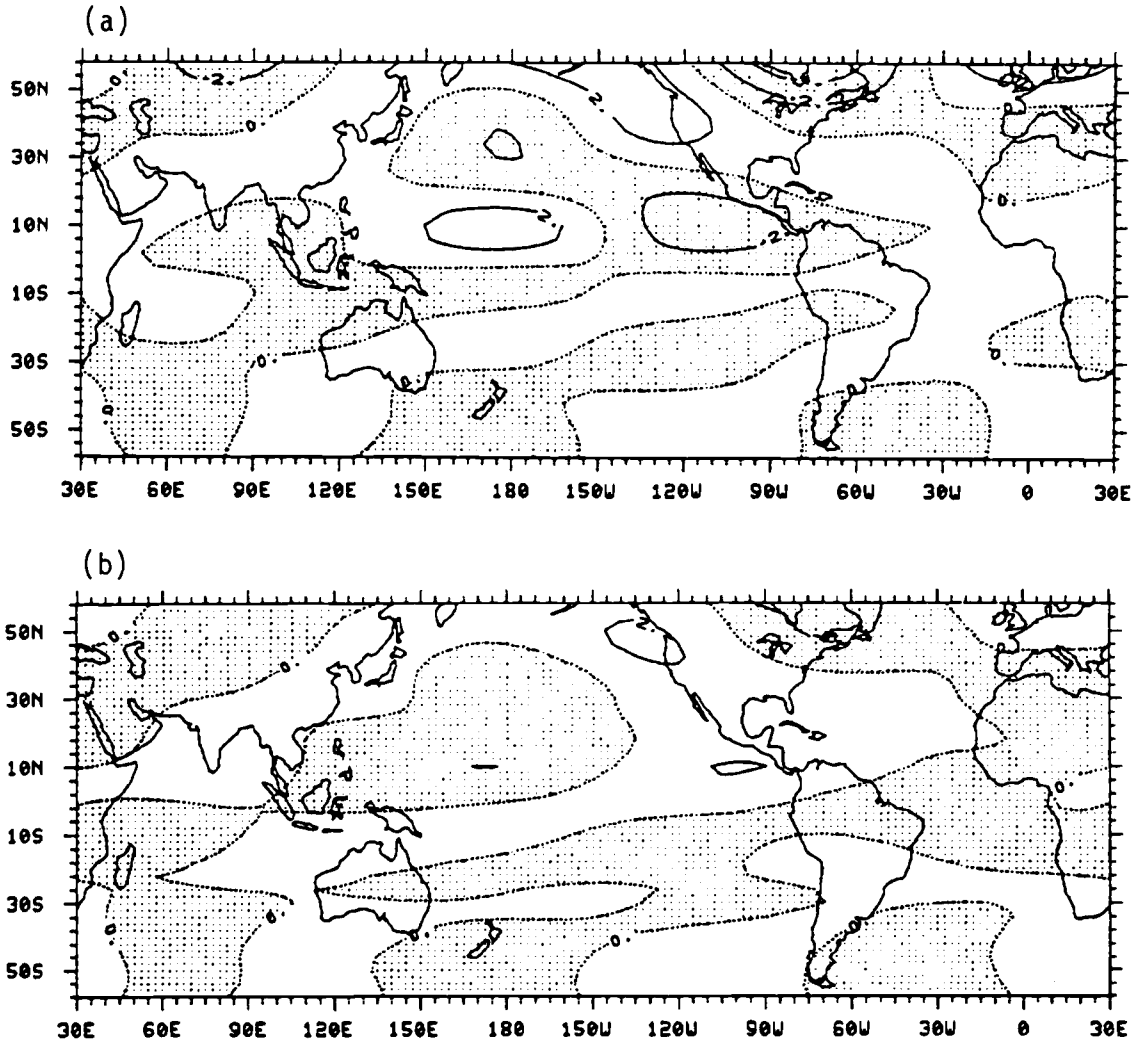

Fig. 6.8. Meridional wind field for the tropical SST anomaly. (a) The upper layer. (b) The lower layer. Contour intervals are 2 m/sec.

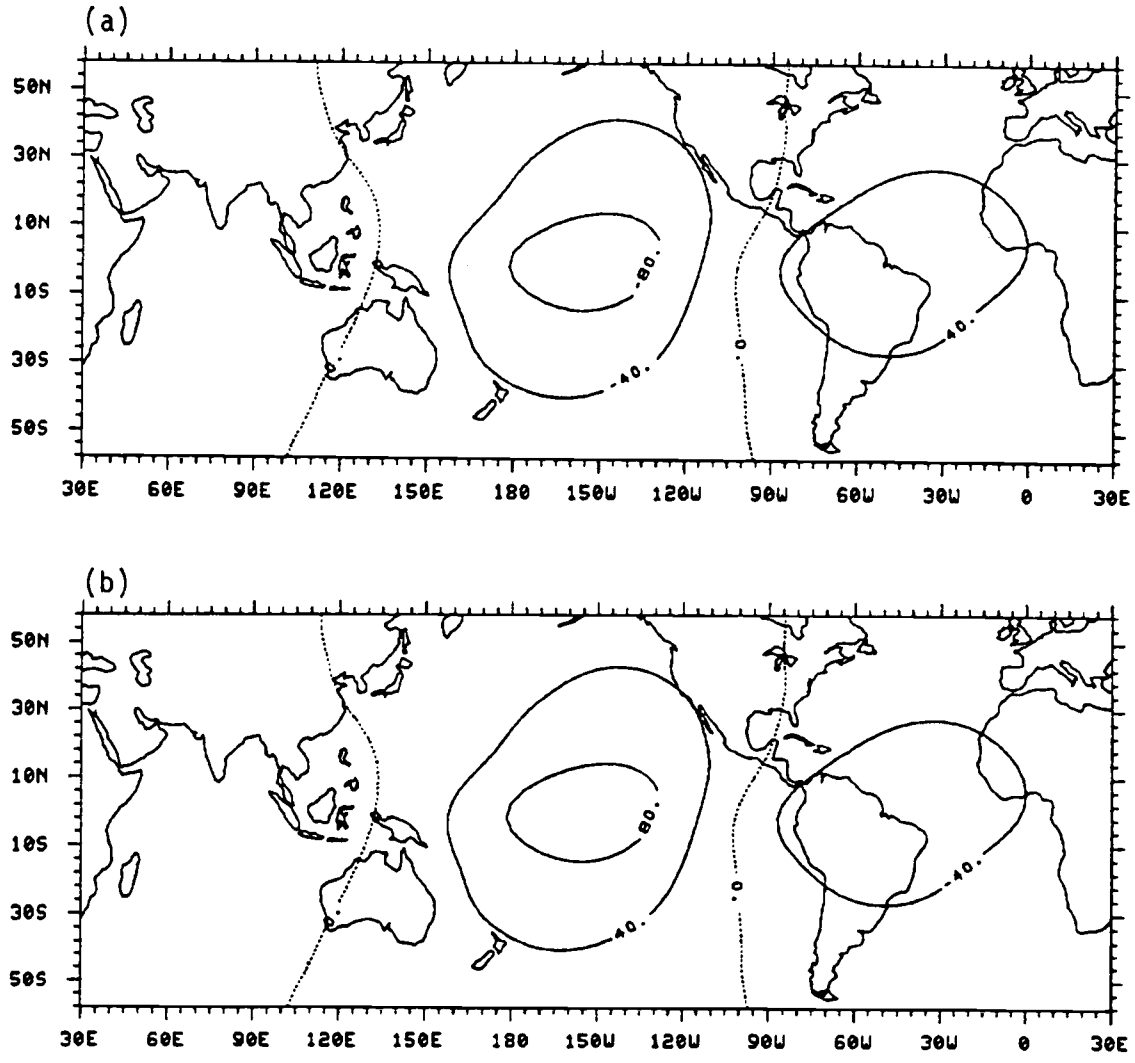

Fig. 6.9. Velocity potential field for the tropical SST anomaly. (a) The upper layer. (b) The lower layer. Contour intervals are 4 x 10^6 m^2/sec.

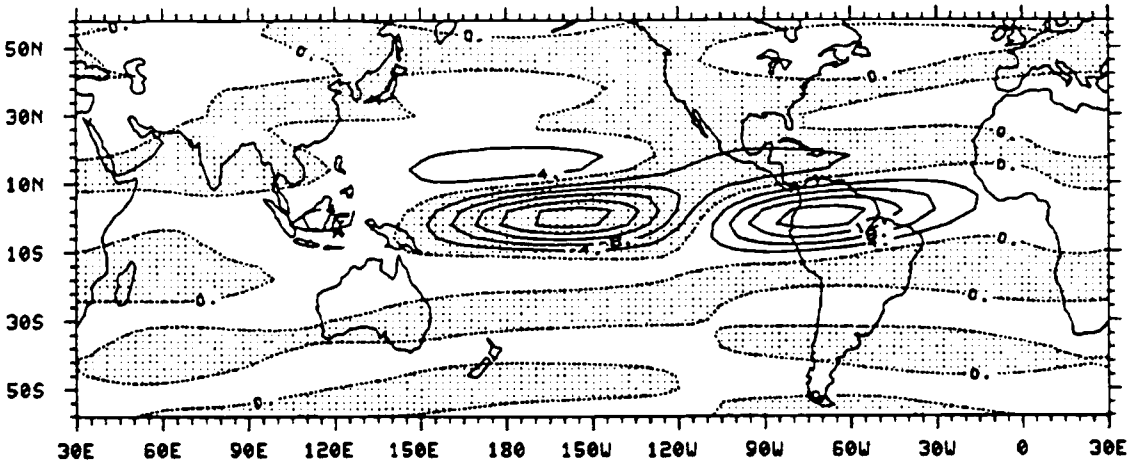

Fig. 6.10. Vertical velocity (dp/dt) field at $\sigma = 0.5$ for the tropical SST anomaly. Contour interval is 2×10^{-4} mb/sec.

velocity field (Fig. 6.10) over the tropics has approximately the same horizontal distribution as those of the heating and divergence fields.

6.3 Impact of the tropical Pacific SST on the maintenance of climatological standing waves

Now that we have discussed the importance of the tropical SST anomaly on both middle latitude and tropical circulation anomalies, it is natural to raise the question: To what extent does the climatological SST distribution in the tropics possibly influence the global standing waves?

To answer this question we examine the model responses to a simplified climatological SST. The tropical Pacific SST field in the domain 22°S-22°N and 60°E-90°W obtained from the January global SST data (Esbensen and Kushnir, 1981) is displayed in Fig. 6.11a. Here the data needed at several land points are simply interpolated from the adjacent values. The deviations obtained by subtracting the sector zonal mean from the SST are then represented spectrally (Fig. 6.11b). In this figure large negative deviations over the eastern tropical Pacific and relatively weak positive deviations over the western Pacific are clearly seen.

The simulated heating fields at both layers are shown in Fig. 6.12. A relatively large cooling is simulated over the central equatorial Pacific, and heating over the northern part of South America and the Indonesian Ocean, the latter only in the lower layer. However, the "cooling" and "heating" in this linear model are relative to the zonal average tropical heating; therefore, the responses cannot be

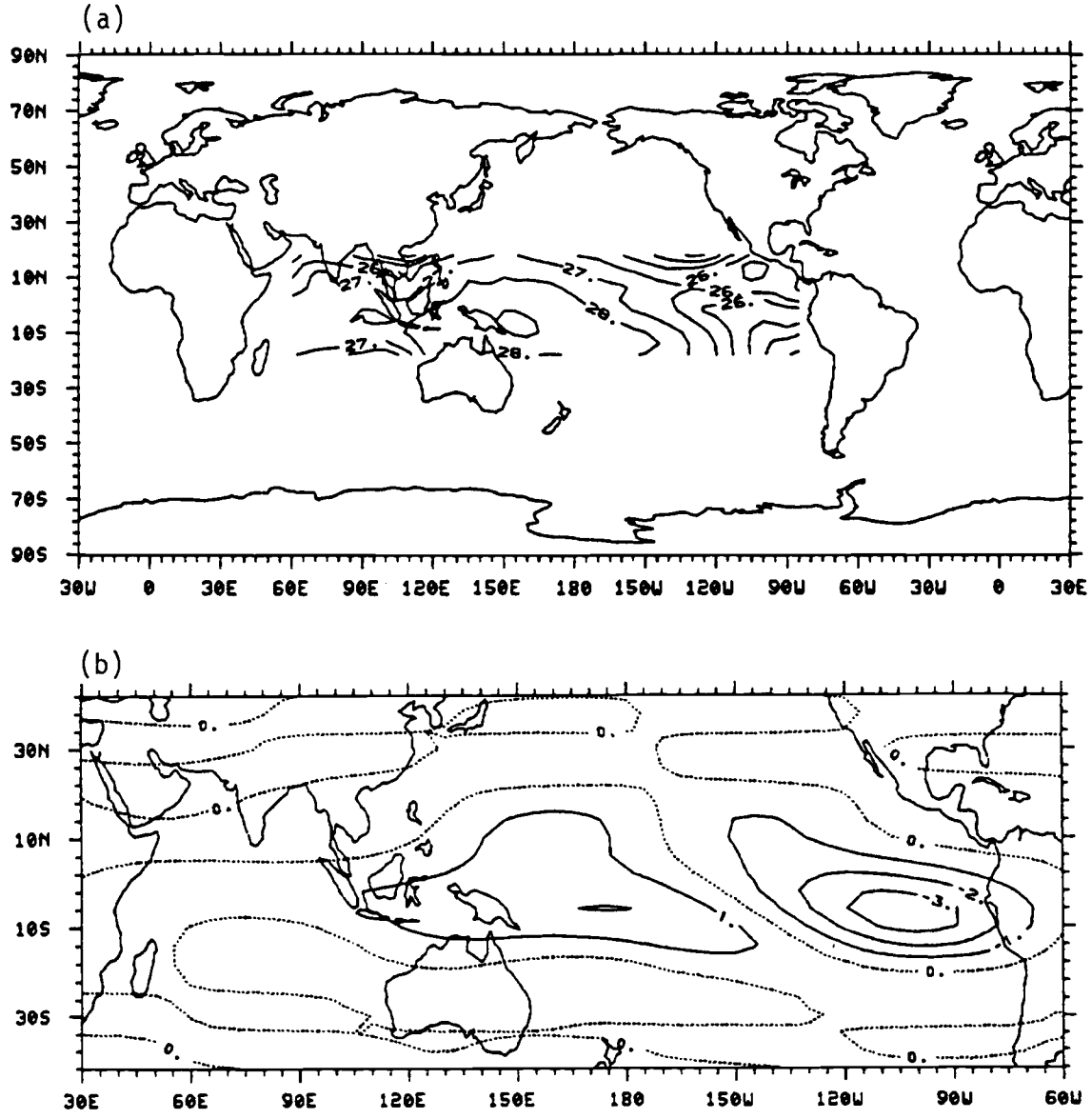

Fig. 6.11. (a) January climatological SST in the domain 22°S-22°N, 60°E-90°W. (b) SST deviation from the zonal mean in the domain. This field is represented by zonal wavenumber components 1 through 4 and 15 associated Legendre polynomials. Units for both figures are °C.

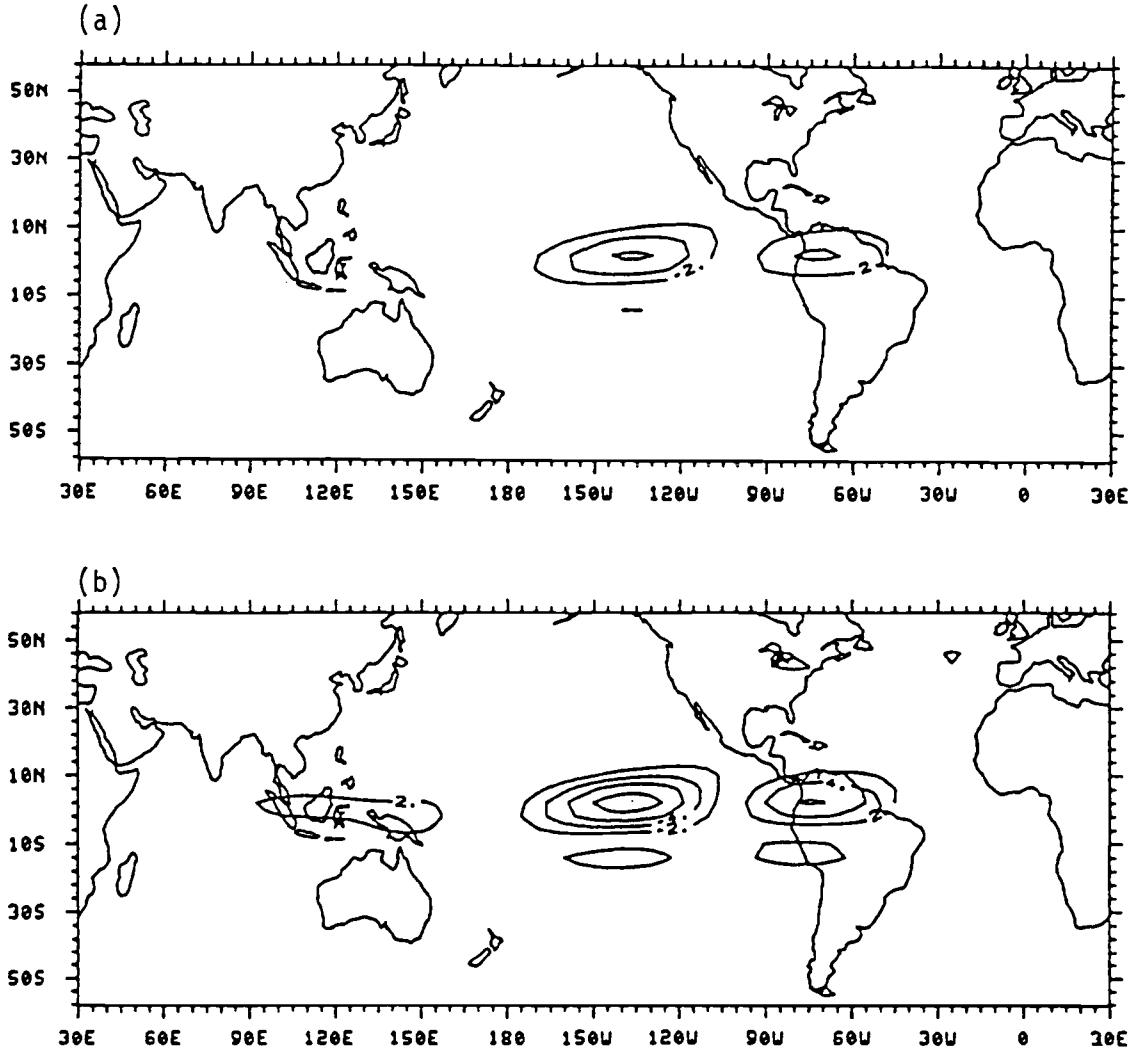

Fig. 6.12. The model simulated heating field for the tropical SST deviation. (a) The upper layer. (b) The lower layer. Unit: °K/day.

directly compared with the observed values. Nevertheless, the general pattern of the simulated heating fields appears to agree with observations available at present. In particular, the simulated large heating over the Amazon is quite consistent with the observed heavy precipitation there. Undoubtedly the longitudinal variation of the Pacific SST is closely related to the corresponding heating pattern as has been documented in numerous observational studies.

The accompaning zonal wind responses at the upper and lower layers are displayed in Figs. 6.13a and b, respectively. One can easily see in these figures the Walker type circulation over the central equatorial Pacific. The positive responses (Fig. 6.13a) off the east coasts of North America and Southeast Asia indicate possible influences of the tropical SST on the subtropical jet.

The simulated geopotential height fields are shown in Figs. 6.14a and b for the 250 mb and 750 mb respectively. Because of the geostropic constraints, the geopotential responses are significant only in the middle and high latitudes. In the tropics, however, large amplitude responses are found in the stream function fields (not shown), which are clearly reflected in the simulated zonal wind fields (Fig. 6.13). For the purpose of comparision, the zonally asymmetric part of January climatological 400 mb and 800 mb heights obtained from the data documented by Schutz and Gates (1971) are shown in Fig. 6.15. It is important to note that some of the features in Fig. 6.14 are in good agreement with the climatological standing waves. Especially notable are the North American trough and ridge over the North Atlantic. The ridge over the west coast of North America in the

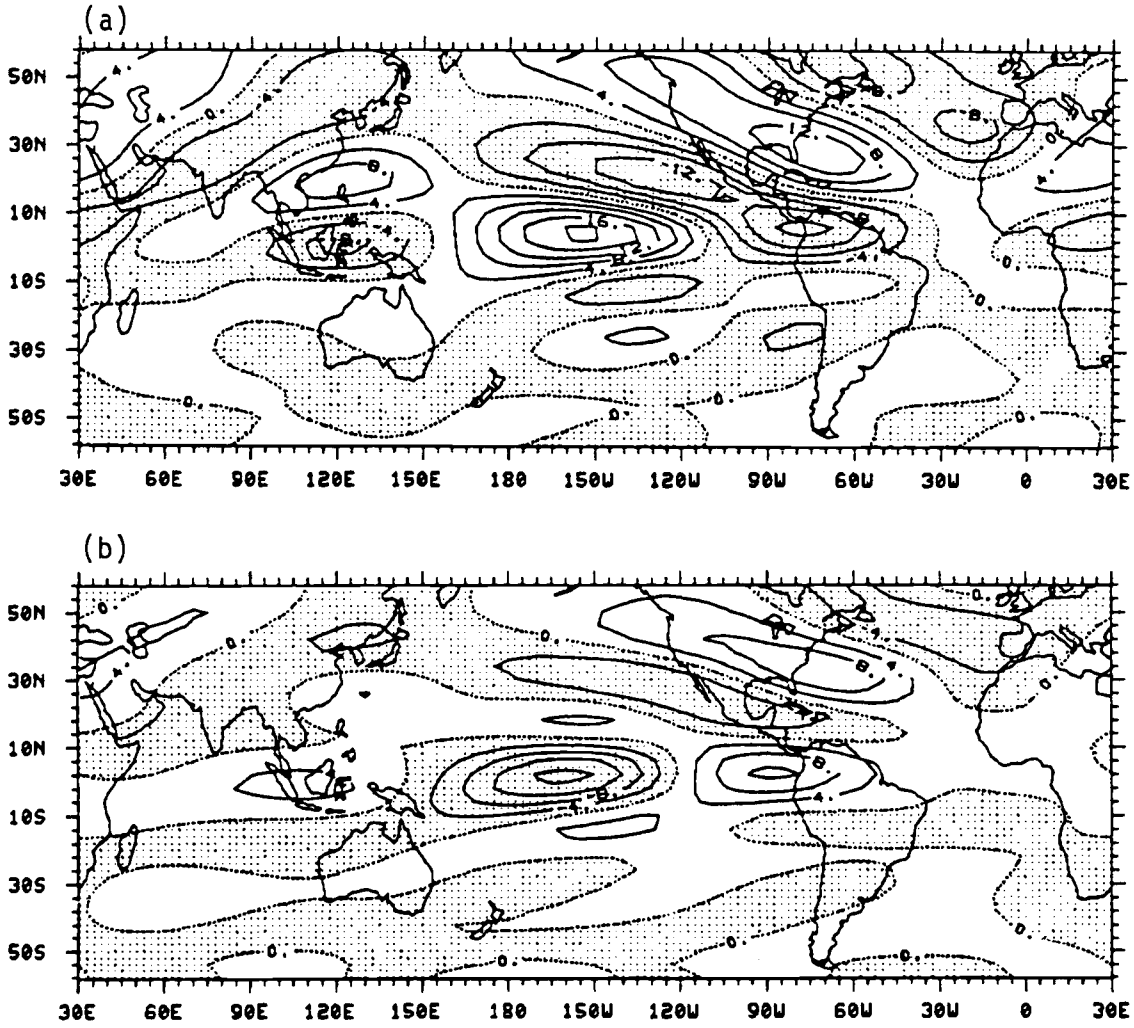

Fig. 6.13. Zonal wind fields at (a) the upper layer and (b) the lower layer for the tropical SST deviation. Contour intervals are 4 m/sec.

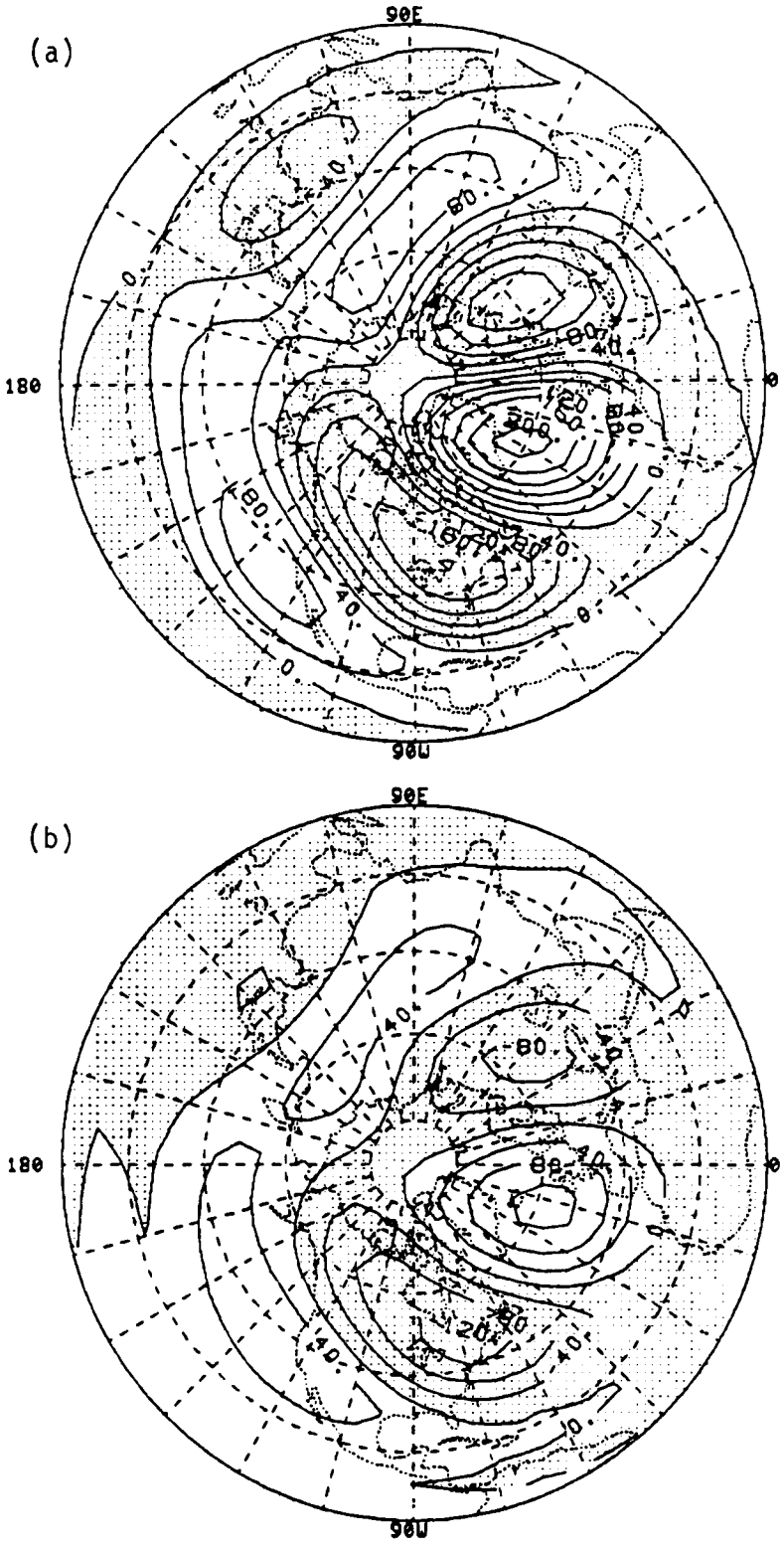

Fig. 6.14. The height response to the tropical SST deviation shown in Fig. 6.11b. Shown are (a) 250 mb height and (b) 750 mb height. Contour intervals are 40 meters.

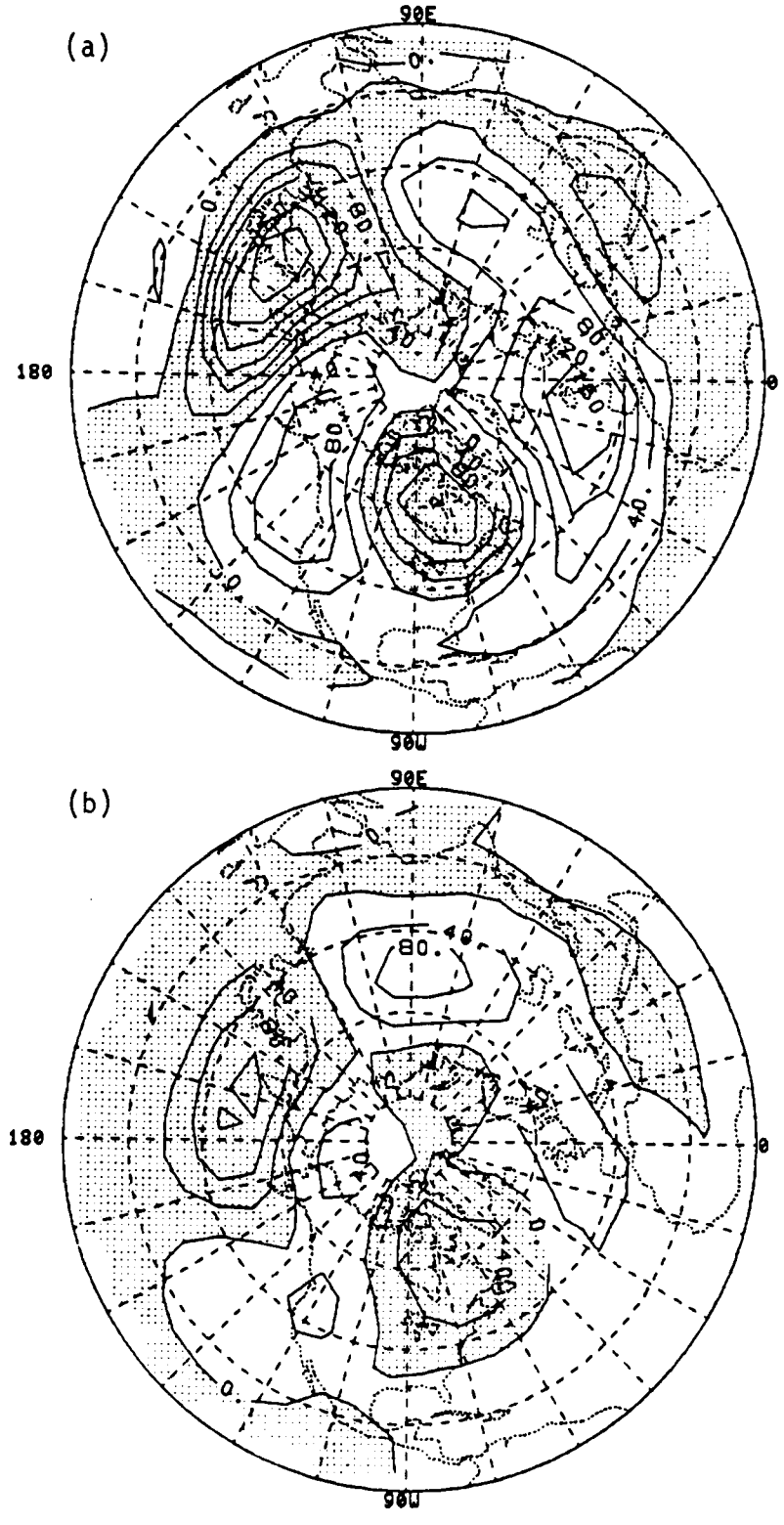

Fig. 6.15. Zonally asymmetric part of January climatological heights at (a) 400 mb and (b) 800 mb derived from the data of Schutz and Gates (1971). Contour intervals are 40 meters.

climatology is also simulated but with a rather small amplitude. It is also worth noting that the barotropic structure of the responses in the middle and high latitudes is generally consistent with the climatological pattern. The present results thus suggest that the tropical Pacific SST can be an important factor in maintaining the climatological standing waves, at least over the western half of the Northern Hemisphere.

6.4 Middle latitude SST anomaly experiment

As briefly mentioned in Chapter 2, the significant geopotential responses to tropical SST anomalies were not reflected in GCM experiments when the anomalies were placed in the middle latitudes (Chervin et al., 1976). Namias (1976), on the other hand, showed observational evidence of a significant correlation between the surface pressure and SST anomalies in the North Pacific. The apparent disparity between the GCM and observational studies needs an explanation. Based on the linear model experiments, Webster (1981) argued that the above discrepancy is due to the different seasons that they chose. His argument was, however, based on the responses of only the zonal wavenumber 1 component, and boundary layer processes were not included in his model. Therefore, it might be worthwhile to reexamine the anomaly effect using the present model which reasonably well simulates the atmospheric responses to tropical SST anomalies.

The SST anomaly used in this section has the sine squared form of an ellipse centered at 40°N and 180° with a major axis of 120° longitude and a minor axis of 30° latitude. The maximum SST anomaly at the

center is 3°C. Figure 6.16 shows the spectral represention of this SST anomaly.

The simulated geopotential heights for the above SST are shown in Fig. 6.17. Comparing these figures with Fig. 6.4, one can see that the responses in the present case are about 5 times weaker than those for the tropical SST anomaly. These weak responses are not surprising because in the middle latitudes the surface heat fluxes, initially induced by the warm SST, are mainly balanced by horizontal advection without causing a significant change of the internal heating. As argued in the previous chapter, the vertical motion must be weak. Figure 6.18 shows that it is even downward over the western flank of the warm SST region and this suppresses cumulus heating there. In fact, the total heating shown in Fig. 6.19 is mainly due to the surface heat fluxes. The lower-layer heating is also about 5 times smaller than that of the tropical SST anomaly case (Fig. 6.6b). The almost negligible heating of the upper layer clearly shows the lack of cumulus heating.

As argued by Webster (1981), during the winter the significant role of horizontal advection in the middle latitudes is related to the strong meridional temperature gradient and the associated strong zonal mean flow. But, if the temperature gradient were small with associated weak zonal flow, the dynamical responses of the system may not be insignificant: i.e., there may be then a large temperature perturbation to balance the heating either by horizontal advection or enhanced convective activity. Therefore, during the summer the atmospheric responses to a middle latitude SST anomaly may be relatively large.

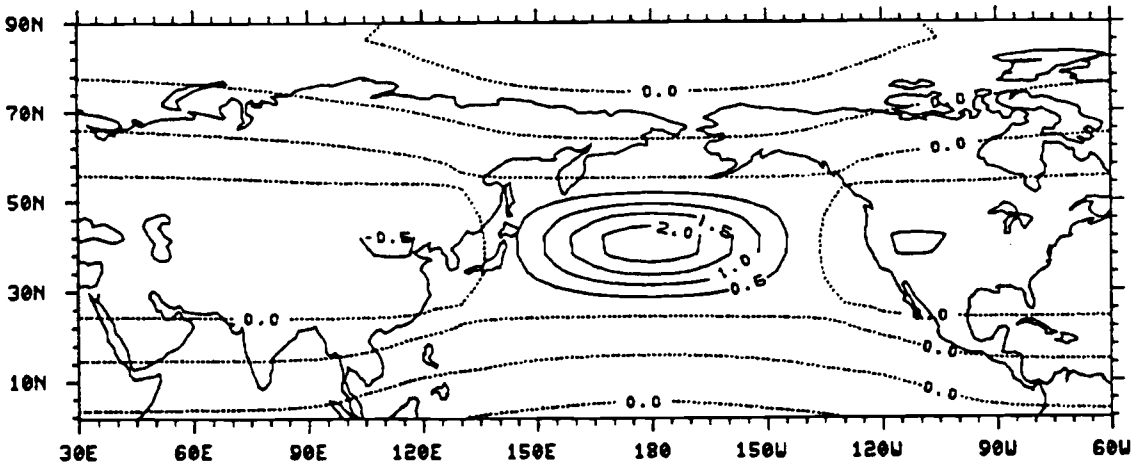

Fig. 6.16. Middle latitude SST anomaly field represented by zonal wavenumber components 1 through 4 and 15 associated Legendre polynomials. Unit: °C.

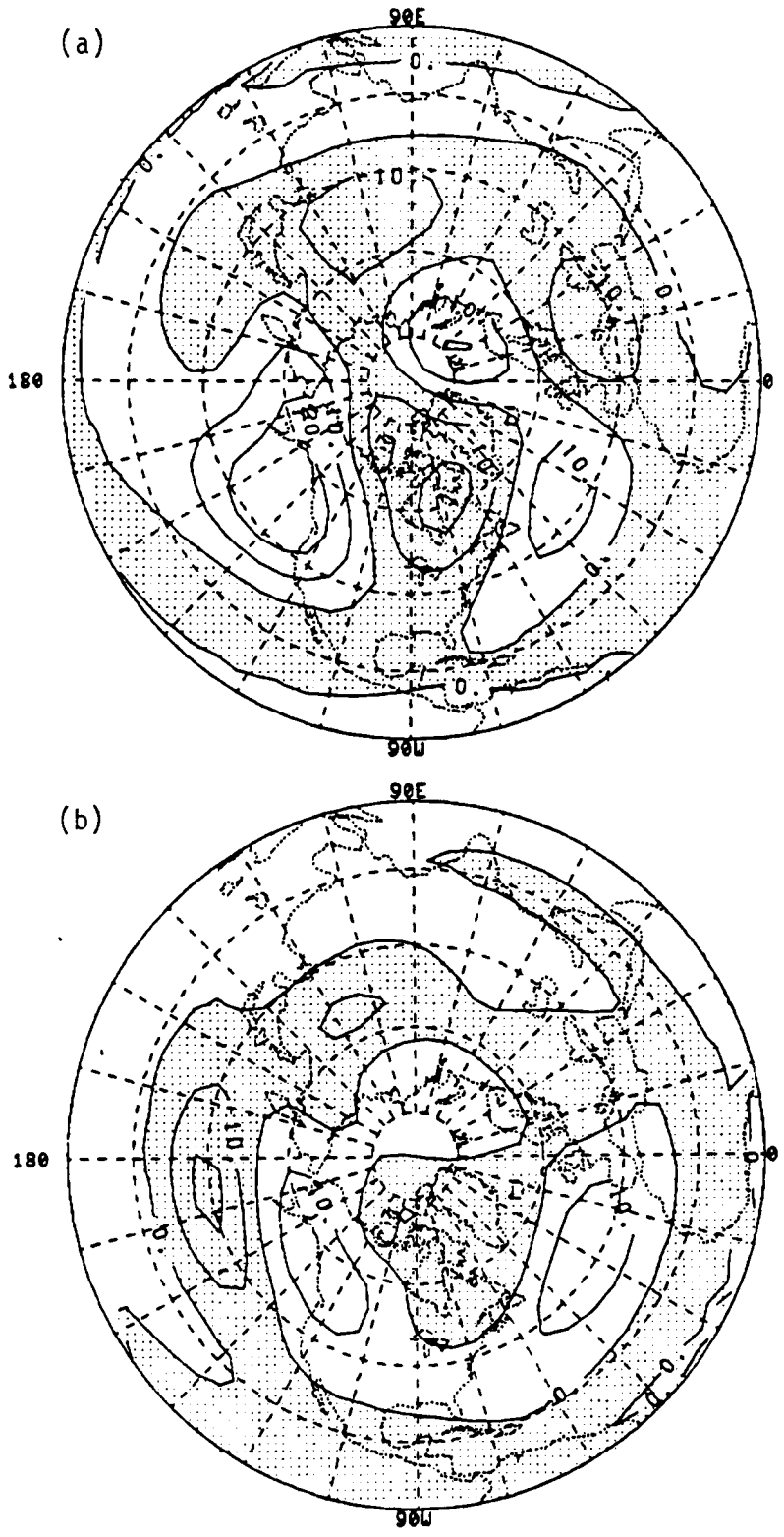

Fig. 6.17. The 20-day mean response to the middle latitude SST anomaly. Shown are (a) 250 mb height and (b) 750 mb height. Contour intervals are 10 meters.

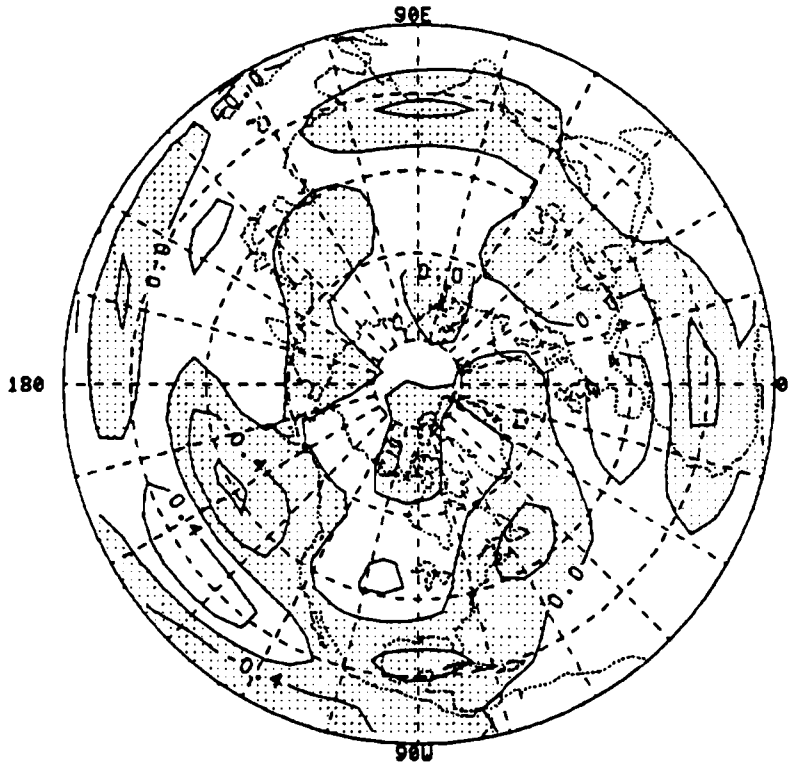

Fig. 6.18. Vertical velocity (dp/dt) at $\sigma = 0.5$ for the middle latitude SST anomaly. Contour interval is 0.4×10^{-4} mb/sec.

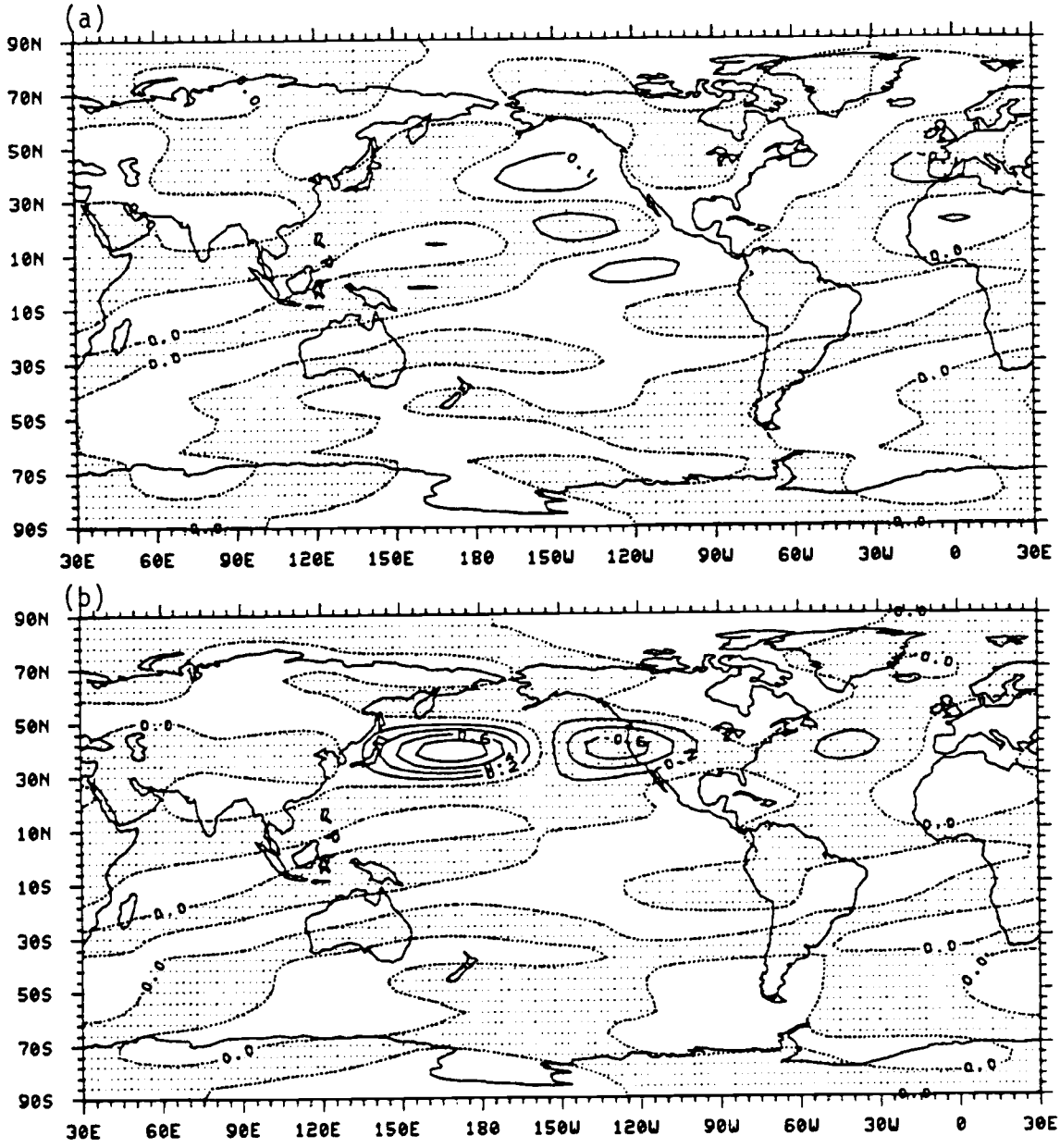

Fig. 6.19. The model simulated heating field for the middle latitude SST anomaly. (a) The upper layer. (b) The lower layer. Contour intervals for (a) and (b) are 0.1° K/day and 0.2° K/day respectively.

The small responses in the present experiment clearly support the GCM experimental results of middle latitude SST anomaly using a winter initial condition (Chervin et al., 1976). The present theoretical argument, which is consistent with that of Webster (1981), may also explain the observed significant effect of a summer SST anomaly on the atmospheric circulation (Namias, 1976).

7. SUMMARY AND CONCLUDING REMARKS

Despite the pronounced impact of tropical SST anomalies on the short-term climate fluctuations, the associated dynamics are as yet incompletely understood. We therefore attempted to clarify the linear dynamical consequences of the SST anomalies. For this study, a linear primitive equation model which includes both surface and internal heating mechanisms was developed. This model was also used to investigate the middle latitude SST anomaly effect, as well as the role of climatological tropical SST on the standing waves. Another objective of the present research was to study the forced planetary wave motion on the sphere. For this objective a simple barotropic model was also developed, and the model results were interpreted in terms of Rossby wave dynamics. In particular, the characteristics of wave responses were examined for each wavenumber component both theoretically and using the model. The baroclinicity of the forced waves was also examined by specifying heat sources in the baroclinic model. In fulfilling these objectives, we have found that both the present barotropic and baroclinic models, as well as the theoretical approach, all give similar results and these are generally in agreement with the observations and GCM results. A conclusion of the present work is therefore that linear processes play an important role in the planetary-wave responses to large-scale vorticity and heat sources, and to SST anomalies.

The experiments for the tropical SST anomaly simulate many aspects of the observed and GCM simulated atmospheric anomalies (Horel and Wallace, 1981; Blackmon et al., 1983). These include the motion and

heating anomalies in the tropics, and the middle latitude geopotential anomalies, particularly over the Pacific/North American sector. Middle latitude SST experimental results are also found to agree with the GCM results (Chervin et al., 1976). In view of the dynamics of the present model, these results suggest that a large portion of the atmospheric anomalies associated with SST fluctuations occur via linear processes.

The above implication of course does not rule out the importance of the other processes because of the simplicity of the model. The parmeterized heating mechanisms in the present model contain several important assumptions. Although these assumptions were largely based on observations, the realism of the present parameterized schemes cannot be judged at present. Nevertheless, the present model simulates heating anomalies that are comparable with observations. Another weakness of the present model for the real atmosphere is the lack of nonlinear dynamics. In fact, the climatological atmospheric states are comprised of standing waves with significant amplitudes superimposed on the westerly zonal current. In the real atmosphere, therefore, the standing waves may influence the forced wave responses. Simmons et al. (1983) in fact show a significant influence of regional barotropic instability on the forced wave solutions. In the present tropical SST anomaly experiment, the weak response over the North Pacific may indicate the importance of such an instability mechanism.

Because of the perceived importance of the feedback between the oceanic and atmospheric anomalies, the coupled system may be needed in order to fully account for the SST anomaly effect on the atmospheric circulation, particularly in the tropics. Cane and Sarachik (1976)

argued that the oceanic response to atmospheric forcing is very rapid in equatorial regions since the baroclinic time scale is weeks at the equator. This may imply that the tropical oceanic anomalies are strongly associated with the atmospheric circulation anomalies. In the present study, however, the basic assumption has been that the time scale of oceanic fluctuations is much longer than that of the variations of atmospheric circulation, thereby specifying constant SST anomalies in the atmospheric model. But the present approach may be justified in the sense of quasi-equilibrium states of both ocean and atmospheric systems. Then, no matter how these equilibrium states are achieved, we may seek the atmospheric state which follows a certain ocean state and vice versa. For instance, during El Niño episodes both ocean and atmosphere have presistent anomalies for time periods greater than seasons. At present, the understanding of the coupled dynamics is very limited and, therefore, a study using the coupled system is important future work.

In the present SST experiments, we found another important possibility: the significant role of climatological Pacific SST on the maintainence of climatological atmospheric standing waves in the middle and high latitudes, as well as in the tropics. This possibility also indicates the important effect of tropical forcing on the middle latitude circulations, as suggested by Simmons (1982). It is therefore suggested that for the correct simulation or prediction of the middle latitude atmospheric pattern, a realistic SST should be prescribed in

the tropics, and the tropical heating mechanisms should be correctly formulated in GCMs or numerical weather prediction models.

For prescribed internal forcings of vorticity and heat sources, both barotropic and baroclinic model experimental results show that the atmospheric responses are dominated by the ultra-long wave components, and that large responses occur for the forcings specified in the subtropics and at the high latitudes near 45°N. These results are consistent with the present theoretical results, and generally are in agreement with the observed low-frequency fluctuations dominated by planetary-scale waves. In Chapter 6, the surface external forcing (SST anomalies) was shown to be important in the tropics but not in the middle latitudes. From these results we may argue that the subtropical forcing associated with fluctuations of the surface conditions (e.g., SST), and high latitude internal forcings that are independent of the changes of surface heat distrbution, may play significant roles on the atmospheric low-frequency variations. In fact, planetary-scale SST fluctuations are often found in the tropics, in particular during El Niño periods, and there is some observational evidence (Horel and Wallace, 1981) that these SST anomalies induce the subtropical vorticity and heat sources. On the other hand, among the high latitude planetary-scale internal forcings, the most notable may be the forcing induced by the nonlinear interaction of synoptic-scale modes, as suggested by Egger and Schilling (1983).

Another interesting finding in the present study is that regardless of the geographical location of the internal forcings, the ultra-long waves behave like a north-south seesaw between the polar and

middle latitudes (m = 1), or between the high latitudes and subtropics (m = 2). Because of the limited documentation of the teleconnection pattern for each wavenumber component, we could not fully compare the present results with observations. Nevertheless, the seesaw of zonal wavenumber 1 component is found to be consistent with that observed by Gambo and Kudo (1983).

REFERENCES

Baer, F., and G. W. Platzman, 1961: A procedure for numerical integration of the spectral vorticity equation. *J. Meteor., 18,* 393-401.

Bjerknes, J., 1966: A possible response of the atmospheric Hadley circulation to equatorial anomalies of ocean temperature. *Tellus, 18,* 820-829.

Bjerknes, J., 1969: Atmospheric teleconnections from the equatorial Pacific. *Mon. Wea. Rev., 97,* 163-172.

Blackmon, M. L., 1976: A climatological spectral study of the 500 mb geopotential height of the Northern Hemisphere. *J. Atmos. Sci., 33,* 1607-1623.

Blackmon, M. L., J. E. Geisler and E. J. Pitcher, 1983: A general circulation model study of January climate anomaly patterns associated with interannual variation of equatorial Pacific sea surface temperatures. *J. Atmos. Sci., 40,* 1410-1425.

Blackmon, M. L., and N.-C. Lau, 1980: Regional characteristics of the Northern Hemisphere wintertime circulation: A comparison of the simulation of a GFDL general circulation model with observations. *J. Atmos. Sci., 37,* 497-514.

Blackmon, M. L., J. M. Wallace, N.-C. Lau and S. L. Mullen, 1977: An observational study of the Northern Hemisphere wintertime circulation. *J. Atmos. Sci., 34,* 1040-1053.

Bourke, W., 1972: An efficient, one-level, primitive equation spectral model. *Mon. Wea. Rev., 100,* 683-689.

Bourke, W., B. McAvaney, K. Puri and R. Thurling, 1977: Global modeling of atmospheric flow by spectral methods. *Methods in Computational Physics, Vol. 17,* J. Chang, Ed., Academic Press, 267-324.

Cane, M. A., and E. S. Sarachik, 1976: Forced baroclinic ocean motions. 1. The linear equatorial unbounded case. *J. of Marine Research, 34,* 629-665.

Ceselski, B. F., 1973: A comparision of cumulus parameterization techniques. *Tellus, 25,* 459-478.

Charney, J. G., 1947: The dynamics of long waves in a baroclinic westerly current. *J. Meteor., 4,* 135-162.

Charney, J. G., 1969: A further note on large-scale motions in the tropics. *J. Atmos. Sci., 20,* 607-609.

Charney, J. G., and P. G. Drazin, 1961: Propagation of planetary-scale disturbances from the lower into the upper atmosphere. *J. Geophys. Rev., 74,* 83-109.

Charney, J. G., and A. Eliassen, 1949: A numerical method of predicting the perturbations of the middle latitude westerlies. *Tellus, 1,* 38-54.

Charney, J. G., and A. Eliassen, 1964: On the growth of the hurricane depression. *J. Atmos. Sci., 21.,* 68-75.

Chervin, R. M., W. M. Washington and S. H. Schneider, 1976: Testing the statistical significance of the response of the NCAR general circulation model to North Pacific ocean surface temperature anomalies. *J. Atmos. Sci., 33,* 413-423.

Corby, G. A., A. Gilchrist and R. L. Newson, 1972: A general circulation model of the atmosphere suitable for long period integration. *Quart. J. R. Met. Soc., 98,* 809-832.

Dickinson, R. E., 1968: Planetary Rossby wave propagating vertically through weak weaterly wind wave guides. *J. Atmos. Sci., 25,* 984-1002.

Dickinson, R. E., 1978: On planetary waves. The general circulation: Theory, Modeling, and Observation, NCAR, 59-82.

Eady, E. T., 1949: Long waves and cyclone waves. *Tellus, 1,* 33-52.

Egger, J., 1977: On the linear theory of the atmospheric response to sea surface temperature anomalies. *J. Atmos. Sci., 34,* 603-614.

Egger, J., and H.-D. Schilling, 1983: On the theory of long-term variability of the atmosphere. *J. Atmos. Sci., 40,* 1073-1085.

Eliasen, E., B. Machenhauer and E. Rasmussen, 1970: On a numerical method for integration of the hydrodynamical equations with a spectral representation of the horizontal fields. Report No. 2, Inst. of Theor. Meteor., Univ. of Copenhagen, Denmark.

Eliassen, A., and E. Palm, 1961: On the transfer of energy in stationary mountain waves. *Geofys. Publ., 22,* No. 3, 1-23.

Esbensen, S. K., and Y. Kushnir, 1981: The heat budget of the global ocean: An atlas based on estimates from surface marine observations. Report No. 29, Climatic Research Institute, Oregon State Univ., Corvallis, 219 pp.

Frederiksen, J. S., 1982: An unified three-dimensional instability theory of the onset of blocking and cyclogenesis. *J. Atmos. Sci., 39,* 969-982.

Gambo, K., and K. Kudo, 1983: Three-dimensional teleconnections in the zonally asymmetric height field during the Northern Hemisphere winter. *J. Meteor. Soc. Japan, 61,* 36-49.

Gates, W. L., 1975: The January global climate simulation by a two-level general circulation model: A comparison with observation. *J. Atmos. Sci., 32,* 449-477.

Gates, W. L., 1979: An essay on the physical basis of climate. Report No. 7, Climatic Research Institute, Oregon State Univ., Corvallis, 29 pp.

Ghan, S. J., J. W. Lingaas, M. E. Schlesinger, R. L. Mobley and W. L. Gates, 1982: A documentation of the OSU two-level atmospheric general circulation model. Report No. 35, Climatic Research Institute, Oregon State Univ., Corvallis, 395 pp.

Gill, A. E., 1980: Some simple solutions for heatinduced tropical circulation. *Quart. J. Roy. Met. Soc., 106,* 447-462.

Gordon, H. B., 1981: A flux formulation of the spectral atmospheric equations suitable for use in long-term climate modeling. *Mon. Wea. Rev., 109,* 56-64.

Grose, W. L., and B. J. Hoskins, 1979: On the influence of orography on large-scale atmospheric flow. *J. Atmos. Sci., 36,* 223-245.

Haltiner, G. J., and R. T. Williams, 1980: Numerical Prediction and Dynamic Meteorology. 2nd Ed., John Wiley & Sons, Inc., 477pp.

Han, Y.-J., W. L. Gates and J.-W. Kim, 1980: A numerical investigation of equatorial ocean dynamics with reference to El Niño. Report No. 20, Climatic Research Institute, Oregon State Univ., Corvallis, 35 pp.

Haseler, J., 1982: An investigation of the impact at middle and high latitudes of tropical forecast errors. ECMWF. Tech. Rep. No. 31, 42 pp.

Hayashi, Y., 1970: A theory of large-scale equatorial waves generated by condensation heat and accelerating the zonal wind. *J. Meteor. Soc. Japan, 48,* 140-160.

Held, I. M., and M. J. Suarez, 1978: A two-level primitive equation atmospheric model designed for climate sensitivity experiments. *J. Atmos. Sci., 35,* 206-229.

Hendon, H. H., and D. L. Hartmann, 1982: Stationary waves on a sphere: Sensitivity of thermal feedback. *J. Atmos. Sci., 39,* 1906-1920.

Holton, J. R., 1971: A diagnostic model for equatorial wave disturbance: The role of vertical shear of the mean zonal wind. *J. Atmos. Sci., 28,* 55-64.

Holton, J. R., 1979: An Introduction to Dynamical Meteorology. 2nd Ed., Academic Press, 391 pp.

Horel, J. D., and J. M. Wallace, 1981: Planetary-scale atmospheric phenomena associated with the Southern Oscillation. *Mon. Wea. Rev., 109,* 813-829.

Hoskins, B. J., and D. J. Karoly, 1981: The steady linear response of a spherical atmosphere to thermal and orographic forcing. *J. Atmos. Sci., 38,* 1179-1196.

Hoskins, B. J., and A. J. Simmons, 1975: A multi-layer spectral model and the semi-implicit method. *Quart. J. Roy. Met. Soc., 101,* 637-655.

Hoskins, B. J., A. J. Simmons and D. J. Andrews, 1977: Energy dispersion in a barotropic atmosphere. *Quart. J. Roy. Met. Soc., 103,* 553-567.

Julian, P. R., and R. M. Chervin, 1978: A study of the Southern Oscillation and Walker Circulation phenomenon. *Mon. Wea. Rev., 106,* 1433-1451.

Kang, I.-S., and Y.-J. Han, 1984: Quasi-stationary atmospheric responses to the large-scale forcing associated with tropical sea surface temperature anomalies. Proceedings of the 15th Technical Conference on Hurricane and Tropical Meteorology (in press).

Kasahara, A., T. Sasamori and W. M. Washington, 1973: Simulation experiments with a 12-layer staratospheric global circulation model. 1. Dynamical effect of the earth's orography and thermal influence of continentality. *J. Atmos. Sci., 30,* 1229-1251.

Keshavamurty, R. N., 1982: Response of the atmosphere to sea-surface temperature anomalies over the equatorial Pacific and teleconnections of the Southern Oscillation. *J. Atmos. Sci., 39,* 1241-1259.

Khalsa, S. J. S., 1983: The role of sea surface temperature in large-scale air-sea interaction. *Mon. Wea. Rev., 111,* 954-966.

Krueger, A. F., and J. S. Winston, 1974: A comparision of the flow over the tropics during two contrasting circulation regimes. *J. Atmos. Sci., 31,* 358-370.

Krueger, A. F., and J. S. Winston, 1975: Large-scale circulation anomalies over the tropics during 1971-1972. *Mon. Wea. Rev., 103,* 465-473.

Krylov, V. I., 1962: Approximate Calculation of Integrals. The Macmillan Company, New York, 357 pp.

Lau, N.-C., 1979: The observed structure of tropospheric stationary waves and local balances of vorticity and heat. *J. Atmos. Sci.*, *36*, 996-1016.

Lau, N.-C., 1981: A diagnostic study of recurrent meteorological anomalies appearing in a 15-year simulation with a GFDL general circulation model. *Mon. Wea. Rev.*, *109*, 2287-2311.

Lorenz, E. N., 1972: Barotropic instability of Rossby wave motion. *J. Atmos. Sci.*, *29*, 258-264.

Manabe, S., and T. B. Tepstra, 1974: The effects of mountains on the general circulation of the atmosphere as identified by numerical experiments. *J. Atmos. Sci.*, *31*, 3-42.

Matsuno, T., 1966: Quasi-geostrophic motions in the equatorial area. *J. Meteor. Soc. Japan*, *44*, 25-43.

Matsuno, T., 1970: Vertical propagation of stationary planetary waves in the winter Northern Hemisphere. *J. Atmos. Sci.*, *27*, 871-883.

McCreary, J., 1976: Eastern tropical ocean response to changing wind systems: with application to El Niño. *J. Phys. Oceanogr.*, *6*, 632-645.

Murakami, M., 1974: Influence of mid-latitudinal planetary waves on the tropics under the existance of critical latitude. *J. Meteor. Soc. Japan*, *52*, 261-271.

Namias, J., 1976: Negative ocean-air feedback systems over the North Pacific in the transition from warm to cold seasons. *Mon. Wea. Rev.*, *104*, 1107-1121.

Namias, J., 1978: Multiple causes of the North American abnormal winter 1976-77. *Mon. Wea. Rev.*, *106*, 279-295.

Opsteegh, J. D., and H. M. van den Dool, 1980: Seasonal differences in the stationary response of a linearized primitive equation model: Prospects for longrange weather forecasting? *J. Atmos. Sci.*, *37*, 2169-2185.

Pan, Y. H., and A. H. Oort, 1983: Global climate variations connected with sea surface temperature anomalies in the equatorial Pacific Ocean for the 1958-1973 period. *Mon. Wea. Rev.*, *111*, 1244-1258.

Pedlosky, J., 1979: Geophysical Fluid Dynamics. Springer-Verlag, 624 pp.

Platzman, G. W., 1960: The spectral form of the vorticity equation. *J. Meteor.*, *17*, 635-644.

Ramage, C. S., and T. Murakami, 1973: Comment on the paper by P. R. Rowntree: "The influence of tropical east Pacific Ocean temperature on the atmosphere." *Quart. J. Roy. Met. Soc., 99,* 393-394.

Rasmusson, E. M., and T. H. Carpenter, 1982: Variations in tropical sea surface temperature and surface wind fields associated with the Southern Oscillation/El Niño. *Mon. Wea. Rev., 110,* 354-384.

Reiter, E. R., 1978: Long-term wind variability in the tropical Pacific, its possible causes and effects. *Mon. Wea. Rev., 106,* 324-330.

Reiter, E. R., 1983: Teleconnections with tropical precipitation surges. *J. Atmos. Sci., 40,* 1631-1647.

Robert, A. J., 1969: The integration of a spectral model of the atmosphere by the implicit method. Proc. WMO/IUGG Symp., Japan Meteor. Agency, 1968. pp. VII-19 - VII-24.

Rodgers, C. D., and C. D. Walshaw, 1966: The computation of infra-red cooling rate in planetary atmosphere. *Quart. J. Roy. Met. Soc., 92,* 67-92.

Rogers, J. C., and H. van Loon, 1979: The seesaw in winter temperatures between Greenland and Northern Europe. Part 2: Some oceanic and atmospheric effects in middle and high latitudes. *Mon. Wea. Rev., 107,* 509-519.

Rossby, C.-G., 1945: On the propagation of frequencies and energy in certain types of oceanic and atmospheric waves. *J. Meteor., 2,* 187-203.

Rowntree, P. R., 1972: The influence of tropical east Pacific Ocean temperatures on the atmosphere. *Quart. J. Roy. Met. Soc., 98,* 290-321.

Rowntree, P. R., 1976: Tropical forcing of atmospheric motions in a numerical model. *Quart. J. Roy. Met. Soc., 102,* 583-605.

Sankar-Rao, M., and B. Saltzman, 1969: On a steady theory of global monsoons. *Tellus, 21,* 308-330.

Schlesinger, M. E., and W. L. Gates, 1981a: Preliminary analysis of the mean annual cycle and interannual variability simulated by the OSU two-level atmospheric general circulation model. Report No. 23, Climatic Research Institute, Oregon State Univ., Corvallis, 47 pp.

Schlesinger, M. E., and W. L. Gates, 1981b: Preliminary analysis of four general circulation model experiments on the role of the ocean in climate. Report No. 25, Climatic Research Institute, Oregon State Univ., Corvallis, 56 pp.

Schneider, E. K., and R. S. Lindzen, 1977: Axially symmetric steady-state models of the basic state for instability and climate studies. Part I. Linearized calculations. *J. Atmos. Sci., 34,* 263-279.

Shukla, J., and J. M. Wallace, 1983: Numerical simulation of the atmospheric response to equatorial Pacific sea surface temperature anomalies. *J. Atmos. Sci., 40,* 1613-1630.

Silberman, I., 1954: Planetary waves in the atmosphere. *J. Meteor., 11,* 27-34.

Smagorinsky, J., 1953: The dynamical influence of large scale heat sources and sinks on the quasi-stationary mean motions of the atmosphere. *Quart. J. Roy. Met. Soc., 79,* 342-366.

Simmons, A. J., 1982: The forcing of stationary wave motion by tropical diabatic heating. *Quart. J. Roy. Met. Soc., 108,* 503-534.

Simmons, A. J., and B. J. Hoskins, 1975: A comparison of spectral and finite-difference simulations of a growing baroclinic wave. *Quart. J. Roy. Met. Soc., 101,* 551-565.

Simmons, A. J., J. M. Wallace and G. Branstator, 1983: Barotropic wave propagation and instability, and atmospheric teleconnection patterns. *J. Atmos. Sci., 40,* 1363-1392.

Spar, J., 1973: Some effects of surface anomalies in a global general circulation model. *Mon. Wea. Rev., 101,* 91-100.

Spiegel, M. R., 1974: Theory and Patterns of Fourier Analysis. Schaum's outline series, McGraw-Hill Book Company, 191 pp.

Schutz, C., and W. L. Gates, 1971: Global climatic data for surface, 800 mb, 400 mb: January. R-915-ARPA, The Rand Corporation, Santa Monica, CA, 173 pp.

Troup, A. J., 1965: The Southern Oscillation. *Quart. J. Roy. Met. Soc., 91,* 490-506.

Tung, K. K., and R. S. Lindzen, 1979: A theory of stationary long waves. Part 1: A simple theory of blocking. *Mon. Wea. Rev., 107,* 714-734.

van den Dool, H. M., 1983: A possible explanation of the observed persistence of monthly mean circulation anomalies. *Mon. Wea. Rev., 111,* 539-544.

van Loon, H., and R. A. Madden, 1981: The Southern Oscillation. Part 1: Global associations with pressure and temperature in the northern winter. *Mon. Wea. Rev., 109,* 1150-1162.

van Loon, H., and J. C. Rogers, 1978: The seesaw in winter temperatures between Greenland and Northern Europe. Part 1: General description. *Mon. Wea. Rev., 106,* 296-310.

van Loon, H., and J. C. Rogers, 1981: The Southern Oscillation. Part 2: Associations with changes in the middle troposphere in the northern winter. *Mon. Wea. Rev., 109,* 1163-1168.

Wallace, J. M., 1978: Beyond the zonally averaged general circulation. The general circulation: Theory, modeling, and observations. NCAR, 40-48.

Wallace, J. M., and D. S. Gutzler, 1981: Teleconnections in the geopotential height field during the Northern Hemisphere winter. *Mon. Wea. Rev., 109,* 784-812.

Weare, B. C., 1982: El Niño and tropical Pacific Ocean surface temperature. *J. Phys. Oceanogr., 12,* 17-27.

Webster, P. J., 1972: Response of the tropical atmosphere to local, steady forcing. *Mon. Wea. Rev., 100,* 518-540.

Webster, P. J., 1981: Mechanisms determining the atmospheric response to sea surface temperature anomalies. *J. Atmos. Sci., 38,* 554-570.

Webster, P. J., 1982: Seasonality in the local and remote atmospheric response to sea surface temperature anomalies. *J. Atmos. Sci., 39,* 41-52.

Wyrtki, K., 1975: El Niño - the dynamic response of the equatorial Pacific Ocean to atmosphere forcing. *J. Phys. Oceanogr., 5,* 572-584.

Yamasaki, M., 1968: Numerical simulation of tropical cyclone development with the use of primitive equations. *J. Meteor. Soc. Japan, 46,* 178-201.

APPENDICES

APPENDICES

Appendix A. The vertical difference scheme

The vertical finite-difference scheme used in the present baroclinic model is basically the same as that of Hoskins and Simmons (1975). This scheme has second-order accuracy and formally conserves kinetic energy.

This scheme uses the centered differnece method as follows:

$$\dot{\sigma} \frac{\partial X}{\partial \sigma} = \frac{1}{2\Delta\sigma} \left[\dot{\sigma}_{r+1/2}(X_{r+1} - X_r) + \dot{\sigma}_{r-1/2}(X_r - X_{r-1})\right]$$

Then the finite-difference analogue of the hydrostatic equation may be written

$$\Phi_r - \Phi_{r+1} = \alpha_r(T_r - T_{r+1})$$

where $\alpha_r = \frac{1}{2}\ell n(\sigma_{r+1}/\sigma_r)$. Assuming an isothermal lowest layer, the geopotential at the lowest layer may be obtained as

$$\Phi_N = \Phi_S + \alpha_N T_N$$

where $\alpha_N = \ell n(1/\sigma_N)$. N represents the lowest layer, and Φ_S is the geopotential at the surface ($\sigma = 1$).

Appendix B. The matrices and vectors used in the baroclinic model

The finite-difference analogues of the matrices and vectors defined in section 2.2 are:

$$\Pi_r = \frac{1}{\cos^2\phi}\frac{\partial B_r}{\partial\lambda} - \frac{1}{\cos\phi}\frac{\partial A_r}{\partial\phi} - \nabla^2\frac{\overline{U}_r U'_r}{\cos^2\phi} + F_{D'_r}$$

$$\Gamma_r = -\frac{1}{\cos^2\phi}\frac{\partial}{\partial\lambda}\left(\overline{U}_r T'_r + U'_r\overline{T}^*_r\right) - \frac{1}{\cos\phi}\frac{\partial}{\partial\phi}\left(V'_r\overline{T}^*_r\right) + \overline{T}^*_r D'_r$$

$$- \frac{1}{2\Delta\sigma_r}\Bigg[\left\{\dot{\sigma}'_{r+\frac{1}{2}}\left(\overline{T}^*_{r+1} - \overline{T}^*_r\right) - \dot{\sigma}'_{r-\frac{1}{2}}\left(\overline{T}^*_r - \overline{T}^*_{r-1}\right)\right\}$$

$$+ \left(T_{0_{r+1}} - T_{0_r}\right)\left\{\left(\sum_{s=1}^{r}\Delta\sigma_s\right)\sum_{s=1}^{N}A'_s\Delta\sigma_s - \sum_{s=1}^{r}A'_s\Delta\sigma_s\right\}$$

$$+ \left(T_{0_r} - T_{0_{r-1}}\right)\left\{\left(\sum_{s=1}^{r-1}\Delta\sigma_s\right)\sum_{s=1}^{N}A'_s\Delta\sigma_s - \sum_{s=1}^{r-1}A'_s\Delta\sigma\right\}$$

$$+ 2\kappa\overline{T}_r\left\{\alpha_r\sum_{s=1}^{r}A'_s\Delta\sigma_s + \alpha_{r-1}\sum_{s=1}^{r-1}A'_s\Delta\sigma_s\right\}$$

$$+ 2\kappa\overline{T}^*_r\left\{\alpha_r\sum_{s=1}^{r}D'_s\Delta\sigma_s + \alpha_{r-1}\sum_{s=1}^{r-1}D'_s\Delta\sigma_s\right\}\Bigg]$$

$$+ \kappa\overline{T}_r A'_r + \frac{Q'_r}{C_p} + F_{T'_r}$$

where $$A'_r = \frac{\overline{U}_r}{a \cos^2\phi} \frac{\partial \ell n P'_s}{\partial \lambda} + \frac{V'_r}{a \cos\phi} \frac{\overline{\partial \ell n P_s}}{\partial \phi}$$

$$\tau_{rs} = \frac{1}{2\Delta\sigma_r} \left[(T_{0r+1} - T_{0r}) \left\{ \Delta\sigma_s \left(\sum_{i=1}^{r} \Delta\sigma_i \right) - \begin{vmatrix} 0 & (r<s) \\ \Delta\sigma_s & (r \geq s) \end{vmatrix} \right\} \right.$$

$$+ (T_{0r} - T_{0r-1}) \left\{ \Delta\sigma_s \left(\sum_{i=1}^{r-1} \Delta\sigma_i \right) - \begin{vmatrix} 0 & (r-1<s) \\ \Delta\sigma_s & (r-1 \geq s) \end{vmatrix} \right\}$$

$$\left. + 2\kappa T_{0r} \Delta\sigma_s \left\{ \begin{vmatrix} \alpha_r & (s \leq r) \\ 0 & (s>r) \end{vmatrix} + \begin{vmatrix} \alpha_{r-1} & (s \leq r-1) \\ 0 & (s>r-1) \end{vmatrix} \right\} \right]$$

$$g = \begin{pmatrix} \alpha_1 & \alpha_1 + \alpha_2 \\ 0 & \alpha_2 \end{pmatrix}$$

$$P = - \sum_{r=1}^{N} A'_r \Delta\sigma_r$$

$$p_r = \Delta\sigma_r$$